Factors affecting the severity of European winter windstorms

DISSERTATION

zur Erlangung des akademischen Grades
eines Doktors der Naturwissenschaften am
Fachbereich Geowissenschaften der Freien
Universität Berlin

vorgelegt von
Thomas Moran

Freie Universität Berlin

Berlin, 1 Oktober 2019

1. Gutachter: Prof. Dr. Uwe Ulbrich, Institut für Meteorologie, Freie Universität Berlin
2. Gutachter: Prof. Dr. Henning Rust, Institut für Meteorologie, Freie Universität Berlin

Selbstandigkeitserklarung

Hiermit erkläre ich an Eides Statt, dass ich die vorliegende Arbeit selbstständig und ohne fremde Hilfe angefertigt, keine anderen als die angegebenen Quellen und Hilfsmittel benutzt und die den benutzten Quellen wörtlich oder inhaltlich entnommenen Stellen als solche kenntlich gemacht habe. Diese Arbeit hat in gleicher oder ähnlicher Form noch keiner Prüfungsbehörde vorgelegen.

Berlin, 1. Oktober 2019

Abstract

Every year, dozens of intense extra-tropical cyclones strike Europe with high intensity wind-fields — or windstorms — that inflict significant damage to local infrastructure and housing. In terms of reinsurance losses, windstorms are the most socioeconomically dangerous hazards affecting Europe to date. Stakeholders from both the public and private sectors are interested in improving the predictability of these systems, and while substantial advancements have been made towards a better understanding of their occurrence frequency, little has been explored in terms of their potential severity. Thus, the thesis focuses on the factors affecting the severity (or footprint) of European windstorms by taking a large set of events from the MPI-ESM-LR model, and ERA-20C reanalysis data. After defining a windstorm footprint metric, windstorms are objectively matched to unique cyclones, where it is assumed the windstorm is created by its paired cyclone (the paired system is called a "storm"). These storms form the basis of the systems studied in the thesis as they provide more upstream information. Factors are explored in three core topics: i) characterising European wind-storms in terms of their parent cyclones; ii) exploring the role of various cyclonic growth factors (CGFs) on storm footprints; and iii) using a Generalized Linear Model (GLM) to quantitatively rank the importance of factors affecting these footprints.

In terms of their parent cyclones, it is found that extremely high windstorm footprints are associated with deeper and faster-growing cyclones, and non-extreme systems show a weaker relationship. Strong windstorms are additionally associated with bomb cyclones. Windstorms usually form 2 days after cyclogenesis and are found to intensify in a 24-hour window centered on cyclone maximum intensification. Finally, we investigated the cyclone pathways which create high European windstorm footprints. Cyclogenesis maxima are situated over the North Atlantic, with a higher density towards the West near the US East Coast. These cyclones intensify on the southwest flank of the British Isles before entering Europe with a high intensity, creating a high European footprint.

Then, we study the role of five CGFs in these cyclone pathways: the jet stream, Eady Growth Rates (EGRs), potential vorticity at 850 hPa (PV850), land-sea contrasts (LSCs), and sea-surface temperature (SST) gradients. To determine whether the magnitudes of these anomalies are related to the European storm footprint, they are composited at the time and location of cyclogenesis or maximum intensification, and are compared between extremely high and low European footprint storms. We find that strong jet streams and latent heat release during the cyclone intensification phase in the East Atlantic have a large influence on the storm footprint, with some influence from these processes at the cyclogenesis phase in the West Atlantic. Lastly, we find evidence that stronger LSCs over the US East Coast are related to higher footprint windstorms, but SST gradient results disagreed between the data sets and may instead be related only to the occurrence of windstorms. Altogether, high European footprint storms are related to a few CGFs influencing cyclogenesis in the West Atlantic (e.g. LSCs and local baroclinicity), followed by other CGFs influencing intensification in the East Atlantic (e.g. PV850).

The previous two sections explored how cyclone properties and CGFs influence high European footprint storms, so we utilize a GLM to quantitatively assess all of these factors which are represented as "predictors" using field means or binary conditions. Six models

are constructed: the first four relate to regional subsets of the storms, and the last two incorporate regional development as predictors. From the parameter estimations of each model result, we find that jet stream and PV850 anomalies at the cyclone intensification phase and West Atlantic cyclogenesis provide the most explanatory power. Moreover, a positive NAO emerges as a strong predictor in the case that storms benefit from being deflected in a northeasterly direction towards Europe (e.g. in MPI-ESM-LR data). Both LSCs and SST gradients appear to be strong predictors, but their disagreements between the two data sets suggest that further analysis is required.

Overall, we determined the most likely factors (among many) influencing a high European windstorm footprint. These are cyclones which generate in the West Atlantic thanks to baroclinicity and surface thermal gradients, a cyclone maximum intensification phase accompanied by a transient jet anomaly and a large amount of diabatic release near the British Isles (especially during a positive NAO phase), and a windstorm genesis and intensification during this phase.

Zusammenfassung

Jedes Jahr treffen Dutzende von intensiven extra-tropischen Zyklonen auf Europa mit hochintensiven Windfeldern - oder Stürmen - die der lokalen Infrastruktur und Wohngebäuden / Gebäuden erheblichen Schaden zufügen. In Bezug auf die Rückversicherungsschäden sind Stürme die bislang sozioökonomisch gefährlichsten Gefahren für Europa. Aus dem öffentlichen und privaten Sektor sind an einer Verbesserung der Vorhersagbarkeit dieser Systeme interessiert, und obwohl wesentliche Fortschritte hinsichtlich eines besseren Verständnisses ihrer Auftrittshäufigkeit erzielt wurden, gibt es hinsichtlich ihrer potenziellen Schwere/Intensität wenig Untersuchungen. Die Dissertation konzentriert sich daher auf die Faktoren, die die Schwere (oder den Fußabdruck) europäischer Stürme beeinflussen, indem eine große Anzahl von Ereignissen aus MPI-ESM-LR Modell und ERA-20C-Reanalysedaten entnommen werden.

Nachdem eine Windstorm-Footprint-Metrik definiert wurde, werden Windstürme objektiv einer Zyklone zugeordnet, wobei davon ausgegangen wird, dass der Windsturm durch seine gepaarte Zyklone erzeugt wird (das gepaarte System wird als "Sturm" bezeichnet). Diese Stürme bilden die Grundlage für die in der Arbeit untersuchten Systeme, da sie mehr vorgelagerte Informationen liefern. Faktoren werden in drei Kernthemen untersucht: i) Charakterisierung europäischer Stürme in Bezug auf ihre Elternzyklone; ii) Untersuchung des Einflusses verschiedener Zyklonenwachstumsfaktoren (ZFs) auf die Fußabdrücke von Stürmen; und iii) Verwenden eines verallgemeinerten linearen Modells (GLM), um die Wichtigkeit von Faktoren, die diese Fußabdrücke beeinflussen, quantitativ zu bewerten.

In Bezug auf die übergeordneten Zyklonen wurde festgestellt, dass extrem hohe Windsturmspuren mit tieferen und schneller wachsenden Zyklonen verbunden sind und nichtextreme Systeme eine schwächere Beziehung aufweisen. Starke Stürme sind typischerweise auch mit Bombenzyklonen (also solchen, deren Kerndruck extrem schnell fällt) verbunden. Stürme bilden sich normalerweise zwei Tage nach der Zyklogenese und verstärken sich in einem 24-Stunden-Fenster, das sich rund um die maximale Intensität des Zyklons zentriert. Schließlich wurden die Zyklonenwege von Systemen untersucht, die hohe europäische Windsturmspuren erzeugen. Zyklogenese- Maxima liegen über dem Nordatlantik mit einer höheren Dichte nach Westen in der Nähe der US-Ostküste. Diese Zyklonen verstärken sich an der Südwestflanke der britischen Inseln, bevor sie mit hoher Intensität nach Europa vordringen, wodurch ein hoher europäischer Fußabdruck entsteht. Anschließend wird die Rolle von fünf ZFs in diesen Zyklonpfaden untersucht: Jet streams, Eady Growth Rates (EGRs), potenzielle Vorticity auf 850 hPa (PV850), Land-See-Kontraste (LSCs) und Meeresoberflächentemperatur (SST). Um festzustellen, ob die Größenordnungen dieser Anomalien mit dem europäischen Sturmfußabdruck zusammenhängen, werden sie zum Zeitpunkt und am Ort der Zyklogenese oder der maximalen Intensivierung zusammengesetzt und zwischen Stürmen mit extrem hohem bzw. extrem niedrigem europäischen Fußabdruck verglichen. Wir finden, dass starke Jet streams und die Freisetzung latenter Wärme während der Zyklonenintensivierungsphase im Ostatlantik einen großen Einfluss auf den Fußabdruck des Sturms haben, wobei ein gewisser Einfluss von diesen Prozessen in der Zyklogenesephase im Westatlantik ausgeht. Schließlich finden wir Hinweise darauf, dass stärkere LSCs über der Ostküste der USA mit Windstürmen mit größerer Grundfläche zusammenhängen, die Ergebnisse des

SST-Gradienten jedoch nicht zwischen den Datensätzen übereinstimmen und stattdessen möglicherweise nur mit dem Auftreten von Windstürmen zusammenhängen, nicht aber mit deren Intensität. Insgesamt hängen Stürme mit hohem europäischen Fußabdruck mit einigen ZF zusammen, die die Zyklogenese im Westatlantik beeinflussen (z. B. LSCs und lokale Baroklinität), gefolgt von anderen ZFs, die die Intensivierung im Ostatlantik beeinflussen (z. B. PV850).

Abschließend wird ein GLM verwendet, um alle die oben genannten Faktoren, die als "Prädiktoren" dargestellt werden, mithilfe von Feldmitteln oder binären Bedingungen quantitativ zu bewerten. Es werden sechs Modelle konstruiert: Die ersten vier beziehen sich auf regionale Untergruppen der Stürme, und die letzten beiden berücksichtigen die regionale Entwicklung als Prädiktoren. Aus den Parameterschätzungen der einzelnen Modellergebnisse geht hervor, dass Jetstream- und PV850-Anomalien in der Zyklonenintensivierungsphase und in der Zyklogenese im Westatlantik die größte Erklärungskraft haben. Darüber hinaus ergibt sich eine positive NAO als starker Prädiktor für den Fall, dass Stürme davon profitieren, in nordöstlicher Richtung nach Europa abgelenkt zu werden. Sowohl LSCs als auch SST-Gradienten scheinen starke Prädiktoren zu sein, aber ihre Unstimmigkeiten zwischen den beiden Datensätzen legen nahe, dass weitere Analysen erforderlich sind.

Insgesamt wurden die wahrscheinlichsten (von vielen) Faktoren ermittelt, die einen hohen europäischen Windsturm-Fußabdruck hervorrufen. Hierbei handelt es sich um Zyklonen, die im Westatlantik aufgrund von Baroklinität und thermischen Oberflächengradienten, einer Phase maximaler Intensivierung durchlaufen, welche von einer vorübergehenden Jetanomalie und einer starken diabatischen Wärmefreisetzung in der Nähe der britischen Inseln begleitet wird (insbesondere während einer positiven NAO-Phase), so dass sich in dieser Phase das zugehörige Sturmfeld bildet (Sturmgenese) und intensiviert.

Acknowledgments

This thesis would not have been possible without the continued support of my supervisors, Prof. Dr. Uwe Ulbrich and Prof. Dr. Henning Rust, and I would like to thank them for our enlightening scientific conversations in my journey to explore meteorological curiosities.

I would like to thank the diverse range of PIs, students, and administrators at both the Institute for Meteorology for providing much needed academic support and guidance. I would especially like to thank Jens, Mareike, and Ines — we made a smashing windstorm team and our conversations always provided inspiration throughout my time in Berlin.

This study might have never happened without the funding and support of NatRiskChange and the DFG, and for that I am extremely grateful. I would also like to thank the PIs and students part of the NatRiskChange group for their pleasant company during the retreats.

I am indebted to the support to my family and friends for being the best cheerleaders I could ask for, and for providing me with an unforgettable four years in Berlin.

And to Alessandro: words cannot express how appreciative I am to have your support — this thesis would not have been possible without you.

Contents

List of Figures

List of Tables

1 Introduction

1.1 An introduction to windstorms and their impacts

Every year, intense extratropical cyclones cause significant destruction in the European region through strong windstorms they create at the surface. According to Munich RE (NatCatService, 2019), 49% of events contributing to European losses between 1980 – 2018 were meteorological in nature. The five most devastating events include the winter storms Lothar, Kyrill, Daria, Xynthia and 87J, affecting various parts of Europe. Between these storms, they were responsible for over 22,800 million USD in insured losses and 308 fatalities.

There is no one way to classify and track specific events with extreme wind speeds. Windstorms are often considered by the reinsurance industry as systems which exceed the 98th percentile of surface wind speeds. For example, Klawa and Ulbrich (2003) constructed a windstorm loss model (compared against recorded losses) by scaling losses against the cube of the surface wind speed normalized by the 98th percentile. This allowed them to identify gridded regions with high wind speeds. Donat et al. (2010) used these anomalous 98th percentiles as well as the gale index, which instead considers strong wind events in terms of directional flow and voriticity associated with a particular MSLP field. Leckebusch et al. (2008) expanded on the concept of identifying gridded surface wind speed anomalies by tracking clusters of surface wind speed anomalies over time. Clusters which exceeded a minimum physical area and duration were classified as windstorm events, much in the same way one can track cyclone events. The power of tracking windstorms over time provides a great deal more information in both a conceptual and applied sense. This tracking scheme forms the basis of the windstorms considered in this study. Lastly, windstorms can often be associated with bomb cyclones, for instance the European storm Gong (Liberato, 2014).

The temporal behaviour of windstorms has been studied with great detail on the inter-annual scale (e.g. Renggli, 2011; Befort et al., 2016; Walz et al., 2018) and the multi-decadal scale (Nissen et al., 2014), along with their trends (Donat et al., 2011). However, the severity of these storms varies quite strongly between events, as can be seen in Leckebusch et al. (2008). From the same paper, we adapt a metric designed to construct a "European windstorm footprint" diagnostic, and study it for large sets of windstorms in both model and reanalysis data. The windstorms we study are synoptic in nature, and are typically associated with extra-tropical cyclones. Thus far, only Nissen et al. (2010) have matched windstorms to their cyclones, where they found that 69% of Mediterranean windstorms are caused by cyclones in the same region. This work explores the broad statistical relationships that can be found between the two systems in their of intensities and trajectories.

1.2 Cyclones and their growth factors

Extratropical cyclones in the North Atlantic come in many shapes and forms, and the manner in which they are forced by the environment is complex. In their climatology of North Atlantic extra-tropical cyclones, Gray and Dacre (2006) found that the majority of European systems were East Atlantic in origin. Moreover, they showed that explosively intensifying cyclones (or "bombs") typically form over the US East Coast (e.g. Allen et al., 2010). Pinto

et al. (2009) found that extreme cyclones develop in a similar region and typically propagate towards Greenland and Iceland, with a few storms arriving around the British Isles. Thus, while cyclones entering Europe are typically associated with cyclogenesis in the East Atlantic, the most devastating systems originate far upstream in the West Atlantic. Additionally, the evolution of such cyclones is of particular interest. Pinto et al. (2009) found that, during their intensification phase, extreme North Atlantic cyclones are associated with extremes in baroclinicity, the jet stream, divergence, and equivalent potential temperature. Gray and Dacre (2006) further found that West Atlantic cyclones are typically Type B in nature (Deveson et al., 2002), i.e. they are predominantly forced by upper-levels, but further show strong lower-level features, whereas East Atlantic cyclones include many Type C cyclones, or those developed by diabatic effects. In a later study, Dacre and Gray (2013) further showed that West and East Atlantic cyclones are enhanced by the presence of strong fronts and diabatically-generated mid-level potential vorticity. Raible (2007) demonstrated that meridional temperature gradients and land-sea contrasts are crucial for the development of North Atlantic cyclones. By studying 58 cyclones with high windstorm severities, Pirret et al. (2017) used the pressure tendency equation to find that baroclinic and diabatic processes, as well as the cyclone position relative to the jet, contributed to their development. If we look at specific cases, a recent salient storm is Kyrill, which intensified over the central North Atlantic as it crossed over in to the jet exit (Fink et al., 2009).

Of particular interest is the role of thermal gradients on the development of these cyclones, such as sea-surface temperature (SST) gradients and land-sea contrasts. In the North Atlantic, the transport of ocean heat by the Meridional Overturning Circulation (MOC) is primarily concentrated in the West Atlantic, where the western boundary currents and Gulf Stream can be located. In winter, this region is very energetic with respect to the rest of the North Atlantic. For instance, Shaman et al. (2010) show that sensible and latent heat fluxes in this region are closely related to storm activity. Here, it is crucial to discuss the direction of causality with respect to storm and ocean activity. On synoptic to intraseasonal timescales, the atmosphere generally "forces" the ocean (e.g. Hurrell et al., 2003). Moreover, lower-temperature SST anomalies will emerge in the wake of cyclones passing by via Ekman pumping: convergent flow in the atmospheric boundary layer causes divergent flow in the marine boundary layer directly beneath it, thus by mass conservation colder water rises to compensate. This process occurs on synoptic timescales and ultimately modifies the SST gradients (Hartmann, 2015). However, the ocean feeds back onto the atmosphere. Typically, we find that low-frequency SST anomalies are driven by oceanic processes and instead force the atmosphere (e.g. Gastineau et al., 2013; Gastineau and Frankignoul, 2015). Nakamura et al. (2004) discuss that SST gradients help maintain baroclinicity in this region, anchoring the generation and intensification of storms which localise there. SST gradients in the Gulf Stream region can dynamically force overlying baroclinic waves in a number of ways. Using a range of reanalysis, atmospheric general circulation model (GCM), and observational data, Minobe et al. (2008) showed that tight gradients in this region force the overlying atmospheric pressure field to adjust, in turn generating strong convergence lines. This results in narrow bands of strong precipitation extending into the upper troposphere. This may force planetary waves, which can remotely influence the development of storms in the North Atlantic downstream. Vries et al. (2019) studied a suite of extra-tropical cyclones

in a reanalysis set using dynamical downscaling, identifying how cyclone behaviour changes for different SST configurations. By smoothing the SSTs and hence reducing the gradients in this region, they found that there was no systematic relationship between the overlying surface wind speeds and these changes. However, they did find that tighter gradients lead to increase baroclinicity and latent heat fluxes in the overlying atmosphere, which were themselves conducive with increased cyclone activity.

The role of land-sea contrasts is often a challenging task, due in part to the fact they are constrained to very specific coastal regions around the Earth. However, some papers have quantified their role to some success. Nakamura and Yamane (2009) studied lower-tropospheric baroclinicity anomalies, which they found to be strongly associated with land-sea contrasts. Day and Hodges (2018) examined land-sea contrasts in a more systematic way. They instead looked at the Arctic Frontal Zone, a region of strong land-sea contrasts which circumnavigates around half of the Arctic circle. They found that both the intensity and frequency of Arctic cyclone activity is associated with years where this gradient is stronger, and that models may underestimate the true frequency and intensity of cyclones if they poorly resolve land-sea contrasts.

The problem of the resolution of thermal gradients and their interaction with the overlying atmosphere is a common one. Parfitt et al. (2017) discuss the role of SST resolution on the air-sea interactions around the Gulf Stream. They find that the frequency of atmospheric fronts increases by up to 30% depending as the resolution of the SSTs is increased. Moreover, precipitation and deep convection over this region is dependent on both the atmospheric and oceanic temperature resolution, and discussed by Scher et al. (2017). These concepts will be revisited throughout the thesis.

1.3   Examples of prominent windstorms

In order to understand what is likely to maximize a European windstorm's footprint, we look to examples of infamous storms and their growth. Figure 1 plots the track of Kyrill throughout its lifetime, as well the strength and structure of the nearby 250 hPa jet stream in 30° longidutinal slices centered on the cyclone center. The system originates over the US East Coast before traversing the North Atlantic ocean. At around 12 UTC on 17 January, it rapidly deepens as it travels through the jet stream and into its left exit. Shortly after, Kyrill enters Europe at around 55°N with a minimized core pressure.

Lothar (Ulbrich et al., 2001; Wernli et al., 2002) is another such storm that generated in the West and later intensified downstream due to a jet stream, where it was further accompanied by low-level PV anomalies. In fact, its intensification was initially suppressed until it was positioned in the jet exit such that it could benefit from upper-level divergence. An example of a prominent European storm which included a starkly different life cycle is the storm Xynthia. As opposed to most extreme extra-tropical European systems, Xynthia's track was predominantly sub-tropical before it was strongly deflected into Europe as it approached the Mediterranean. As Liberato et al. (2013) explain, Xynthia was supplemented by a high moisture supply and explosive diabatic release, contributing to an strong intensification phase in the Eastern North Atlantic.

Altogether, it is clear that a number of factors can affect the evolution of a North Atlantic
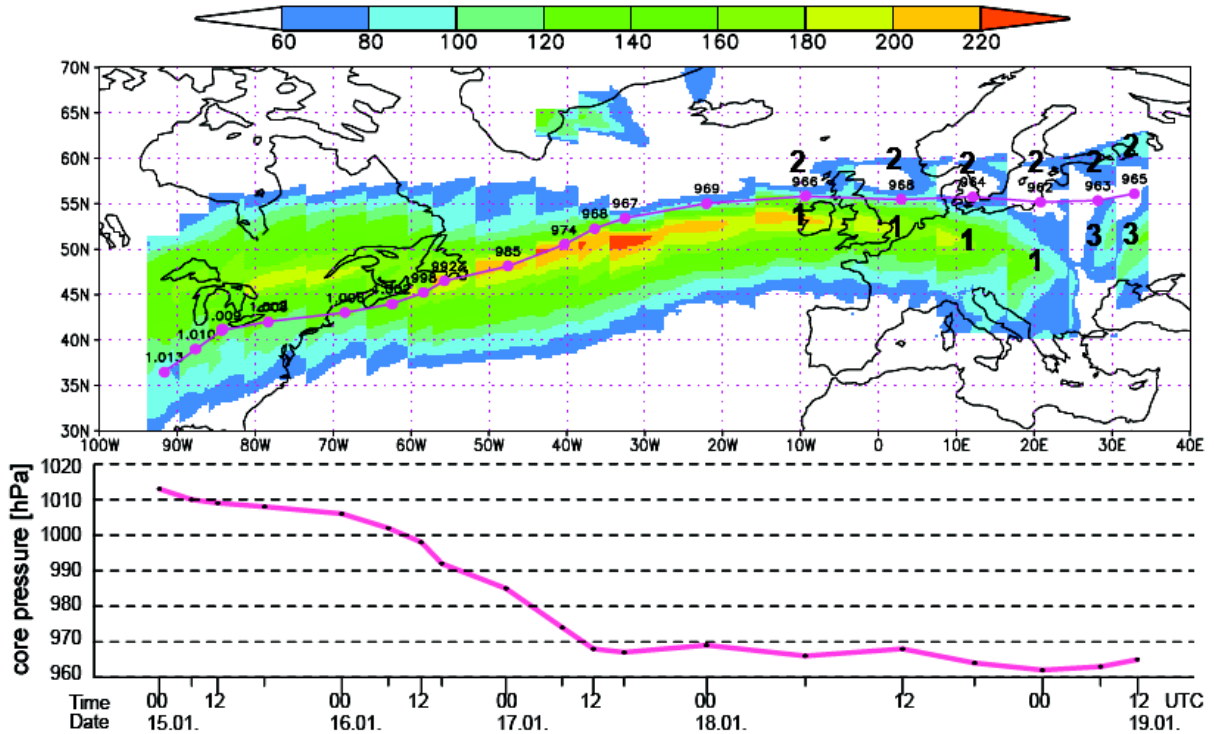
Figure 1: Top: The track of the extreme cyclone Kyrill, with moving slices of the nearby jet anomaly at each point of the track; colours represent the jet speed in knots. Bottom: core pressure of Kyrill throughout its lifetime. The numbers "1", "2", and "3" indicate split jets. From Fink et al. (2009)

cyclone and hence the windstorm it can produce in Europe. These factors include but are not limited to upper-level effects (e.g. the jet stream), baroclinicity in the troposphere, surface-level fronts (e.g. land-sea contrasts and SST gradients), and diabatic forcings. We have seen that some storms (e.g. Kyrill and Lothar) are more strongly related to their interaction with an upper-level feature, whereas systems like Xynthia are more closely related to high temperatures and moisture in the boundary layer contributing to more intense diabatic release. The key similarities between all of these systems are the following: genesis over the Western Atlantic, a gradual development over the North Atlantic ocean, and explosive intensification in the Eastern Atlantic. Together, these three steps form the following hypothesis which underpin this thesis: European windstorm severities are dependent on the necessary, but insufficient condition, that cyclones generate upstream of the North Atlantic and intensify in the Eastern Atlantic due to a combination of upper-level, diabatic, and baroclinic forcings.

Although there are clear similarities between windstorms and extreme cyclones, it is crucial to distinguish them before we continue. To begin with, **windstorms** refer to the tracked clusters of surface wind speed anomalies defined by the tracking scheme of Leckebusch et al. (2008). **Cyclones** refer to the tracks of MSLP minima (and other iterative steps) described by Murray and Simmonds (1991) and adapted for Northern Hemispheric cyclones by Pinto et al. (2005). It is assumed that *every windstorm is the daughter of a unique cyclone*, and the procedure matching the two systems (developed by Nissen et al., 2010) is described in more detail in Section 2.2. Finally, **storms** refer to the collective cyclone-windstorm systems, and thus includes many properties. The footprint of a storm refers to the windstorm's footprint, whereas the cyclogenesis of a storm, naturally, refers to the cyclone's genesis and not that of the windstorm system.

16

1.4   Extreme storms in a changing climate

As our climate changes due to anthropogenic forcings, so too does the frequency and intensity of extreme events, including cyclones and windstorms. With respect to extreme cyclones, Ulbrich et al. (2009) find that the frequency of intense events associated with deepening cyclones is expected to increase in many parts of Europe. This is accompanied by a positive shift in the 95th percentile of surface wind. By examining gale days and and surface wind percentiles, Donat et al. (2011) additionally find a similar result, where parts of Northern Europe show significant and positive trends in storminess.

1.5   Statistical modeling

Generalized linear models (GLMs) are typically employed in both social and natural sciences to encapsulate the response of a system's state to the state of a number of other variables. They are especially useful when dealing with a large number of possible explanatory variables. It can be used to test for causality (Shmueli et al., 2010), which is our aim in this thesis.

GLMs are frequently used in the atmospheric sciences in a number of ways, such as characterizing climate variability. Stevenson et al. (2013) utilize GLMs to model changes in ENSO based on principal-component-generated states of SSTs, which they found to have a good forecast skill at subyearly timescales. Chandler (2005) demonstrate that GLMs are especially useful for interpreting climate variability in cases where standard methods, such as Principal Component Analysis (PCA), may prove to be more cumbersome. With respect to European windstorms, Walz et al. (2018) used a Poisson GLM to reconstruct their interannual variability using an extensive suite of variables. These variables included, but were not limited to, interannual time series of teleconnection patterns (e.g. the NAO, ENSO, PNA), the large-scale surface temperature contrast between the US and the North Atlantic, among others. The response of a storm's strength to the intensity of its immediate environment has been primarily studied in, for example, Dacre and Gray (2013). They used a multiple linear regression to quantify the sensitivity of cyclone intensities based on the intensity of nearby variables. Graf et al. (2017) instead use PCA to objectively classify types of cyclogenesis, where they found upper-level and diabatic forcings as the most influential, but that cyclogenesis types exist on a continuous spectrum. To date, GLMs have not been applied to the severity of windstorms.

1.6   Structure of the thesis

Together with the hypothesis, the windstorms examined by this study are used to address the following three questions:

1. To what extent is the footprint of a windstorm attributable to properties of its parent cyclone?

2. How do combinations of the magnitude, positioning, and timing of cyclone growth factors relate to the windstorm footprint?

3. Can we rank, in order of importance, which factors play the most important role in a windstorm's footprint?

From this, we develop a framework in which windstorm footprints can be studied in terms of their cyclones' behaviour and environmental factors. Section 2 begins by scouring the data of windstorm-cyclone pairs in terms of their strength, growth properties, and regional development. Building from this, Section 3 then identifies the ways in which the magnitude, positioning, and timing of CGFs influence cyclones which create extremely high footprint European windstorms. We shift our focus to a GLM in Section 4, where we explore how the influence of the previously-explored factors can affect the footprint of a European windstorm's footprint. Lastly, Section 5 synthesizes the results of the previous sections.

2 European windstorm footprints and their relationship to cyclones

> Strange events permit themselves
> the luxury of occurring.
>
> *Charlie Chan*

This section is stratified in the following way. First, the interannual variability of windstorm footprints is studied: this is compared to their interannual frequency to highlight the advantages of studying their footprints. Then, we move on to sets of individual storm events. Each footprint is comprised of a number of components related to the windstorm's structure, so we first explore these relationships, and progress to the cyclones via the matching algorithm. Here, it is assumed that every windstorm is the daughter of a unique cyclone (recall that this collective cyclone-windstorm entity is a *storm*). Following from this, we identify the ways in which windstorms grow relative to their parent cyclone, and identify storm pathways associated with anomalously high footprints.

2.1 Data

Two primary sets of data are employed in this study. The first data set is comprised of historical simulations performed by the coupled Max Planck Institute Earth System Model (MPI-ESM). These experiments are conducted in low resolution (abbreviated as MPI-ESM-LR). The second data set is the ECMWF 20th century reanalysis (ERA-20C). Because windstorms are already an extreme system by nature, this necessitates the use of large data sets to find robust statistical patterns. Naturally, it is important to select datasets which capture extratropical processes sufficiently, such as the meridional overturning circulation, atmospheric circulations, energy balances, and the ebb and flow of the North Atlantic storm track and its associated tracked systems (i.e. windstorms and cyclones). Thus, MPI-ESM-LR was chosen as a model data set as it provides a wealth of systems to study. Similarly, ERA-20C was chosen as it is a relatively long reanalysis (over 100 years) which represents North Atlantic extratropical systems well. The details of these data sets and relevant studies which detail their ability to reproduce extratropical systems are described below. Important to note in these datasets is the inclusion of greenhouse gas forcings, which will produce trends in multiple signals. In Section 2.4 we will explore these trends with respect to windstorm activity. In the chapters to follow, we will compare signals between sets of anomalously high or low windstorm footprints.

Description of the MPI-ESM and historical runs

The MPI-ESM is a coupled model, whose various components are illustrated in Figure 2. More important to note are the atmospheric and oceanic components of the model, ECHAM6 and MPIOM, respectively. The low-resolution configuration is run on an atmospheric grid with resolution T63/1.9° L47 and an oceanic grid with resolution GR15 L40. As stated previously, the primary function of this model data is to provide an ample number of wind-

storms to study. With regards to windstorm frequencies, Kruschke et al. (2016) found that extratropical systems over the North Atlantic showed no significant biases with respect to a mixed ERA-40 and ERA-Interim reanalysis set.
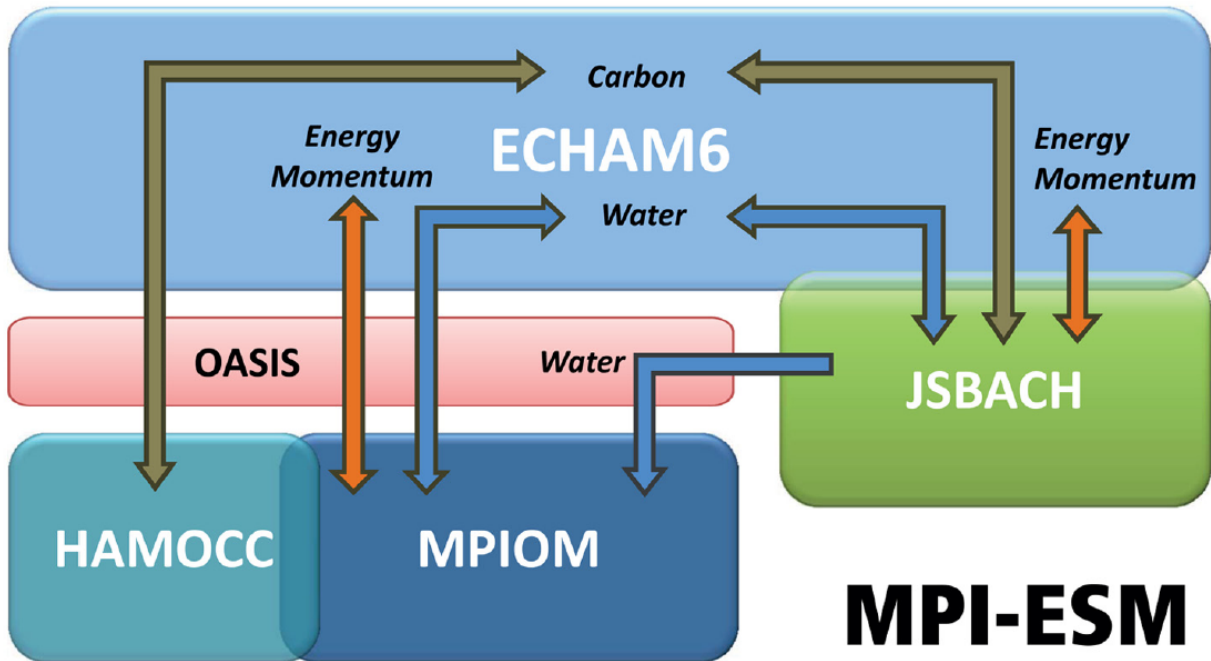
Figure 2: Components of the MPI-ESM model, from Giorgetta et al. (2013). ECHAM6 is the atmospheric component of the model directly coupled to the JSBACH land model that describes soil and vegetation via energy, momentum, water, and carbon fluxes. ECHAM6 is similarly coupled to MPIOM (the ocean general circulation model) and HAMOCC (describing marine biogeochemistry). A coupler program, OASIS, is employed to aggregate, interpolate, and exchange the aforementioned fluxes once per day between ECHAM6/JSBACH and MPIOM/HAMOCC.

The MPI-ESM model was used in accordance with the Coupled Intercomparison Model Project 5 (CMIP5), an ambitious project which aimed to test the robustness of model processes and climate projections by comparing a large number of models. One condition of models participating in this project was to employ three ensemble members of the historical run. These are uninitialized runs, i.e. they are not based on initial conditions relating to observational or reanalysis data. To create them, first the pre-industrial control simulation is run without any changing aerosol, land-use, or greenhouse gas concentrations, i.e. only internal variability is simulated. Once this pre-industrial control has reached a steady-state, seasonally varying tropospheric aerosols, stratospheric aerosols from volcanic eruptions, and greenhouse gas concentrations used from the time range 1850—2005 are employed. Each ensemble member of the historical runs differs only in terms of the pre-industrial control year in which they were initialized. In this case, they were initialized around 40 to 50 years apart from one another. In order to compare a similar time range to the reanalysis data (in which the total effect of external forcings are "synchronized"), we used data from 1950-2005 instead. This gives a total of 165 years of data. The ocean-atmosphere coupling by sending daily mean ocean-atmosphere fluxes to the ocean model, to be used as the ocean-surface forcing for the next daily coupling interval.

The ERA-20C reanalysis

All model data is compared to the reanalysis data, or ERA-20C (Poli et al., 2016). ERA-20C has a horizontal resolution of T159 on 91 vertical levels for the time period 1901-2010. Only atmospheric pressure and surface-wind observations are assimilated using a 4D-Var-scheme which is processed using the IFS cy38r1 model. The ocean data (such as sea surface temperatures [SSTs] or sea ice) are provided by HadISST2.1.0.0 (Titchner and Rayner, 2014) and are prescribed forcings in the model. Other prescribed forcings include solar radiation, tropospheric and stratospheric aerosols, ozone, and greenhouse gases. These data are provided by CMIP5.

Generally speaking, ERA-20C simulates synoptic activity and precipitation around the North Atlantic region fairly well, which relate strongly to the processes and regions studied in this thesis. Compared to other reanalyses (e.g. ERA-Interim, JRA-55) it faithfully reproduces major modes of climate variability such as the North Atlantic Oscillation (NAO), Nino 3.4 SST Index, Pacific North American Index (PNA), and the Southern Oscillation Index.

The interannual variability and trends of extreme cyclones and windstorms in ERA-20C have already been studied in detail by Befort et al. (2016). Figure 3 illustrates how they compare to NOAA-20CR. One can see that prior to the 1950s, there is a strong difference in overall trend and average number of windstorms. After, the two series converge and produce similar behaviour. It is crucial to note that surface observations were relatively sparse prior to the 1950s. Thus, they conclude that interpreting cyclone and windstorm behaviour on longer timescales prior to this period cannot be done confidently. For the remainder of this thesis, all ERA-20C data is taken from 1950—2010.
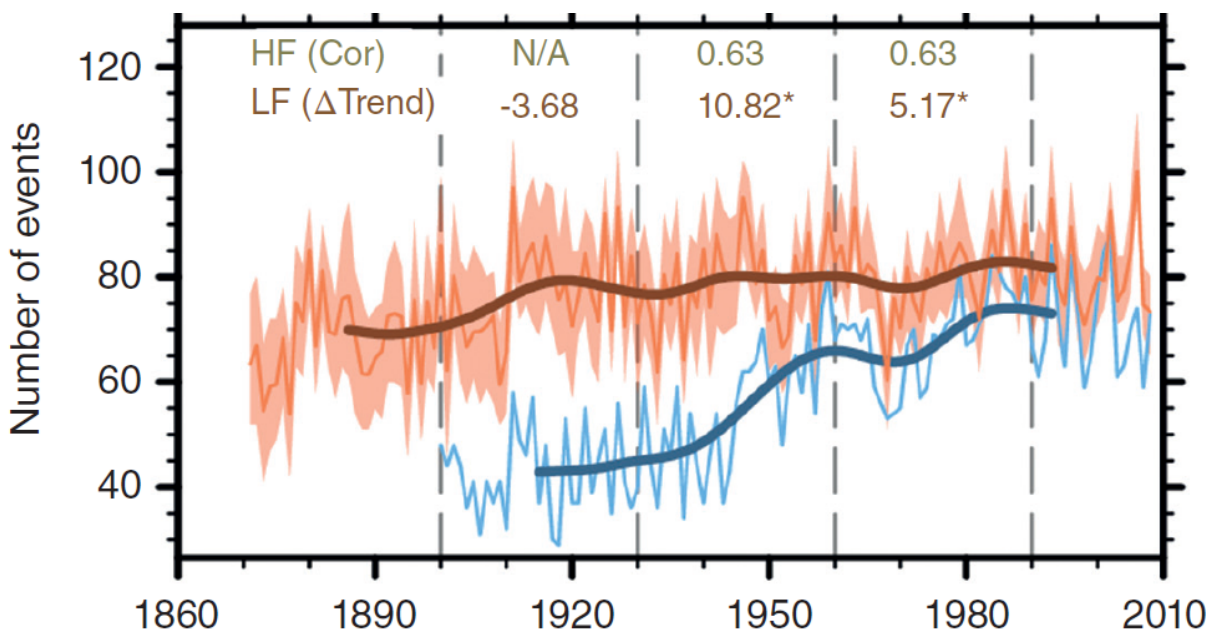
Figure 3: Interannual variability (thin lines) and trends (of windstorms in the North Atlantic for ERA-20C (blue) and NOAA-20CR (red), with the NOAA-20CR ensemble variability displayed by shading. The bold lines represent a low-pass filtered time series. The difference in low-frequency (LF) trends between the two series is displayed, such that changes statistically significant from zero are shown (*). From Befort et al. (2016).

A more prominent data set often used by atmospheric scientists is ERA-Interim, which assimilates a far greater number of variables. While it is perhaps a more realistic represen-

tation of our climate compared to ERA-20C, it has the drawback of far shorter time range (beginning from 1979 onwards). As stated previously, because windstorms are extreme systems with a relatively low frequency, ERA-20C was better suited for this study.

2.2   Methods

Windstorm tracking

The windstorm tracking scheme has been developed in great detail by Leckebusch et al. (2008) and Kruschke (2015). First, the scheme computes the surface (10 meter) wind speed from its zonal and meridional components. This data is 6-hourly and based on the instantaneous wind speed. Then, its 98th percentile is computed at each grid box. The scheme requires a few user-defined parameters. These include but are not limited to the minimum total physical area, the minimum length of windstorms, the maximum translational velocity, and the geographical boundaries in which we choose to study the storms. For this study and all associated data sets, a minimum area of 150,000 km^2 is chosen (in ERA-20C, for example, this is about a total of sixteen $1° \times 1°$ grid boxes). A minimum duration of 4 time steps is chosen (equal to 18 hours), as well as a maximum translational velocity of 600 km h^{-1}. Renggli (2011) found that sensitivity of the storm severities is not strongly sensitive to the minimum areas.

From here, we begin the iterative procedure of tracking the windstorms. First, from a given time step of the surface wind velocity field, locate grid boxes which exceed their grid box's 98th percentile. Adjacent grid boxes, or clusters, with a minimum aforementioned area are selected. Then, the center of the cluster is computed using the weighted average longitude and latitude of all the grid boxes in the cluster. In order to find the location of the cluster at the next time step, distances between the new and old clusters are calculated: those with the shortest distances are deemed the "same" cluster. Over this 6-hourly change, distances which are greater than the maximum translational velocity are excluded. Finally, lifetimes equal to or above the minimum lifetime are selected. The schematic in Figure 4 illustrates an idealized windstorm track.

The windstorm tracking scheme outputs tabulated data for each windstorm, with one row of data for each 6-hourly step. This includes the longitude and latitude of the cluster
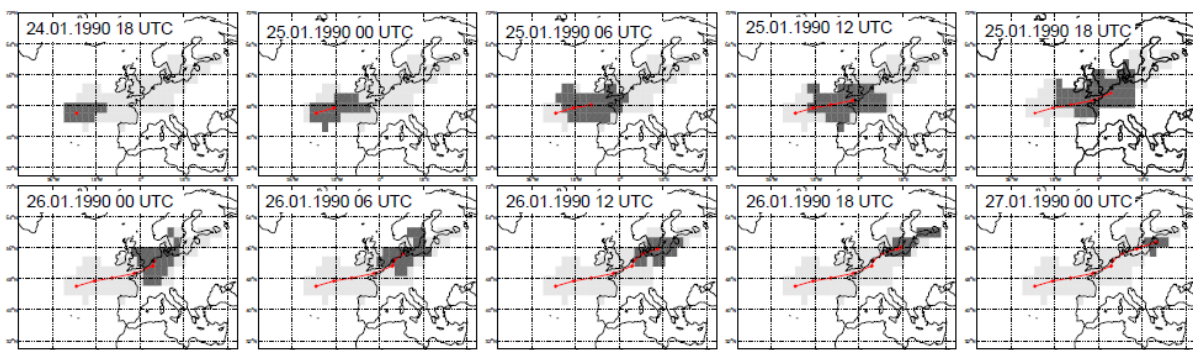
Figure 4: Example of the windstorm footprint of storm Daria at each of its ten timesteps. The gray boxes represent the grid boxes of surface wind velocities exceeding their local 98th percentiles, and light gray boxes are boxes affected by the storm at some time in the past. From Renggli (2011).

center of mass, its average surface wind velocity, its maximum surface wind velocity, and multiple severity metrics of the storm (explained in Section 2.2).

Windstorm footprints

The severity of individual windstorm events can be quantified by the Storm Severity Index (SSI), which is defined as:

$$SSI = \sum_t^T \sum_k^K \left[\max(0, v_{k,t}/v_{k,98} - 1)\right]^3 \times \frac{A_k}{A_0}, \tag{1}$$

where k represents a grid box, t the time step, and A_k the area of the grid box which is normalized by a reference area A_0 (this corresponds to an area of 150,000 km^2). The SSI accounts for the scaled exceedance of the local 98th percentile of surface wind speeds $v_{k,t}$. This percentile at each grid point $v_{k,98}$ is chosen with the assumption that storm damages occur on 2% of all days (Palutikof and Skellern, 1991). A cubic scaling is applied (Leckebusch et al., 2008), as is commonly used in studies relating to storm losses (e.g. Klawa and Ulbrich, 2003). A storm footprint typically refers to the wind field it imprinted throughout its lifetime, thus the footprint is equivalent to Eq. 1. It is thus dependent on the lifetime of the storm, the total area it covers, and the intensity of the surface wind fields contained in its clusters. An alternative way to develop the footprint is to first transform percentiles to create a distribution-independent SSI, as employed by Walz et al. (2015), who showed that the shape of the tail-end of surface wind speed distributions differs between e.g. oceanic and mountainous regions. However, this is beyond the scope of this study.

Then, we wish to evaluate windstorm footprints in the European region, where the regional boundaries are defined as 10W — 30E, 35 — 65N. A windstorm is considered to be "European" if its cluster center exists in this region for at least four time steps (one day). To quantify the footprint to these regions, Eq. 1 is instead aggregated over the European lifetime of the storm, or T_{EU}. The European footprint of the storm is thus SSI_{EU}. A caveat of this method is that it may underestimate the "true" European footprint for storms at the borders of the European region. For example, a windstorm with its center of mass located just outside the border will have overlapping grid boxes in Europe, but will have no footprint (and vice versa for a center of mass inside the edge of region). However, clusters are rarely so large in size that we will significantly under- or over-estimate the footprint. An example of Kyrill's footprint at one time step in its lifetime is displayed in Figure 5; this is an extreme case of a high footprint, where the storm covers a large part of the European region.

The European footprint is essentially comprised of three components: its average total area, average surface wind speed intensity, and its lifetime. We define the European lifetime-average total area as $\overline{A_{EU}} = n_{EU}^{-1} \sum_\tau A_\tau$, where n_{EU} is the number of timesteps corresponding to T_{EU} and A_τ is the total area covered by the storm at a time step τ within the storm's lifetime. For the intensity, we consider the lifetime-mean cluster-averaged wind intensity as $\overline{v_{\mu,EU}} = n_{EU}^{-1} \sum_\tau v_{\mu,\tau}$, and the lifetime-mean cluster-max wind intensity as $\overline{v_{\max,EU}} = n_{EU}^{-1} \sum_\tau v_{\max,\tau}$, where $v_{\mu,\tau}$ and $v_{\max,\tau}$ are the mean and maximum surface wind speed in the cluster at a time τ, respectively.

The maximum intensification rate of a windstorm is defined as the maximum 6-hourly rate of change of SSI. This can physically represent a combination of a rapid increase in

JAN19 00:00 UTC
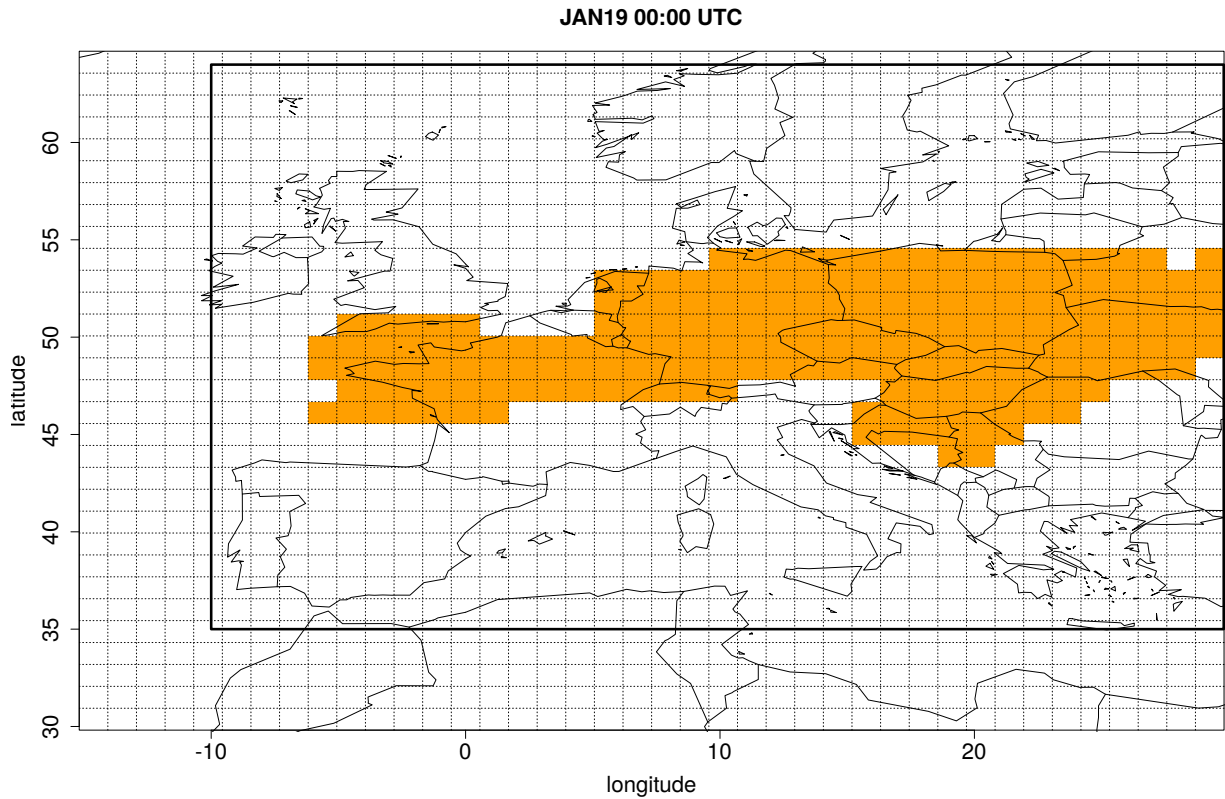
Figure 5: Example of the footprint of the storm Kyrill on 19.01.2007 00:00 UTC, from ERA-20C. The orange grid boxes represent the anomalous surface winds which exceed their local 98th percentiles and are included in the overall grid box cluster. The bold rectangle encloses the European region.

the windstorm's anomalous surface wind field area or an increase in the magnitude of the field itself. A 6-hourly rate was chosen because windstorms typically have short lifetimes and often experience both rapid increases and decreases in their footprint over 6-hourly time steps.

Cyclone tracking

Cyclones are identified and tracked using an objective MSLP-based method, developed by Murray and Simmonds (1991) and adapted for the Northern Hemisphere by Pinto et al. (2005). To begin with, gridded MSLP data is interpolated to a higher-resolution dataset. This is to ensure that the resolution of the data set is higher than a typical cyclone radius. Then, local maxima in the Laplacian of pressure, $\nabla^2 p$ are detected, and the algorithm seeks local pressure minima using a two-dimensional extension of the Newton-Raphson method. If a true minimum exists within a 1200 km radius, the depression is classified as closed: its center is the point of minimum pressure. In the case that no true local pressure minimum exists, however, the algorithm can identify open depressions by locating the point of a minimum pressure gradient associated with concavity. This represents the center of an open depression. After cyclones have been identified, they are filtered by their strength. For open and closed depressions we disregard those which are weaker than $\nabla^2 p = 0.2$ hPa deg. lat.$^{-2}$ and $\nabla^2 p = 0.3$ hPa deg.lat.$^{-2}$, respectively. Cyclones which are too close to another, or those which are localized in an elevation of over 1500 m are additionally discarded.

The final step is to track the position of these cyclones. The most likely new position of the cyclone is estimated using its previous velocity and weighting factors which take into

24

account its memory of past motion and pressure tendencies. Pairs of predicted and new positions are then evaluated by quantifying the distance between them. If this distance is a some critical threshold of 12.5 deg. lat., a probability based upon the distance between them and their pressure differences is assigned. Any cyclones which cannot be paired up to new predicted centers are defined as newly generated or decayed systems.

Cyclone properties

Each cyclone track contains 6-hourly tabulated data of the properties of its core pressure, Laplacian of pressure, geographical coordinates, information about its status (i.e. closed/open and weak/strong), its steering velocity, and the probability that the predicted and new cyclone positions are the same. Unlike the windstorm footprint, cyclone characteristics are considered over its entire lifetime. We are interested to know whether cyclone characteristics further upstream (even outside of Europe) are in some way related to a high SSI_{EU}.

Throughout the lifetime of a cyclone, its peak intensity can be described either as its minimum core pressure p_{min} or its maximum Laplacian of pressure, $[\nabla^2 p]_{max}$ – both quantities are commonly used to measure cyclone strength (e.g. Wang et al., 2006). The intensification rate of the cyclone can be considered either in terms of its pressure or Laplacian of pressure. Therefore, we define two quantities: the deepening rate (DR) and intensification rate (IR), defined as the maximum rate 6-hourly rate of change of p and $\nabla^2 p$, respectively. A 6-hourly window was chosen to match that of its daughter windstorm. Following Sanders and Gyakum (1980), the DR has been normalized by a factor of $\sin 60° / \sin \phi$, where ϕ is the latitude of the cyclone. This is to account for the increase in planetary vorticity as one moves polewards (accompanied by a decrease in relative vorticity).

Cyclone and windstorm matching

The procedure used to objectively match each windstorm to a unique cyclone is based on Nissen et al. (2010) and is described here. It is broken down into three primary iterations. In the first iteration, windstorm tracks which are related to a single cyclone are matched by identifying overlapping periods of the windstorm track with all possible cyclone tracks. These cyclones must have been closed and stronger than 0.6 hPa deg. lat.$^{-2}$ in their lifetime. If multiple cyclones detected within an 800 km radius of the windstorm are found, the cyclone with the strongest Laplacian of pressure is chosen. Otherwise, a radius of 1200 km is used — this threshold corresponds to the cyclone tracking scheme search radius. If the windstorm cannot be uniquely matched and is connected to multiple, consecutive depressions, the second iteration begins. Windstorms are matched to cyclones with the greatest coexistent lifetime within a mean distance of 1200 km. Finally, the last iteration repeats the second iteration but for open depressions. A storm footprint refers to the windstorm's footprint, and its generation and intensification refers to that of the cyclone unless specified otherwise. A small number of windstorms will not able to be matched, either because of systems leaving the area of interest or accidental matching of multiple windstorm tracks.

Identification of bomb cyclones

Explosive cyclones are those which undergo a rapid deepening phase and are often referred to as "bombs" (Sanders and Gyakum, 1980). The definition for the criteria of a bomb is described by the Bergeron condition. If the 24-hour pressure drop Δp_{24hr} satisfies the inequality $\Delta p_{24hr} \geq 24$ hPa $\times \sin \phi / \sin 45°$, it is classified as a bomb.

2.3   Storm data

Following the tracking and matching schemes as applied to the Northern Hemisphere (above 20° N), we track a total of 64186 and 20994 storms in three members of MPI-ESM-LR and ERA-20C, respectively. We were left with a total of 9077 and 4640 untracked windstorms, respectively. A cursory glance at the total footprint of these unmatched windstorms showed that their SSIs were on average 57% and 58% weaker than the matched windstorms for the respective data sets. Moreover, these unmatched storms had lifetimes that were 77% and 71% shorter than matched windstorms. Returning to the matched systems, after we filter for European systems we arrive at a total of 5164 and 1550 storms for MPI-ESM-LR and ERA-20C, respectively.

On the subject of regional dependencies, when this study was repeated with a European region that is shifted to the West, South, or East by 10°, the results to follow and their interpretation were extremely similar and will not be shown. However, shifting it North changes the behaviour such that we have increased numbers of storms and average footprints (we do not continue with this Northern extension, as it includes Arctic systems which are beyond the scope of this study).

2.4 Interannual behaviour

One of the stated goals of the thesis is to highlight the stark range of European windstorm footprint magnitudes that exist, and how they compare to the frequently-analyzed windstorm counts. With the construction of the storm footprint, we demonstrate here how the winter-aggregated European footprint of these storms compares with interannual variability of windstorm counts. Note that these are all windstorms which have been explicitly matched to a cyclone and satisfy all the requirements described in Section 2.2.

For each data set, all winter European windstorms' footprints are cumulatively added in their respective ONDJFMs; define this sum of footprints as the "storminess". We repeat this for each year to obtain a time series of storminess against each winter, which is shown in Figure 6. This is accompanied by Table 1 which computes relevant correlations and trend statistics. All four time series show storminess and storm counts with similar amplitudes, with a slight increase in the mean number of storms in the historical ensemble members. Visually we can see a particularly strong interannual frequency, with both windstorm numbers and storminess rapidly changing between years. We can further see years where increases in storm count do not correspond to an increase in storminess, but instead a decrease (e.g. 1979 in ERA-20C, or 1980 in MPI-ESM-LR 1). In general, although storminess and windstorm counts show a strong correlation in both data sets, there is still another part of the picture: the distribution of footprints of individual storms, which we will soon investigate.

In ERA-20C, there is a statistically significant positive linear trend in storminess which is comparatively stronger compared to the trend in counts. Conversely, these trends are not significant, and lower in magnitude for all three members of MPI-ESM-LR. MPI-ESM-LR member 1 interestingly shows a positive storminess slope, but the slopes are negative and near zero for members 2 and 3. This is despite the external forcings applied to the historical runs from model year 1850 onward. Lastly, the variance explained by a linear fit is only significant for ERA-20C data, as indicated by the R^2 values and their significance. These findings are similar to those of Kruschke et al. (2016), who found no significant windstorm count trends in MPI-ESM-LR, but one in a mixed ERA reanalysis (utilizing both ERA-Interim and ERA-40). Befort et al. (2016) additionally find positive trends in windstorm counts in a similar time period over Europe for ERA-20C. In their review paper of extratropical cyclones in a changing climate, Ulbrich et al. (2009) show that many studies see an increase in the activity of extreme cyclones over time. However, as the definition of an extreme system is important when studying changes in cyclone behaviour over time, they suggest to exercise caution. For instance, one may find opposing trends when defining cyclones by core pressure instead of the Laplacian of pressure.

One possible reason for these disagreements between data sets is the nature in which the historical runs are initialized. These runs are initialized 50 years apart in the pre-industrial control, and are likely situated in different phases of low frequency modes of variability like the Atlantic Multidecadal Oscillation (AMO). The AMO represents the basin-wide SST anomaly changes in the North Atlantic on decadal scales. For example, Yamamoto and Palter (2016) show that negative AMO phases are related to more zonally elonated storm tracks in the Atlantic. The AMO is further related to variations in the meridional overturning circulation (Knight et al., 2005). This circulation is known to affect the frequency

of windstorms (and thus, the annual storminess) on multi-decadal scales (Nissen et al., 2014). A given historical ensemble member could be run in such a way that its AMO in the model years 1950 — 2005 counteracts any positive trends potentially forced by external forcings.

Data	C	Storminess slope	Counts slope	R^2 storminess	R^2 counts
ERA20C	0.71*	0.91*	0.094*	0.13*	0.053*
MPI-ESM-LR 1	0.57	0.41	0.0020	0.0074	10^{-5}
MPI-ESM-LR 2	0.58	-0.18	-0.052	10^{-3}	0.0056
MPI-ESM-LR 3	0.44	-0.022	-0.054	10^{-4}	0.010

Table 1: Summary of statistics for interannual storminess and counts. C is the correlation between the storminess and counts. The slope of each series' trend is shown, along with R^2 values. Values with asterix (*) are significant to $p < 0.05$.

We now wish to see how stormy and non-stormy years depend on the number and/or footprint of windstorms, and we will demonstrate how this justifies the need to study windstorm footprints in addition to their frequency. First, the storminess time series is separated into stormy and non-stormy years using upper and lower thresholds defined by the mean $\pm$ standard deviation of storminess in each respective data set. Then, we can study a breakdown of the windstorms and their footprints that contributed to that year's storminess. Figure 7 displays how individual windstorms contribute to the each year's total storminess for ERA-20C, and Figure 8 for the first ensemble member of MPI-ESM-LR (the other two are not shown here, but displayed very similar results).

In ERA-20C, we can identify a number of prominent windstorms. For example, in the winter of 1999, we find the storms Martin, Lothar, and Anatol with footprints of 38.98, 23.89, and 17.77 units respectively. Other notable storms such as Vincinette in 1962 (footprint of 56.32), Daria in 1989 (footprint of 30.45), and Kyrill in 2007 (footprint of 36.81) can be seen. Further, each stormy year contains at least one storm that exceeds the 95th percentile (to gain a sense of what footprint magnitude constitutes an anomalously strong windstorm, the 95th percentile of these windstorm footprints is 15.83 units). In the non-stormy years, there are generally less storms, and by comparison lower maximum footprints apart from 1995 with one anomalous storm of footprint 26.80. In the first ensemble member of MPI-ESM-LR, every stormy year also contains at least one windstorm which exceeds its 95th footprint percentile of 12.43. By comparison, the maximum windstorm footprint in non-stormy years is generally quite low, and there are fewer windstorms overall.

However, there is the case to be made that stormy years do not necessarily align with years of high windstorm frequency. For example, the total storminess of the year 1961 in ERA-20C is 186.42 units, but is comprised of only 27 windstorms (which is close to the mean of 26 windstorm counts). In contrast, the year 1981 has a slightly lower storminess of 164.87 units, but 34 windstorms (which is above the 75th percentile of windstorm counts). In the first member of MPI-ESM-LR, the years 1976 and 1977 have total storminess values of 153.53 and 168.08, respectively, but counts of only 31 (equal to the mean). Altogether this demonstrates that studying the interannual variability of windstorm counts alone does not provide the full picture of how severe that season was: some years only require a few extremely powerful storms to create a high total footprint.
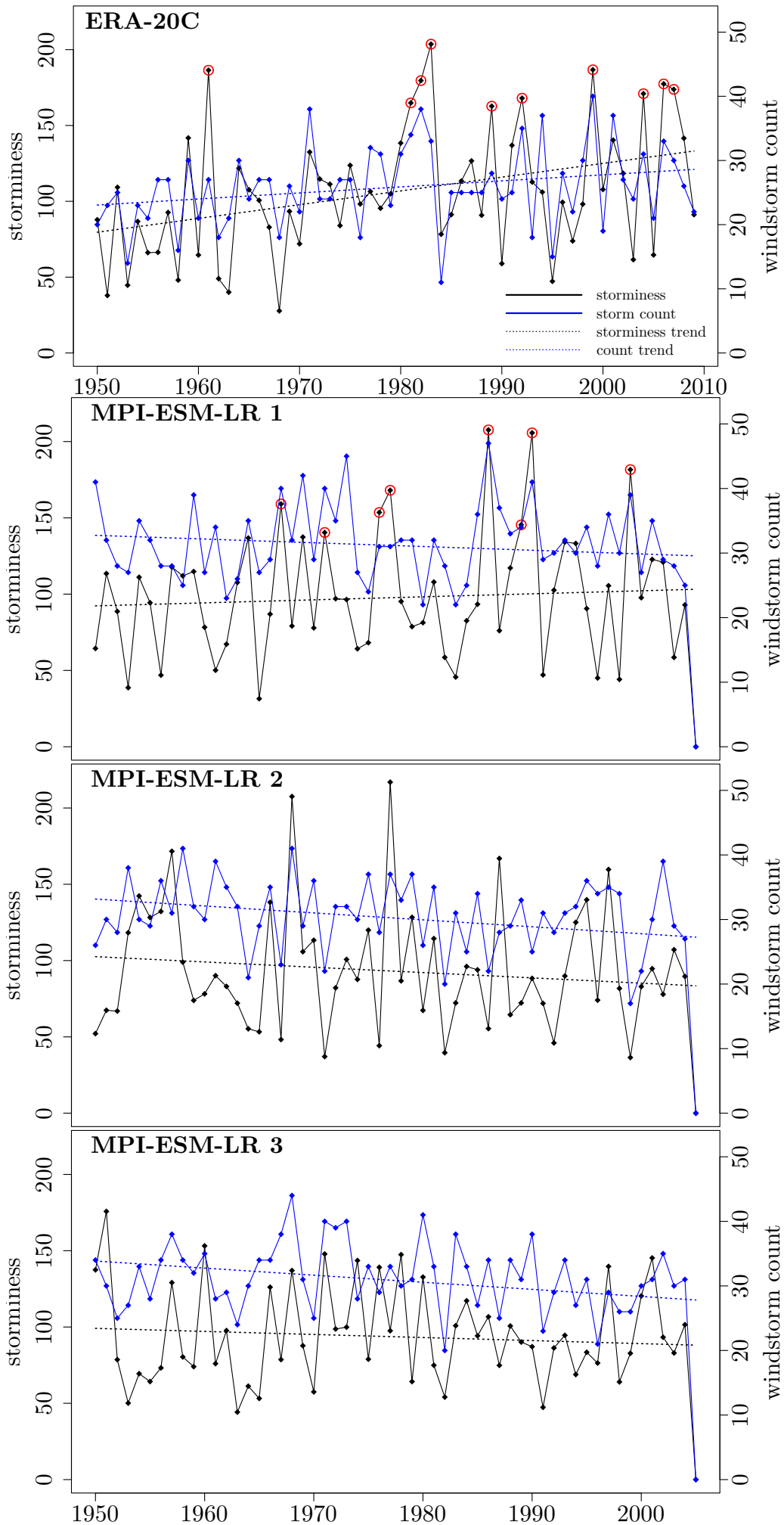
Figure 6: Winter-aggregated European windstorm footprint ("storminess", black) and windstorm counts (blue) every winter (ordinate), for ERA-20C and each MPI-ESM-LR ensemble member. Dashed lines are linear trends for the respective variable. Red circles indicate examples of anomalously stormy years shown in Figures 7 and 8.
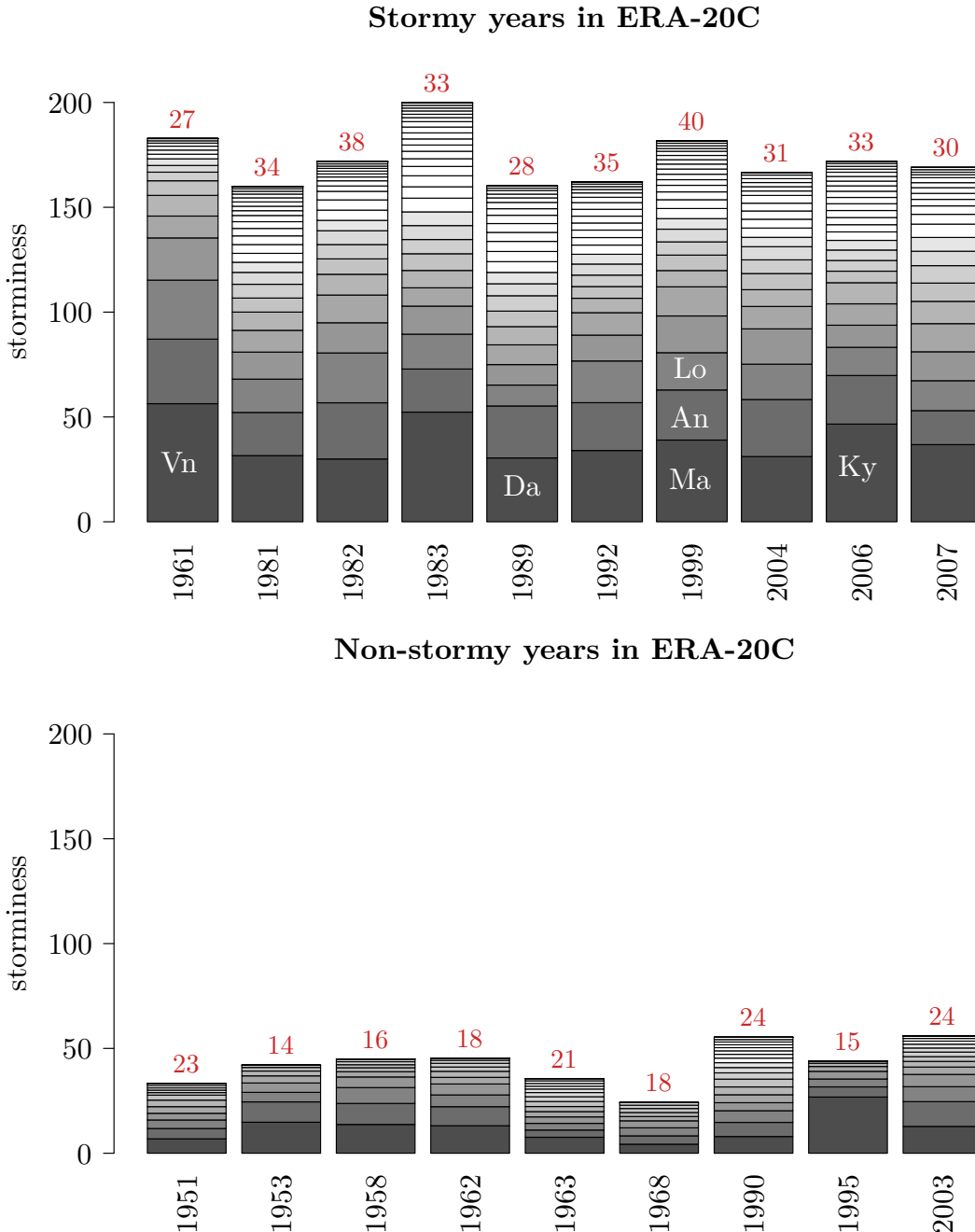
Figure 7: Contribution of each European windstorm's footprint (individual bars) to the year's total European storminess in dimensionless units, for stormy years (top) and non-stormy years (bottom). The red numbers at the top of each bar stack represent the number of European storms in that year. Examples of prominent destructive European windstorms and their contribution are shown in the top figure, for Vincinette (Vn), Daria (Da), Lothar (Lo), Martin (Ma), Anatol (An), and Kyrill (Ky).

2.5 Relationships in windstorm-cyclone pairs

To provide a complete picture of how dynamical factors affect the cyclones which produce high footprint windstorms, we first wish to describe the prevailing relationships between windstorms and their parent cyclones. First, we identify how the windstorm footprint depends on its own constituents, as displayed by correlations in Table 2. The windstorm lifetime and $\overline{A_{EU}}$ contributes the most to its footprint, whereas $\overline{v_{\max,EU}}$ and $\overline{v_{\mu,EU}}$ contribute a negligible amount. This is consistent in both ERA-20C and MPI-ESM-LR. These results show that a high footprint windstorm must be associated with a widespread anomalous wind field that maximizes its time in the European region. However, increases in the wind field intensities only marginally increases the footprint magnitude.
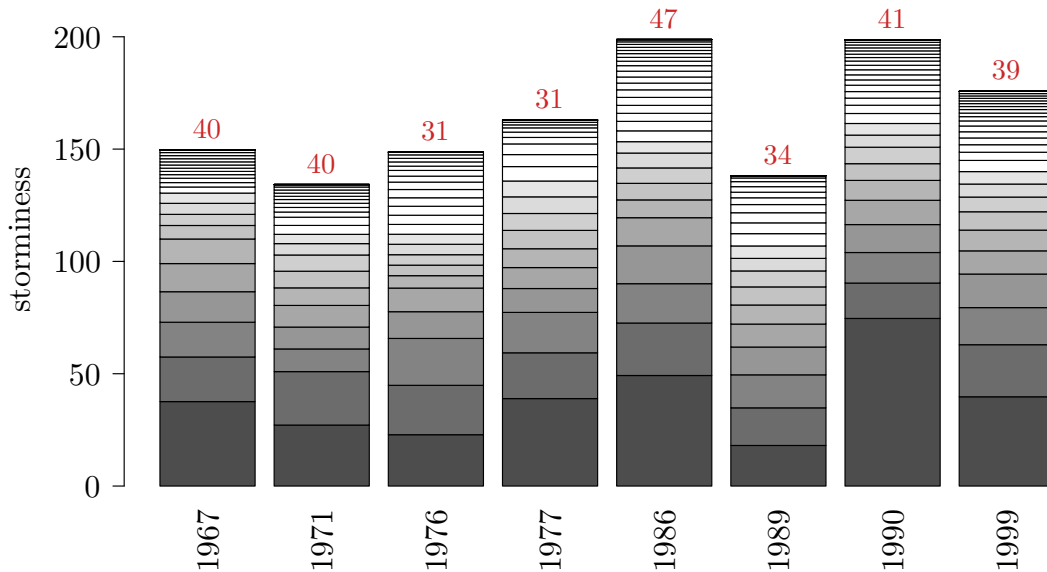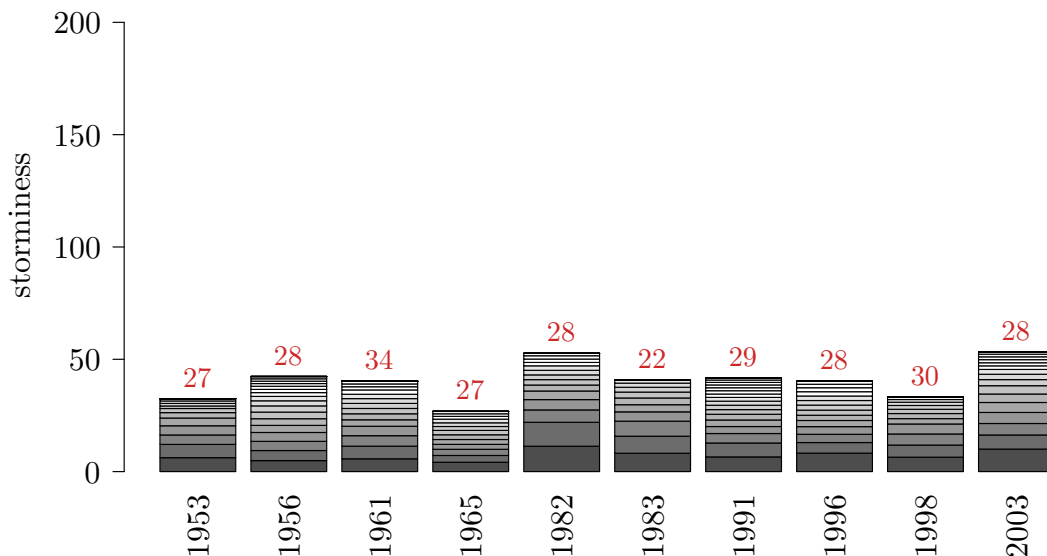
Figure 8: As Fig. 7, but for the first MPI-ESM-LR historical member.

Windstorm Property	SSI$_{EU}$ correlation (MPI-ESM-LR)	SSI$_{EU}$ correlation (ERA-20C)
$\overline{v_{max,EU}}$	0.30	0.15
$\overline{v_{\mu,EU}}$	0.04	-0.11
$\overline{A_{EU}}$	0.71	0.66
Wind. Lifetime	0.41	0.44

Table 2: Pearson's correlation coefficient of SSI$_{EU}$ with individual storm properties, all significant to $p < 0.05$.

The relationships between windstorm and cyclone properties are shown in the correlation matrix (Table 3). With respect to the windstorm properties, both the minimum core pressure and maximum vorticity show very similar correlations (with reversed sign). However, the max intensification rate (IR) and deepening rate (DR) are slightly different, DR showing higher absolute correlations in general. Correlations between any cyclone property and SSI_{EU} are significant but relatively low, but correlations between these properties and $\overline{A_{EU}}$, $\overline{v_{\max,EU}}$, $\overline{v_{\mu,EU}}$ are higher. In addition, longer-lasting cyclones are not necessarily related to

Data set	MPI-ESM-LR					ERA-20C				
Cyclone / Windstorm Property	SSI_{EU}	$\overline{v_{max,EU}}$	$\overline{v_{\mu,EU}}$	$\overline{A_{EU}}$	Wind. Lifetime	SSI_{EU}	$\overline{v_{max,EU}}$	$\overline{v_{\mu,EU}}$	$\overline{A_{EU}}$	Wind. Lifetime
Maximum vorticity	0.22	0.41	0.35	0.24	0.09	0.12	0.52	0.42	0.27	0.07
Minimum core pressure	-0.24	-0.45	-0.37	-0.37	-0.08	-0.14	-0.56	-0.43	-0.39	-0.06
Max IR	0.17	0.26	0.21	0.19	0.04	0.08	0.32	0.24	0.21	0.07
Max DR	-0.23	-0.32	-0.23	-0.27	-0.07	-0.19	-0.40	-0.28	-0.31	-0.05
Cyc. Lifetime	0.09	0.14	0.11	0.10	0.11	0.09	0.20	0.14	0.13	0.11

Table 3: Correlations of cyclone properties (rows) with windstorm properties (columns), split into MPI-ESM-LR and ERA-20C data. All values are significant to $p < 0.05$.

longer-lasting European windstorms as evidenced by the low correlations between lifetimes. The limitations of studying $\overline{v_{\max,EU}}$ and $\overline{v_{\mu,EU}}$ are that surface wind percentiles can vary strongly between grid points (e.g. ocean points have much higher percentiles), thus assessing the strength of a windstorm from the absolute wind speed alone is difficult.

To summarize, tables 2 and 3 provide a general picture of the main quantities that contribute to a high European windstorm footprint. In terms of windstorm properties, both data sets agree that a high footprint requires a high windstorm lifetime and a widespread windfield, with a reduced dependence on the wind intensity itself. In terms of cyclone properties, despite the fact the area and intensity of the windfield strongly depend on cyclone intensities, the footprint itself shows no strong dependencies on any one property. This is because the windstorm lifetime poorly correlates with all properties. To build upon this further, high footprint windstorms can be associated with all kinds of cyclones, so that the footprint primarily depends on the timing in which a cyclone enters Europe during stronger phases. For example, a weaker cyclone that successfully intensifies as it enters Europe can imprint a similar footprint to a much stronger cyclone that intensified upstream (and hence too early). This implies that the window in which a cyclone maximizes its intensity over Europe is crucial as the windstorm only exists for far less time by comparison. The mean cyclone lifetime in both data sets is 6.2 / 6.7 days for MPI-ESM-LR and ERA-20C, respectively, over four times longer than their daughter windstorms with mean lifetimes of ~1.5 days.

Correlations only provide a linear relationship between quantities. A different picture emerges if we consider, for example, the extremes of windstorm footprints, defined as the highest and lowest 5% footprint of storms. Empirical cumulative density function (ECDF) curves for different cyclone properties are constructed for these two classes of windstorms, as displayed in Figure 9. These relationships become much clearer. For both MPI-ESM-LR and ERA-20C, higher maximum vorticities and more intense growth rates are associated with higher footprint windstorms and vice versa. Lifetimes are higher for high footprint storms, but not substantially.

Lastly, we can relate windstorm footprints to the occurrence of bomb cyclones, which are typically cyclones with higher maximum intensities (Trigo, 2006). Figure 10 directly compares quantiles of windstorm footprints for windstorms associated with bomb cyclones and non-bomb cyclones, where the diagonal line represents the line of equal quantiles between both cases. The actual values are shifted towards the windstorm footprint quantiles of bomb cyclones, indicating that these quantiles are higher compared to non-bomb cyclones.

To summarize this section, we have found that a windstorm's European footprint is partially related to the intensity and growth rates of its parent cyclone (especially at its
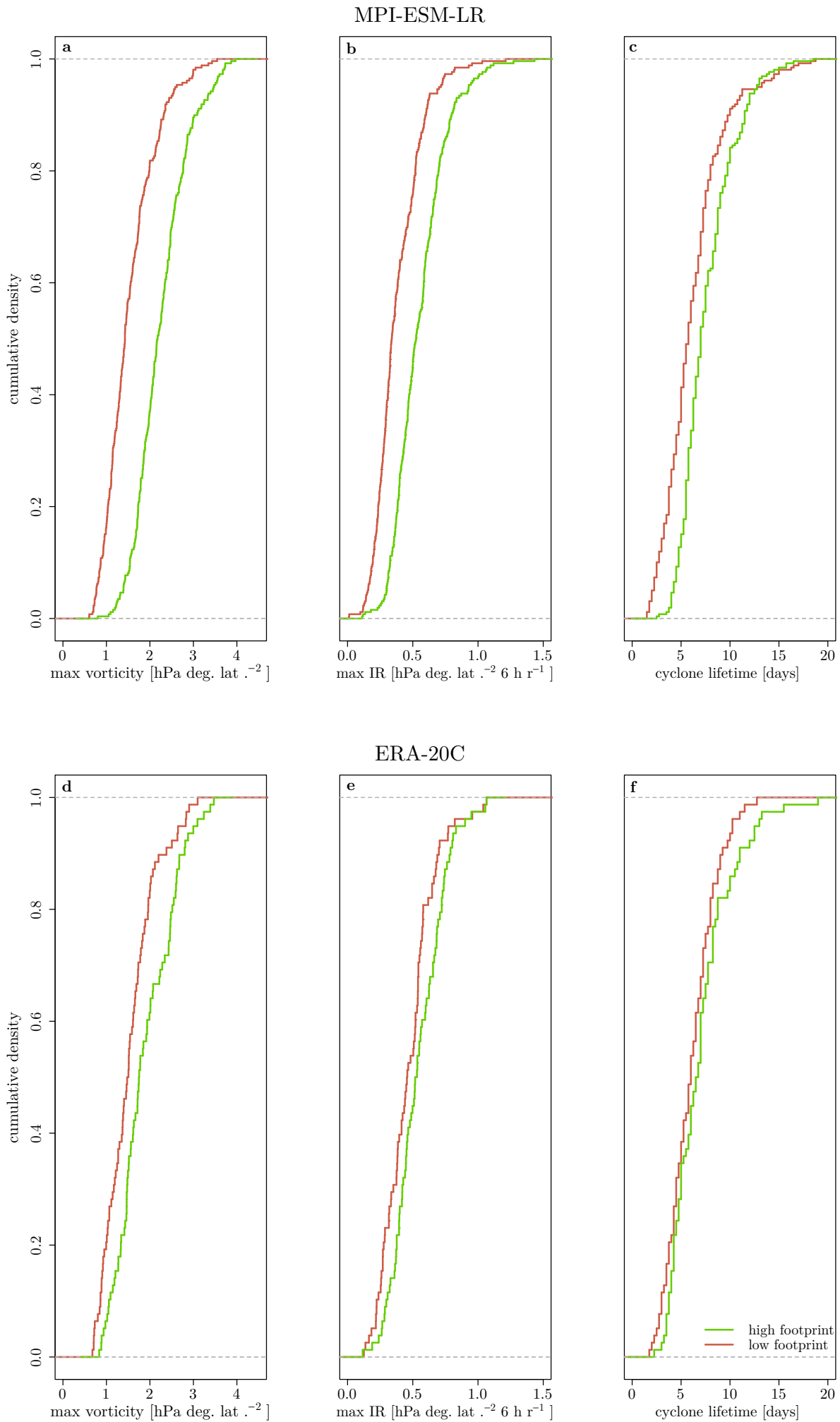
Figure 9: Empirical cumulative density functions for the maximum vorticity (a, d), maximum IR (b,e), and cyclone lifetime (c, f) for high SSI_{EU} (green) or low SSI_{EU} (red) windstorms. Top: MPI-ESM-LR data with $n = 259$, bottom: ERA-20C with $n = 78$. A Welch two-sample t-test confirms that the means of each pair of data were significantly different from one another.
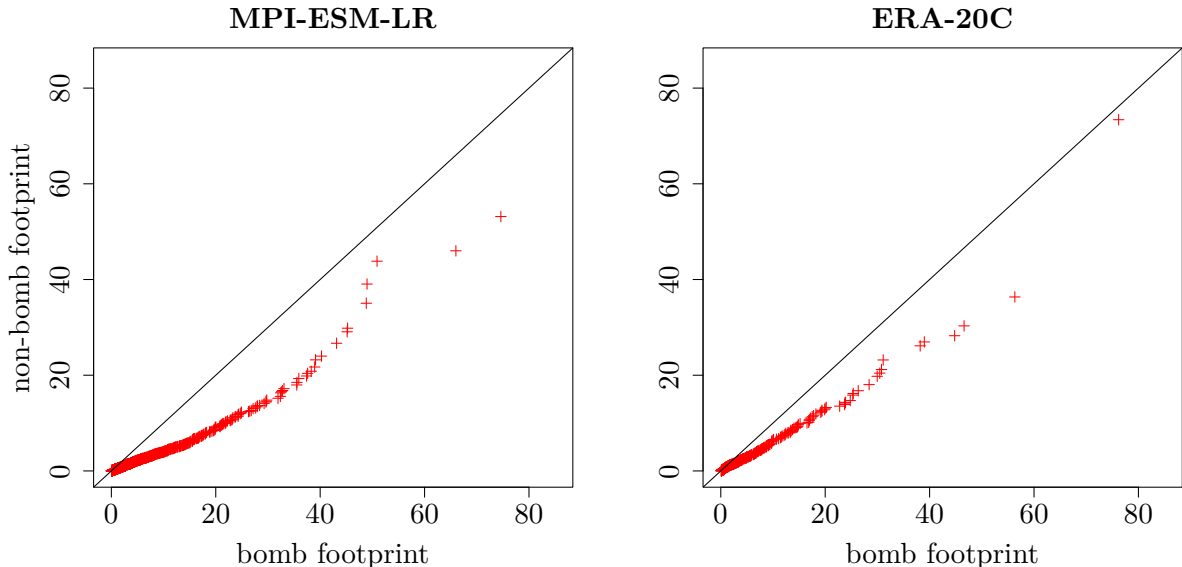
Figure 10: QQ-plot of SSI$_{EU}$ related to bomb or non-bomb cyclones for MPI-ESM-LR and ERA-20C. The former data includes 1172 bomb and 3992 non-bomb values, and the latter 352 bomb and 1198 non-bomb values. The black diagonal line represents the line of equal quantiles, and the red + symbols are the actual values from the data.

extremes). However, the footprint is primarily dependent on the lifetime of the windstorm, which itself is maximized depending on when and where the windstorm intensifies with respect to a specified region. This necessitates a deeper understanding of how windstorm growth relates to their parent cyclones, and where high footprint systems generate, intensify, and travel. These concepts will be explored in the following two sections.

2.6   Growth behaviours of cyclones and windstorms

One feature we would like to elucidate is the role of a cyclone's growth on that of its daughter windstorm. This allows us to paint a clearer picture of exactly how a windstorm evolves with respect to the strength of the cyclone. To do this, we start by looking at an example life cycle of the cyclone-windstorm system corresponding to the storm Anatol, displayed in Figure 11. Anatol was a prominent storm system which caused substantial losses due to high surface winds (Ulbrich et al., 2001). Its cyclone originated over the central North Atlantic before it rapidly intensified further east, entering Europe with a high intensity. The intensities of both systems are plotted over time, which itself is represented on a 6-hourly scale since cyclogenesis at 1999-21-01 00:00 UTC. Anatol is a good example of a storm system with a clear trajectory, and one which will help us define growth-related variables to be expanded upon in the following sections.

There are a number of interesting features in Anatol's cyclone and windstorm growth curves. Following the genesis of the cyclone upstream over the central North Atlantic ocean, it slowly intensifies over a period of 48 hours before its daughter windstorm forms. By looking at where the right red dashed line intersects with the cyclone intensity curve, we see that the windstorm forms at a cyclone strength of $\nabla^2 p \sim 1.0$. More importantly, the storm pair enters the European region six hours later, in which the cyclone experiences its maximum intensification. Six hours after this, the windstorm itself experiences maximum

34
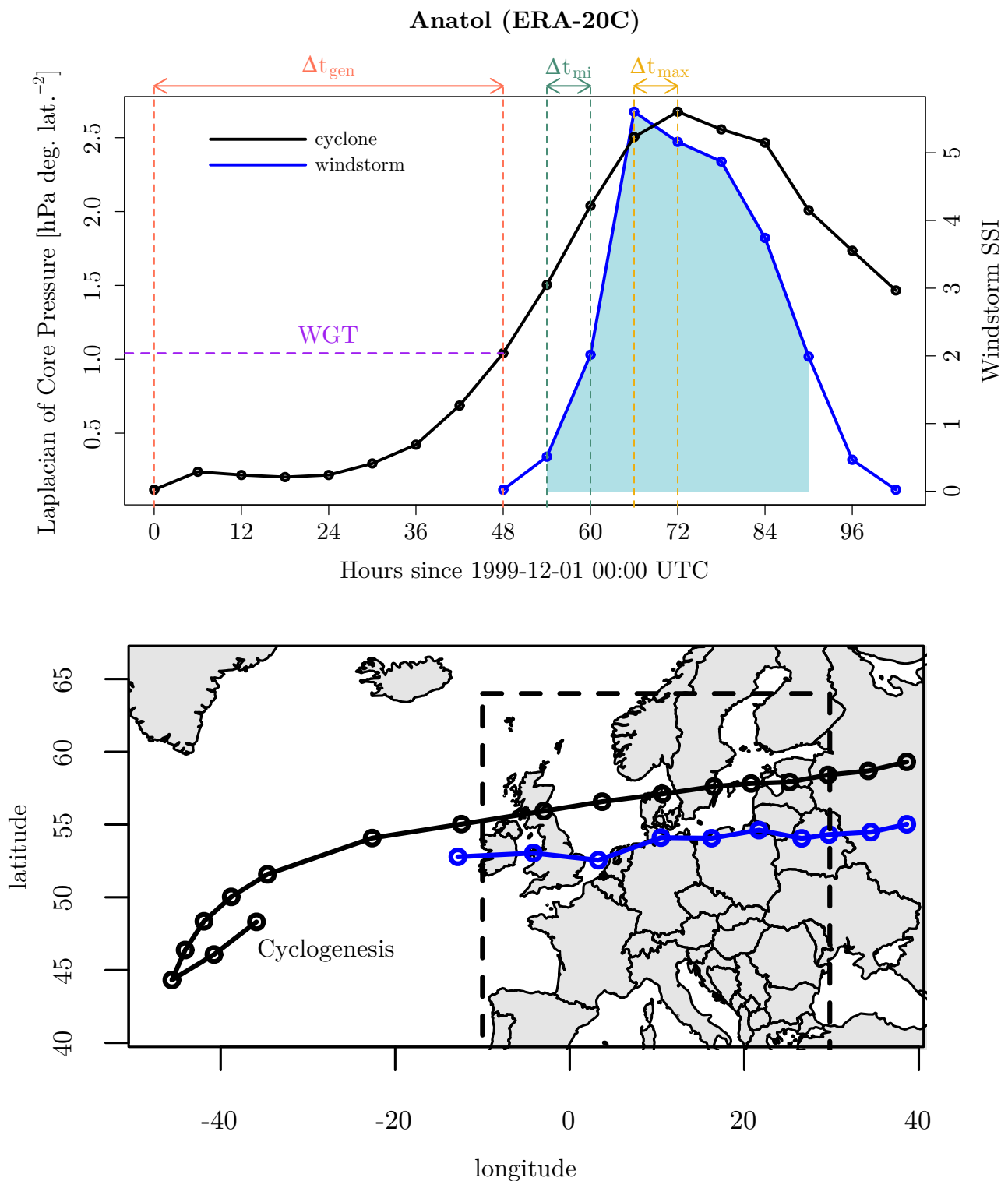
Figure 11: Growth curves (top) of the cyclone (black line) and its daughter windstorm (blue line) for the storm Anatol, starting on 12-01-1999 00:00 UTC. The left axis corresponds to the cyclone Laplacian of core pressure, and the right axis the windstorm SSI. The genesis separation Δt_{gen} (red), maximum intensification separation Δt_{mi} (blue), and the maximum intensity separation Δt_{max} (orange) are indicated by horizontal arrows (colour coded by each variable), with dashed vertical lines to indicate the temporal separation. The light blue shaded area underneath the windstorm curve represents the European footprint of the storm. The purple dashed line connects the Laplacian of the cyclone at the time its windstorm forms, i.e. the windstorm generation threshold (WGT). The corresponding track (bottom) of Anatol's cyclone (black) and windstorm (blue) is also shown.

intensification, before the windstorm reaches its peak intensity at hour 66 after cyclogenesis, and the cyclone at hour 72. Merely 18 hours after its genesis, the windstorm enters its lysis phase, before disappearing 36 hours later. The lysis phase of the cyclone lasts far longer in comparison (and extends further than the x-axis, but is not shown). Given the extreme nature of windstorms, it is expected to decay or disappear during periods of below-average cyclone intensities. Most importantly, the windstorm passed through Europe during its high-intensity phase. From this description, we are therefore interested in the following four features:

- Δt_{max}, the maximum intensity separation, is the separation between the peak vorticity (or minimum core pressure) of the cyclone and the windstorm maximum SSI.

- Δt_{mi}, the maximum intensification rate separation, is the separation between the maximum 6-hourly rate of change of vorticity[1] and the maximum 6-hourly rate of change of SSI.

- Δt_{gen}, the genesis separation, is defined as the time between cyclone and windstorm genesis.

- WGT, or the Windstorm Generation Threshold, is defined as the cyclone vorticity at the time the windstorm first generates.

Positive values of the temporal separation quantities indicate that the windstorm lags the cyclone. This section will compute statistics to explore the general behaviour of these features across all the systems. Windstorms studied here are the same in section 2.5, except we consider the whole windstorm lifetime (instead of just its European segment).

Fig. 12 contains ECDFs displaying quantiles of Δt_{max}, with a mean of -2.22 and 3.69 hours for MPI-ESM-LR and ERA-20C, respectively. For Δt_{mi}, this is -4.31 and +3.37 hours. Although the mean separation is small, it would appear that MPI-ESM-LR windstorms peak in growth and intensity shortly before their parent cyclone. The inter-quartile range displayed by the two vertical dashed lines shows that, in both MPI-ESM-LR and ERA-20C, the majority of windstorm/cyclone pairs reach peak intensity within a $\sim \pm 18$ hour window of each other. Fig. 3b, which instead shows ECDFs of Δt_{mi}, shows that the two systems further experience maximum growth around the same time as one other. Bengtsson et al. (2009) similarly found that near-surface level winds peak in their intensity, on average, around the same time that the cyclone reaches its maximum vorticity. In both data sets, approximately 35% of storms intensify in a window greater than ± 24 hours, and a small 15% of storms in a window greater than ± 48 hours. One reason for the large separations is that some cyclone growth curves can experience secondary cyclone intensification phases, and the windstorm could possibly form near the weaker intensification phase.

Fig. 13 also displays histograms of WGTs. The mean WGT is 1.07 hPa deg. lat.$^{-2}$ and 0.95 hPa deg. lat.$^{-2}$ for MPI-ESM-LR and ERA-20C, respectively. This is greater than the average $\nabla^2 p$ over all tracked cyclones, which is 0.99 and 0.67 hPa deg. lat.$^{-2}$, respectively. This is comparable to Nissen et al. (2010), who find that the number of windstorm-generating cyclones increases as one moves into $\nabla^2 p \geq 1.0$ hPa deg. lat.$^{-2}$. For the higher WGTs in Fig.

---

[1]Note that core pressure can additionally be used here, and for brevity has been omitted from the following sections as it exhibited markedly similar behaviour to vorticity.
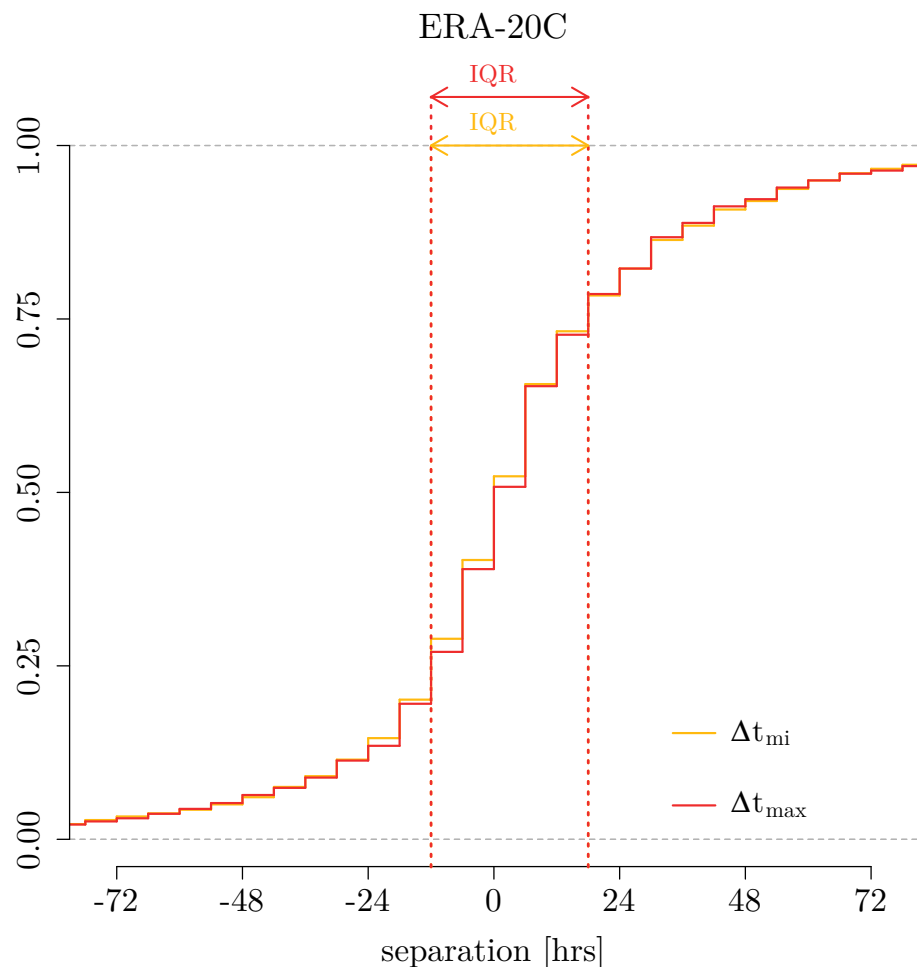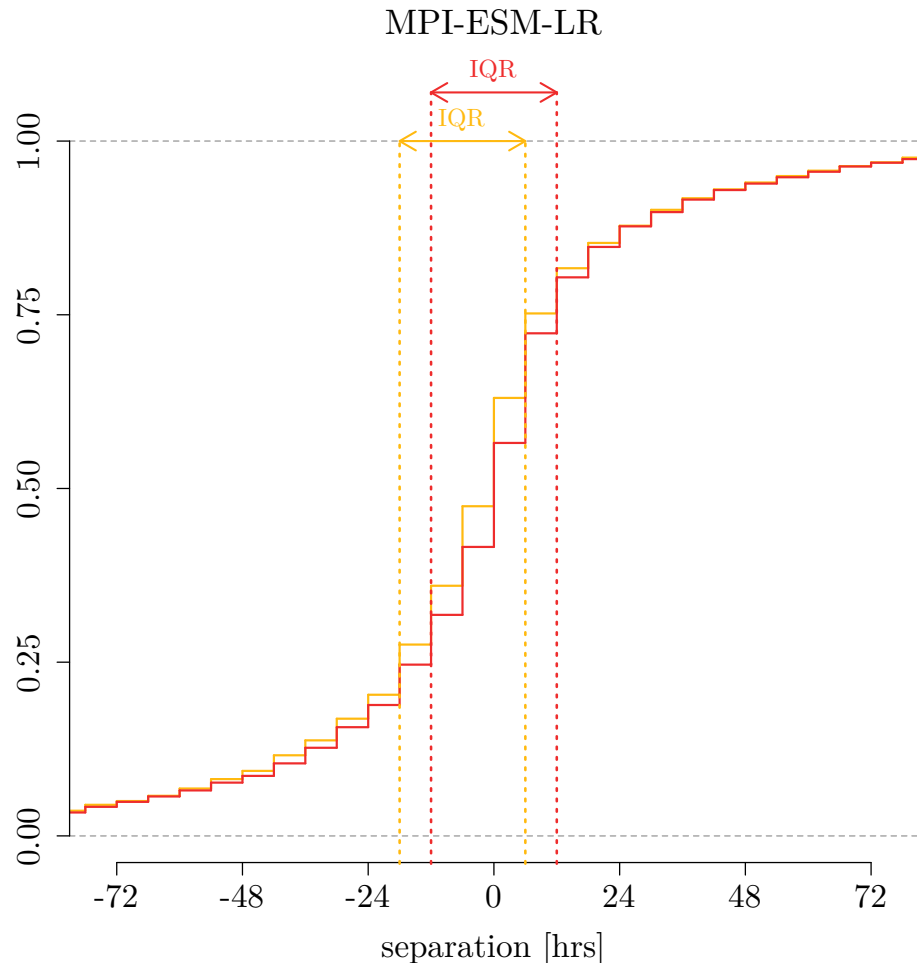
Figure 12: Empirical cumulative density functions for Δt_{max} (red) and Δt_{mi} (yellow) for MPI-ESM-LR (top) and ERA-20C (bottom). Vertical dotted lines enclose the inter-quartile range for each respective data set.

13, this implies that the windstorm only formed for extremely vigorous cyclones. In these scenarios, it could be that the cyclone is situated in a region where local surface wind speed 98th percentiles are very high, such as the open ocean; land percentiles are much lower by comparison. Although the mean WGT differs between the two data sets, it is small enough such that there are unlikely to be significantly different dynamical explanations. Fig. 13 also shows an exponentially-distributed Δt_{gen} for both model and reanalysis. For MPI-ESM-LR and ERA-20C, the mean values are 1.83 and 1.25 days, respectively.
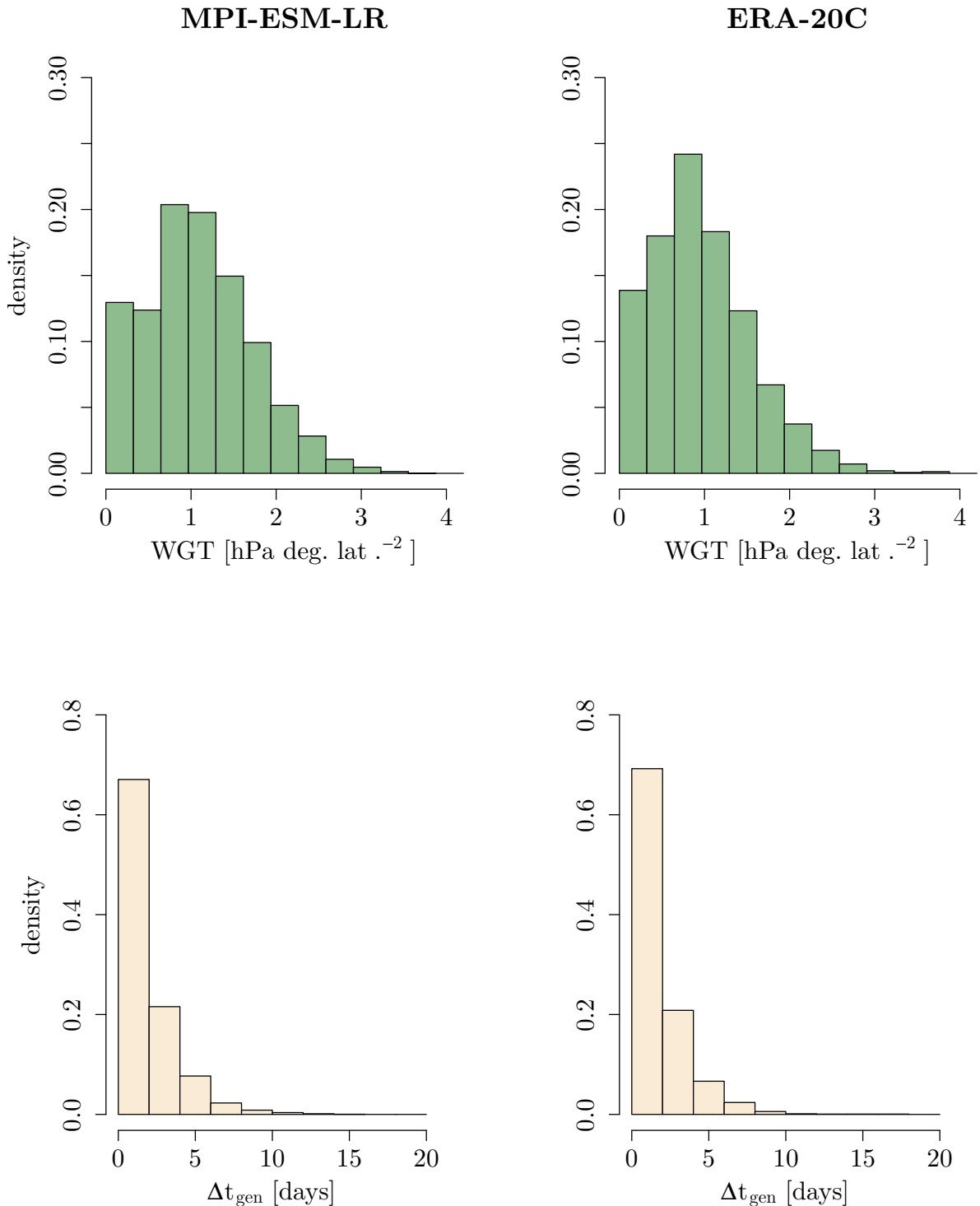
Figure 13: Histograms of WGT (top, in hPa deg. lat.$^{-2}$) and Δt_{gen} (bottom, in days) for MPI-ESM-LR (left) and ERA-20C (right) results.

These results collectively explain a typical life cycle of a cyclone and windstorm pair in MPI-ESM-LR and ERA-20C. Following the genesis of the cyclone, it takes shortly under two days for the cyclone to reach a strength of $0.95 - 1.07$ hPa deg. lat.$^{-2}$, where the windstorm will first generate. Then, the cyclone reaches peak intensification due to forcings in the vicinity of Europe. The windstorm's anomalous surface wind field will expand in

area and/or intensity, increasing its current SSI value rapidly, typically in a one-day window centered on the cyclone maximum intensification. Finally, both systems transition into their respective lysis phases. The windstorm rapidly weakens and disappears, and the cyclone gradually disappears after it.

2.7 Regions of cyclone genesis and intensification

In order to understand how environmental variables could be related to the footprint of a European windstorm, we first need to explore where their parent cyclones formed and intensified. For example, Anatol in Figure 11 showed a cyclone which formed upstream of the North Atlantic ocean before intensifying around the British Isles and entering Europe with a maximized SSI. We begin by identifying the behaviour of all European storms in our data set, as shown in Figure 14.
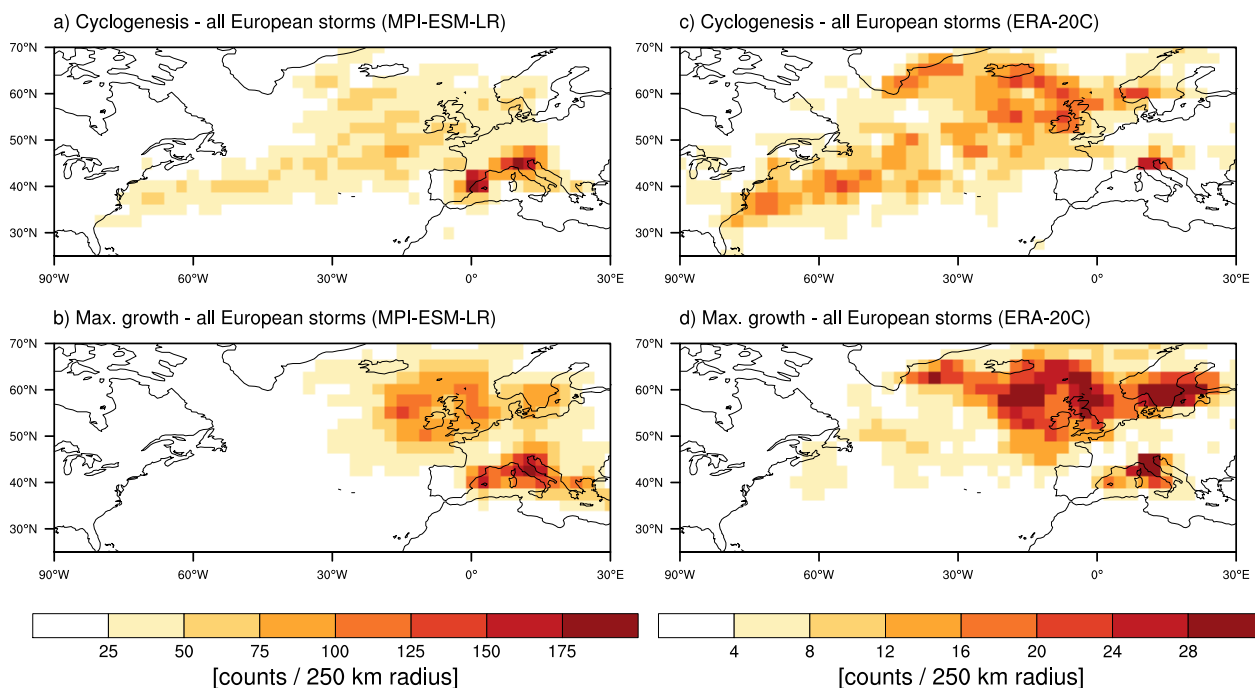
Figure 14: Cyclogenesis densities (top) and maximum growth densities (bottom) for all European storms in MPI-ESM-LR (left) and ERA-20C (right), all in counts within 250 km of each grid point.

Cyclogenesis of European storms is consistent across both sets of data, and shows a signal reminiscent of the North Atlantic storm track. In Figures 14a and 14c, points are fairly uniformly distributed along the storm track, while some areas of the Arctic show cyclogenesis maxima. The difference between MPI-ESM-LR and ERA-20C storms can be seen around Greenland, where the latter shows an increased cyclogenesis density. Further, there are maxima situated around the Mediterranean. In MPI-ESM-LR, two Mediterranean maxima are apparent: one over the Alps, and one in the east of Spain, bordering France. By comparison, ERA-20C only shows a maximum over the Alps.

Sharp maxima of cyclone maximum growth are situated near Europe in both data sets. Two maxima are located around the British Isles and Scandinavia, while another is located again around the Alps. However, the maximum around the British Isles in the MPI-ESM-LR data (Fig 14b) is more concentrated. In ERA-20C (Fig 14d), this maximum is somewhat spread out, with more storms experiencing maximum growth further West (near Iceland) or East (near Sweden). Continuing as we did before, we now wish to see how the cyclogene-

sis and intensification regions of extremely high footprint storms compare to that of lower footprints.

Storm extremes

Figure 15 displays cyclogenesis densities for low and high European footprint storms for both sets of data. From Section 2.5, recall that high and low footprints refer to the extremes above and below the 95th and 5th percentiles of storm footprints, respectively. In Figures 15a and 15c, maxima of cyclogenesis density can be located over the Mediterranean, near Greenland, as well as the Western Boundary Current (WBC) region. Dacre and Gray (2009) similarly showed that explosive cyclones typically generate and/or intensify near Atlantic WBCs. By comparison, Figures 15b and 15d show fewer low footprint storms which generate in this region; they generally form further downstream. This western region is labeled RW with boundaries shown by the dashed black box in 15a. Another important discernible maxima is that of low footprint storms over the Mediterranean in MPI-ESM-LR data, which is not apparent in ERA-20C.
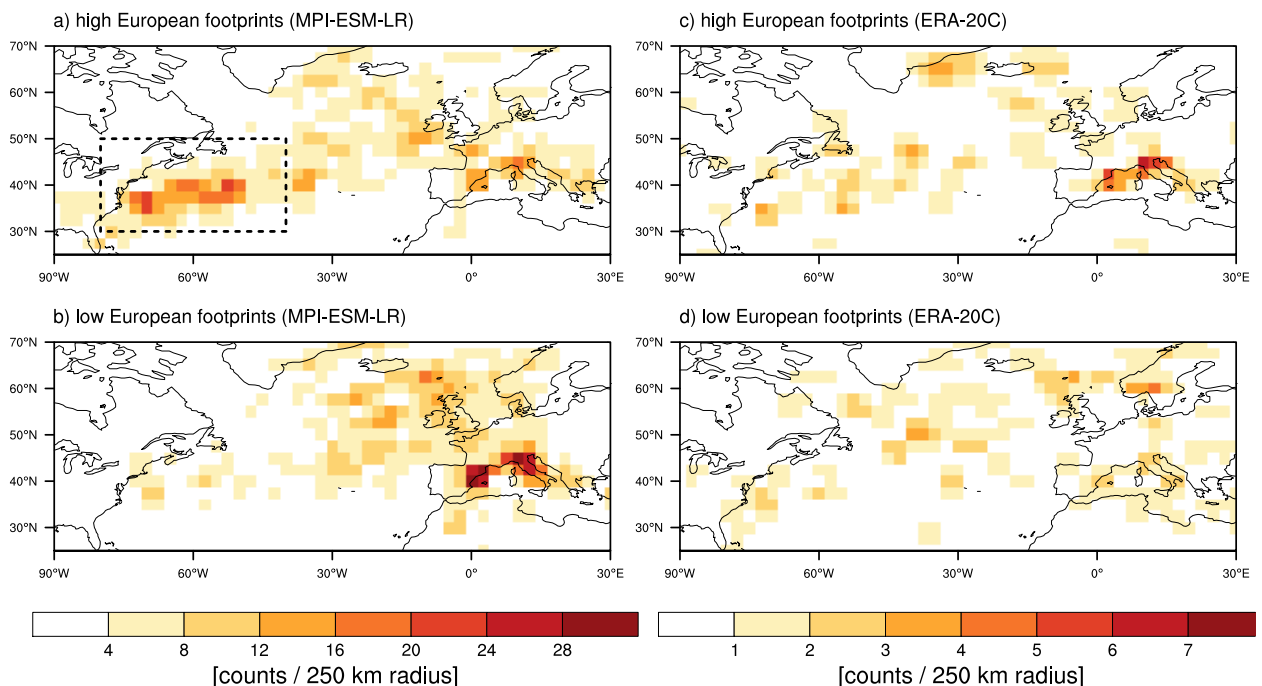
Figure 15: Cyclogenesis densities for high (top) and low (bottom) European footprint storms in MPI-ESM-LR (left) and ERA-20C (right), all in counts within 250 km of each grid point. The dashed box represents the western region (RW, see text) where maxima in cyclogenesis can be identified.

Figure 16 instead shows densities of cyclone maximum intensification for MPI-ESM-LR and ERA-20C. First, we consider the high footprint storms. In MPI-ESM-LR (Figure 16a), density maxima are primarily located on the Western flank of the British Isles and near the Alps. There are additionally a few storms which intensify around the WBC region. ERA-20C is comparatively more complex (Figure 16c) and shows density maxima near the Mediterranean, but more spread around the British Isles, with some storms intensifying on their Western flank, and many over the North Sea. ERA-20C shows density maxima primarily near Greenland and Iceland. From these results, we can identify a key eastern region, RE, defined by the black box in Figure 16a. For the low footprint storms, MPI-ESM-LR shows a very similar pattern compared to high footprint storms (Figure 16b) . ERA-

20C (Figure 16d) instead shows most low footprint storms intensifying closer to Greenland, Iceland, and a few around Canada or Scandinavia.
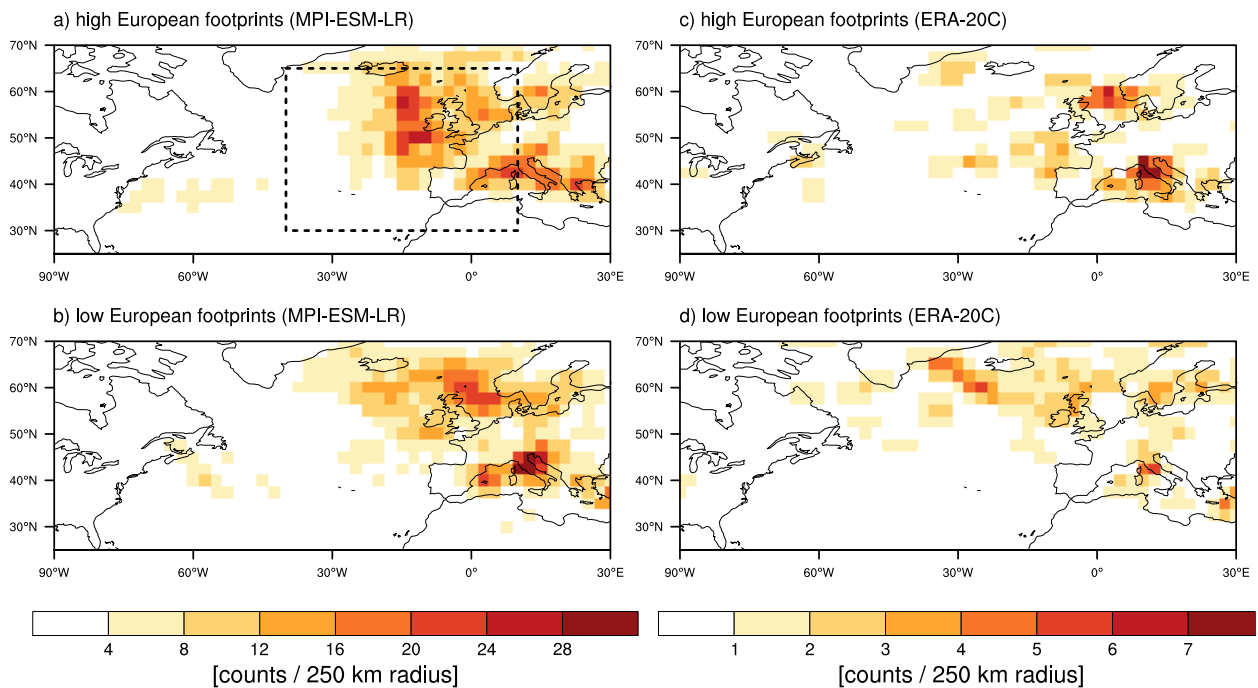
Figure 16: As Figure 15, but for maximum intensification densities.

Constructing storm pathways

Previously we found that high footprint storms prefer to generate in RW or intensify in RE. However, it is possible that storms which generate in RW do not necessarily intensify in RE. This is explored in Figure 17, which visualizes the cyclone track densities and their maximum intensification densities for cyclones which necessarily generate in RW, and form anomalously high footprints in Europe. The majority of these storms follow the typical North Atlantic storm track, while still intensifying around the British Isles. More interestingly, a small number of storms instead experience maximum growth in or near RW. These could be particularly intense storms which are sustained by forcings further downstream, or can undergo a secondary intensification phase.

A number of these anomalously strong storms will generate in the East instead, and their tracks and maximum intensification locations are shown in Figure 18. Two distinct track density maxima can be seen in both MPI-ESM-LR (Fig 18a) and ERA-20C (Fig 18c). One corresponds to storms which pass through the British Isles and through Scandinavia. The other is related to Mediterranean systems, which likely remain in the region, particularly around the Alps and Central Italy. MPI-ESM-LR shows a wider range of track paths, with many more storms traveling through Central-Eastern Europe compared to ERA-20C. These storms additionally intensify around the British Isles, near the Alps, and further towards Scandinavia, a signal present in both MPI-ESM-LR (Fig 18b) and ERA-20C (Fig 18d).

To corroborate the qualitative interpretations of previous sections, we turn our attention to Table 4, which computes statistics of cyclogenesis or intensification in different regions for European storms in particular. The proportion of high footprint storms which generate in RW is increased compared to all storms or low footprint storms. The same can be said for storms intensifying in RE. This indicates that high footprint storms are more likely to generate in RW and/or intensify in RE, particularly on the Southwestern flank of the British

41
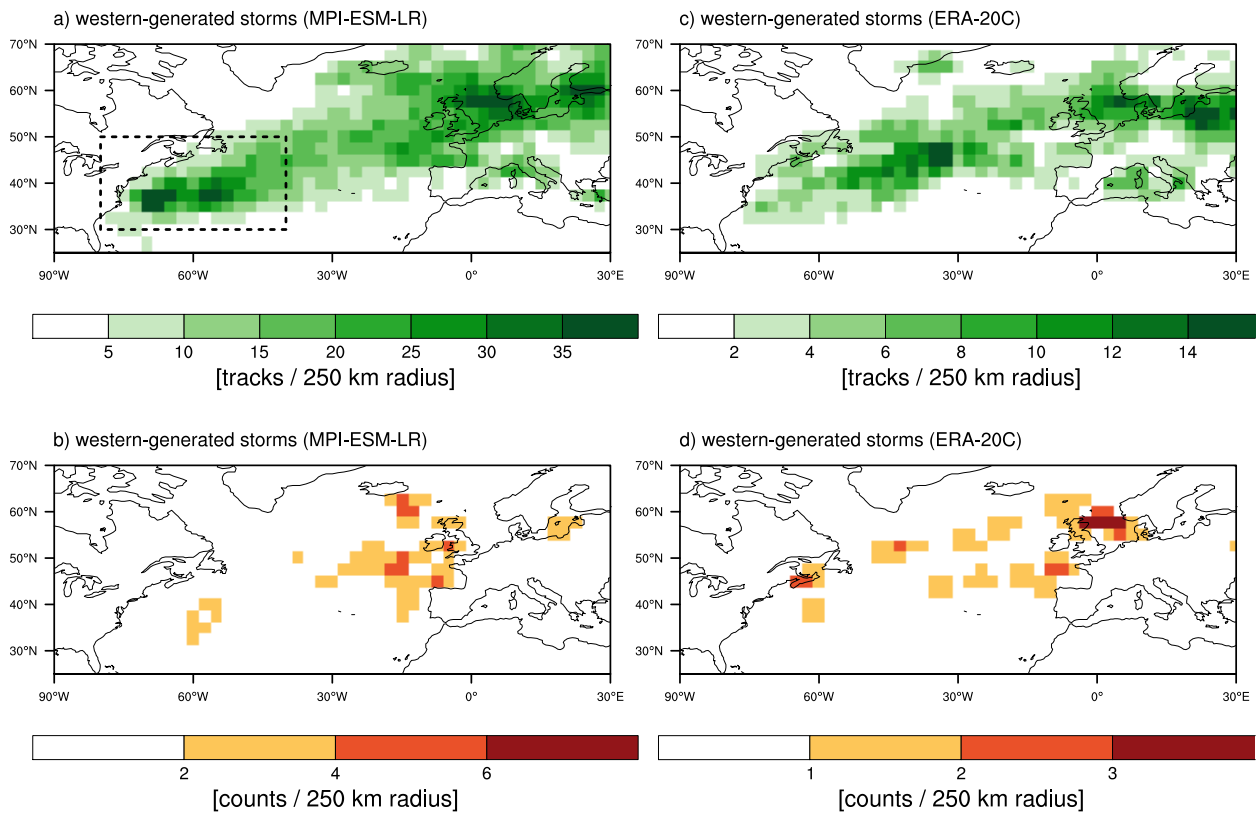
Figure 17: Cyclone track densities and maximum intensification densities for MPI-ESM-LR (a,b respectively) and ERA-20C (c,d), filtered by cyclones which generate in RW (dashed box in a) and create high footprints in Europe.
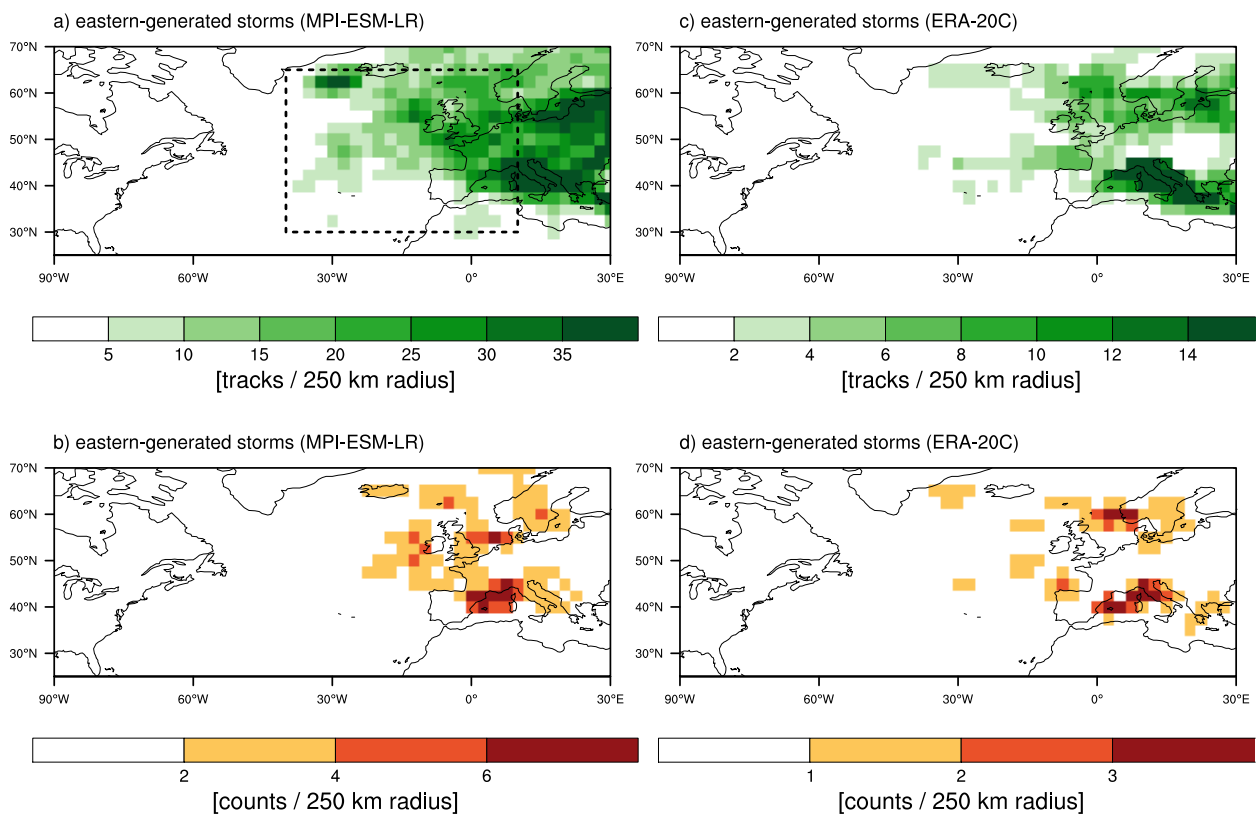
Figure 18: As Fig. 17, but for high European footprint storms which generate in RE (represented by the dashed black box in a).

Isles.

Comparison with North Atlantic storms

To identify whether these cyclogenesis and intensification patterns are unique to high and low European footprint storms, we compare them to the behaviour of North Atlantic systems.

Data set	MPI-ESM-LR			ERA-20C		
Region	High SSI_{EU} (259)	Low SSI_{EU} (259)	All (5164)	High SSI_{EU} (78)	Low SSI_{EU} (78)	All (1550)
RW - Gen	32	10	18	26	15	19
RW - MI	6	5	5	5	1	5
RE - Gen	39	55	50	37	38	42
RE - MI	60	49	49	47	42	45

Table 4: Proportion of storms (in %) generating or intensifying in RW or RE, relative to the storm set in the respective column (storm set size in brackets). The remainder of storms did not generate or intensify in either RW or RE.

Figures 19 and 20 shows cyclogenesis and intensification density patterns for North Atlantic windstorms, respectively. Here, footprints are defined by storms which exist in the North Atlantic region, which itself is defined by the boundaries 80W — 30E, 30 — 65N. We see that high footprint storms are generated far upstream towards Florida, whereas weaker storms can generate here as well, but are more dispersed across the North Atlantic. In ERA-20C, a higher density of cyclone generation can be seen towards Greenland as well. Shifting our attention to intensification densities, both MPI-ESM-LR and ERA-20C show that high footprint storms typically intensify around the US east coast or Greenland, and some intensify further South or East in the Atlantic Ocean. In fact, many low footprint storms additionally intensify in similar regions; compared to high footprint storms however, their signal is reduced around the US east coast. These findings are similar to cyclogenesis and intensifications of cyclones studied by Reale et al. (2019).
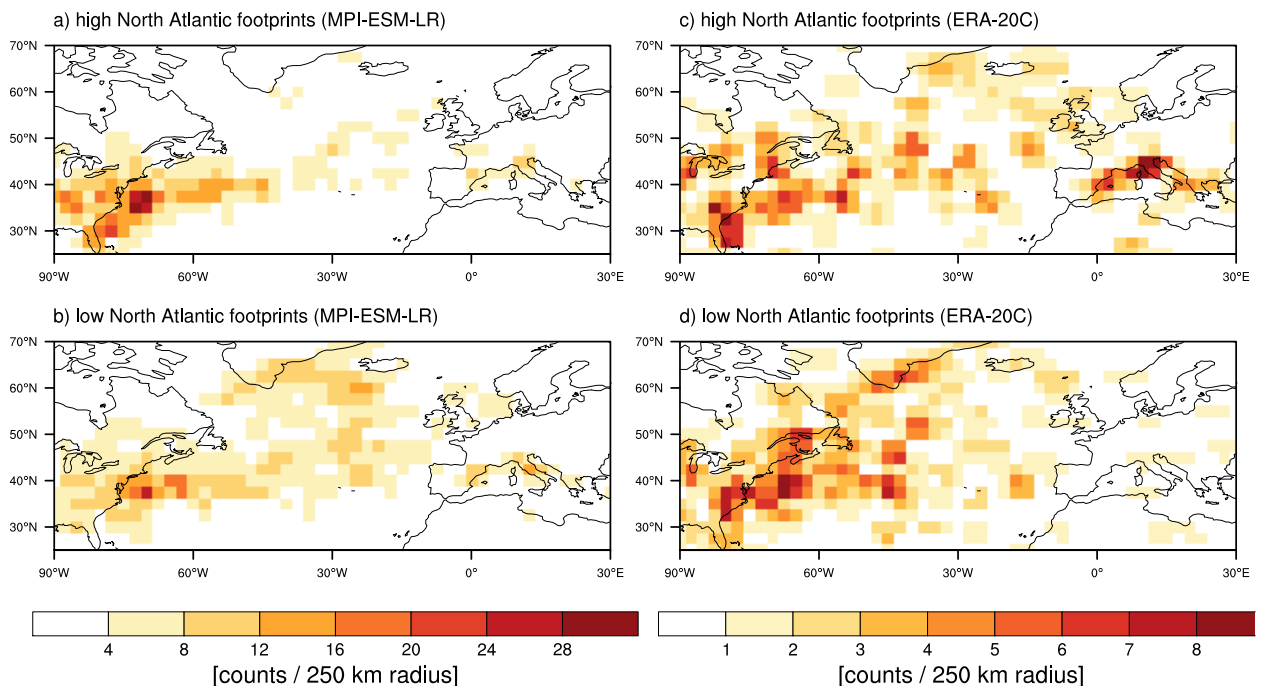
Figure 19: As Figure 15, but for storms within the North Atlantic region.

Thus, anomalously strong European storms are a subset of strong North Atlantic cyclones which form upstream over the North Atlantic Ocean, but instead of intensifying near the US East Coast or Greenland, they are deflected slightly towards Europe.

2.8   Summary of primary relationships

This Chapter aimed to address the question: "to what extent is the footprint of a windstorm attributable to properties of its parent cyclone?". General statistical relationships between
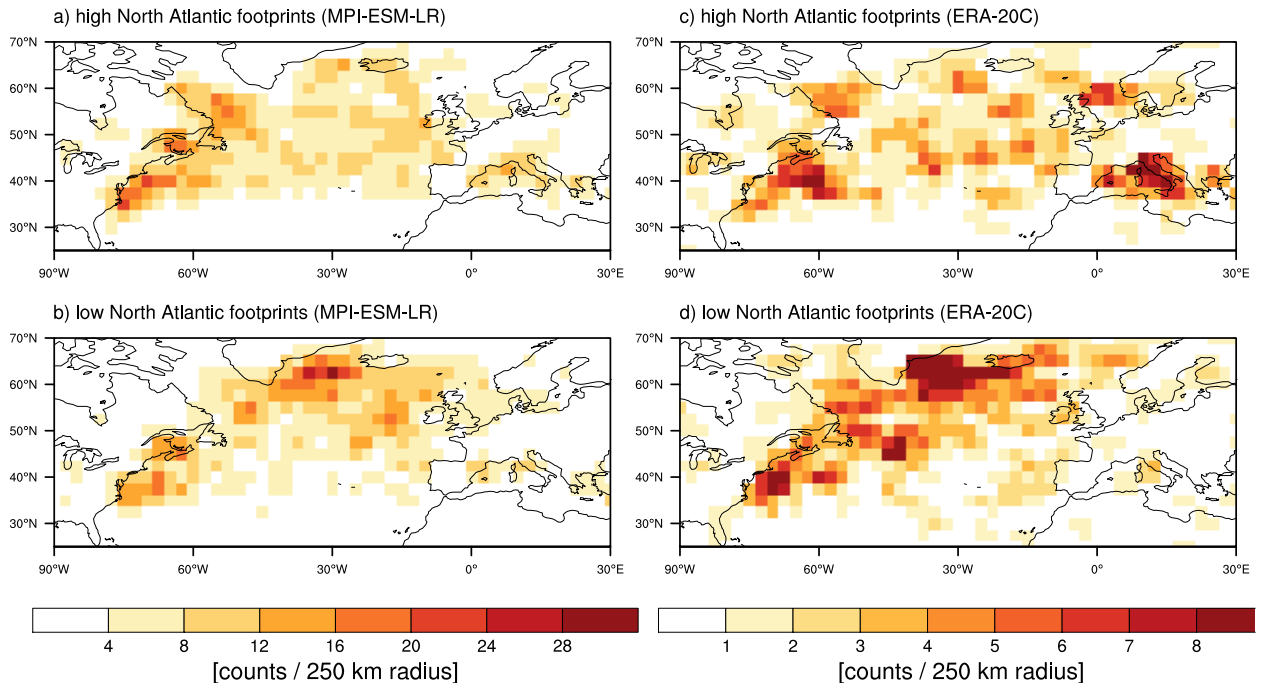
Figure 20: As Figure 16, but for storms within the North Atlantic region.

properties of windstorms and cyclones have been established. We began by first looking at storm behaviour from an interannual perspective, to compare the winter-aggregated storm footprints (or "storminess") with the commonly used winter storm counts. We found that, while storminess correlates well with storm counts, years with high or low storminess were not necessarily conducive with a high or low number of windstorms. For example, stormy years could include an average number of storms, but individually powerful events were still present. An investigation of trends also showed that ERA-20C sees a positive trend in counts and storminess, but none for the MPI-ESM-LR data. With regards to previous works, Trigo (2006) show that the trends of cyclone counts actually differs between Northern and Central Europe, and that Central Europe actually shows a downward trend in storm counts; these results were consistent in two other reanalyses (NCEP/NCAR and ERA-40). They suggest this is related to a northward shift of the storm tracks (also found by Wang et al. (2006)) and by fluctuations in the NAO. Therefore, a closer investigation of regional dependencies could be investigated in future studies.

The windstorm footprint itself is primarily related to the area and lifetime of the windstorm. It is not explicable by any single cyclone property. However, there are significant and strong correlations between the surface wind cluster field and the core pressure and maximum intensity of the cyclone. Although the footprint depends strongly on the windstorm's lifetime, long lifetime cyclones are not necessarily conducive with high footprints. This is primarily to do with the timing in which a cyclone intensifies: a European footprint is expected to be high given that the cyclone intensifies near Europe and not too far upstream or downstream.

Following from this, the growth behaviours between windstorms and their parent cyclones are established. This is necessary given that windstorms are by nature a statistical phenomenon based on percentiles, while cyclones are based on full MSLP/vorticity fields and grow in a more continuous manner. It is found that windstorms generally experience their maximum intensification and maximum intensity in a 24 hour window of their parent cyclone. Moreover, it takes two days for the windstorm to spawn following cyclogenesis, so long that its parent cyclone reaches a WGT of around 1.0 hPa deg. lat.$^{-2}$.

Last, cyclone pathways relating to high and low footprint storms are examined. In general, high footprint storms are associated with cyclogenesis around the Western North Atlantic, particularly around the US East Coast and the Gulf Stream region. Maximum intensification densities are additionally studied. It is found that, regardless of the windstorm footprint magnitude, the majority of storms intensify near the British Isles or Spain. Higher footprint windstorms are more likely to intensify when they are positioned further South towards Central Europe, such that they are more likely to persist in the European region when they enter. This is compared to the behaviour of all North Atlantic storms, which exhibit cyclogenesis and intensification maxima further upstream in comparison (around the US East Coast and Greenland, respectively). Thus, most high footprint European systems are a less common subset of these North Atlantic systems which generate in the West, but do not propagate towards Greenland, instead traveling East to Europe. Moreover, a number of Mediterranean signals can be identified. A large portion of windstorms generate, travel, and intensify within the Mediterranean region alone, and it is possible a number of systems form upstream and drift into the Mediterranean before they intensify. However, these Mediterranean signals differ between the MPI-ESM-LR and ERA-20C data sets, in the sense that the latter detects them with potentially higher European footprints.

Assimilating these ideas together, we find that a high footprint windstorm depends on their parent cyclones in the following ways. These cyclones are more likely to generate over the US East Coast, where they intensify near Europe, ideally positioned near the British Isles or Spain. As the cyclone enters Europe, the footprint of its daughter windstorm storm depends, to some degree, on the magnitude of the cyclone's intensification phase. From there we can expect the windstorm to intensify in a 24 hour window of this phase. The windstorm decays shortly afterward and its cyclone some time later. Another variation of this process is a storm which generates further East (either over the open ocean or near Greenland), but will additionally intensify along the western flank of Europe. In future work, it would be fruitful to systematically classify the many pathways that these high footprint systems can take. This would simplify the process of assigning different environmental factors that contribute to the system's European footprint.

3 Cyclonic growth factors and European windstorm footprints

> Unlike history, meteorology does repeat itself.
>
> *Mel Goldstein*

We have seen that high footprint windstorms are associated with specific properties of cyclones, namely cyclones which experience higher growth rates and reach deeper core pressures. These same cyclones are more likely to generate in the West Atlantic, followed by a maximum intensification phase in the East Atlantic. As explained in Section 1.6, once we understand how cyclones affect the behaviour of windstorms, we can now establish relationships between environmental factors (which affect those same cyclones) and windstorms. The evolution of a cyclone can be thought of in terms of factors affecting baroclinic wave development and baroclinic instability, a process whereby phase-locked circulation anomalies at the surface and tropopause mutually amplify each other to create powerful cyclones at the surface. Here, we categorize these factors into three broad types.

1. Lower-level thermal gradients, which contribute significantly to thermal advection near the surface. This, in turn, leads to the development of thermal (and hence pressure) waves near the surface, an ingredient essential for baroclinic instability.

2. Upper-level development, related to upper-level (i.e. tropopause) troughs and jet streams. The existence of an upper-level trough is indicative of divergence, which itself can deepen surface lows directly beneath. Moreover, these regions can be associated with extremely high upper-level winds, i.e. jet streams.

3. Moisture and its contribution to diabatic heat release. Especially in lower layers, the cooling of moist air causes it to release latent heat via condensation, in turn creating positive circulation anomalies and vertical motion of air.

We collectively call these effects Cyclonic Growth Factors (CGFs), and they will be defined and explored in the following sections. The goal is to understand whether the magnitude of a storm's European footprint is in some way attributable to the strength of these CGFs, particularly during the genesis or intensification phase of cyclones.

3.1 Cyclonic growth factors

The following cyclonic growth factors constitute a set of environmental variables which are likely to affect either the genesis or intensification of a cyclone.

Eady Growth Rates

Eady Growth Rates (EGRs) represent the maximum growth rate of unstable baroclinic modes, and are frequently used as a measure of baroclinicity in the atmosphere. They are defined as:

$$EGR = 0.31 f |\partial \mathbf{v}/\partial z| N^{-1}, \qquad (2)$$

where f is the Coriolis parameter, $|\partial \mathbf{v}/\partial z|$ is the vertical wind shear, and N is the Brunt-Vaisala frequency, which is a measure of static stability in the chosen layer. We calculate EGRs in both the 850 - 500 hPa and 500 - 250 hPa levels. The seminal work produced by Hoskins and Valdes (1990) utilized EGRs to study and describe the existence of extra-tropical storm tracks. To this day, they are frequently used as diagnostics for North Atlantic extra-tropical storm development (e.g. Willison et al. (2015), Shaw et al. (2016), Novak et al. (2018)). EGRs have high-frequency variability: their anomalies are replenished by temperature gradients and destroyed by eddies, thus a 3-day running mean filter is applied. Previous studies have found robust relationships between the magnitude of lower- and upper-level EGRs and the intensity or frequency of cyclones and windstorms (e.g. Ulbrich et al. (2001), Pinto et al. (2009), Renggli (2011), Nissen et al. (2014)).

The Jet Stream

The jet stream is a known source of cyclone development. We calculate the jet stream as the total wind at 250 hPa. Here, it is used both as a proxy for upper-level forcings and to an extent a representation of vertical wind shear in the layer. The region of a jet's left exit at upper levels is known to be a region of divergence which can assist in cyclone intensification in the layer below; this interaction has been studied in great detail in a number of studies (e.g. Ulbrich et al. (2001), Pirret et al. (2017), Priestley et al. (2017)). Figure 21 illustrates a jet streak and its associated patterns of convergence and divergence.
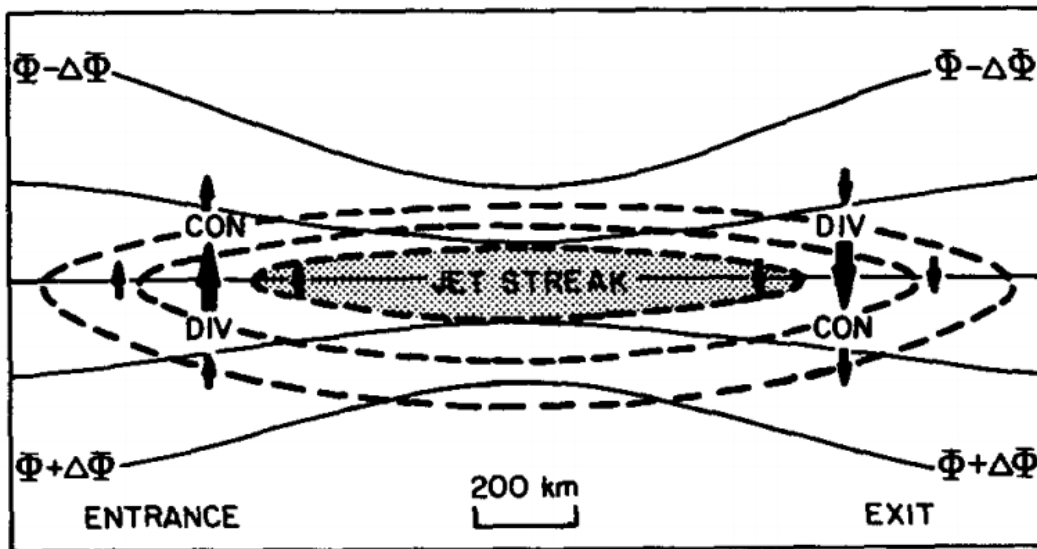
Figure 21: Schematic of patterns of convergence (CON) and divergence (DIV) associated with a jet streak. Solid lines represent geopotential height on a constant surface, Φ, and dashed lines are isotachs with the maximum wind speed shaded. Solid arrows represent ageostrophic motions. Adapted from Keyser and Shapiro (1986).

Potential vorticity

Potential vorticity (PV) in the Ertel framework describes the ratio of the absolute vorticity of an air parcel to the depth of the vortex, or the distance between two surfaces of constant potential temperature θ, and is conserved following the motion in adiabatic and frictionless flow. It is written as:

$$PV = \frac{\zeta_a \cdot \nabla \theta}{\rho}, \tag{3}$$

where ζ_a is the parcel's absolute vorticity, $\nabla \theta$ is the vertical gradient of potential temperature θ between two isentropes' surfaces, and ρ is the density of the air. Thus, an increase in the absolute vorticity of the parcel should be accompanied by a "stretching" of the vortex between these two isentropes, i.e. a reduction in $\nabla \theta$. It can be shown that the Lagrangian rate of change of PV is related to a diabatic heating rate $\dot{\theta}$ and frictional acceleration $\dot{\mathbf{u}}$ as

$$\frac{D}{Dt} PV = \frac{1}{\rho} \zeta_a \cdot \nabla \dot{\theta} + \frac{1}{\rho} (\nabla \times \dot{\mathbf{u}}) \cdot \nabla \theta. \tag{4}$$

This implies a positive anomaly in PV can be generated by diabatic changes represented by the first term of equation above. Figure 22 illustrates the response of the atmosphere to a diabatic heating region in terms of PV anomalies. The instantaneous response of the atmosphere is to form an ageostrophic circulation which acts to oppose the heating, i.e. air cools by rising adiabatically. This results in convergence below (positive cyclonic tendency) and divergence aloft (negative cyclone tendency). The instantaneous response can act to reinforce surface cyclonic tendencies with the lower-level positive PV anomaly. Davis and Emanuel (1991) used PV diagnostics for a cyclone case study to demonstrate that lower-level PV anomalies were responsible for around 40 % of the cyclone's circulation. For the steady-state response of the system, the positive PV air has been ageostrophically lifted and coincides with the region of diabatic heating, while the negative anomaly disperses aloft in a lens shape.
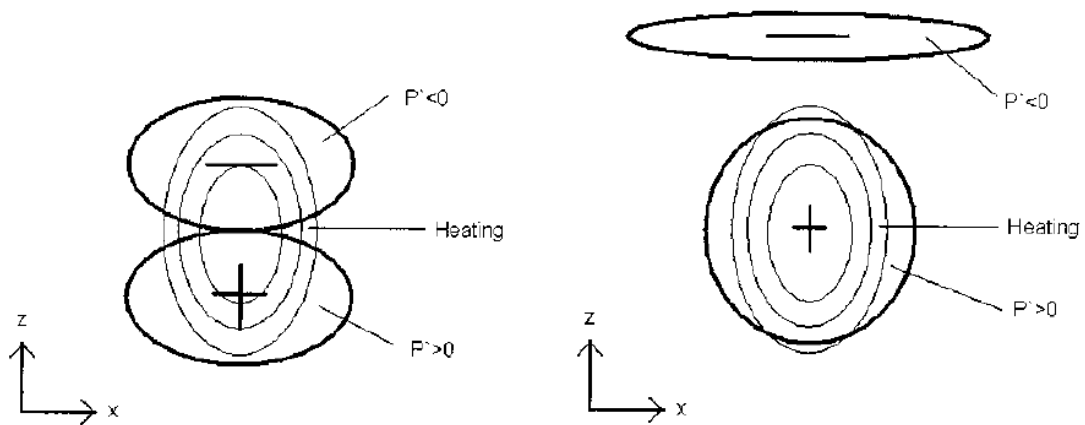
Figure 22: Instantaneous (left) and steady-state (right) heating source and its PV anomaly (P') responses, where z and x refer to the vertical and zonal coordinates, respectively. Adapted from Pomroy and Thorpe (2000).

The studies of Ahmadi-Givi et al. (2004), Čampa and Wernli (2012), and Davis and Emanuel (1991) found that PV at the 850 hPa level (PV850) is indicative of high latent heat release, following warm, moist air flowing through a warm conveyor built and being transported upwards through the cyclone. The advantage of using PV850 over the commonly-used equivalent potential temperature is that it is a direct indicator of moisture conversion to latent heat release in the cyclone, whereas the latter quantity incorporates relative humidity but does not indicate any of the conversion to energy. We compute PV850 using 6-hourly wind, temperature, and pressure fields.

Land-sea contrasts

One of the key features of the North Atlantic storm track is that a number of mechanisms assist in restoring baroclinicity in the West Atlantic (e.g. Ambaum and Novak (2014)). Since vigorous eddy activity tends to mix surface temperature gradients such that it reduces baroclinicity, restoration mechanisms are particularly important. One such mechanism relates to land-sea contrasts (LSCs), or regions of highly-concentrated surface thermal gradients along coastlines due to the significantly different heat capacities of land and ocean. These gradients effectively act as a secondary forcing.

However, the nature of land-sea contrasts as a spatiotemporal field is such that they are confined to coastal regions. In fact, there is no canonical definition of a land-sea contrast field, and given its geographical constraints it is naturally a challenging task to construct such a field. Nonetheless, we produce a land-sea contrast by adapting the method of Day and Hodges (2018), who calculated the magnitude of the 2-meter Temperature gradient, $|\nabla T_{2m}|$. Here, we do the same, but we compute the gradient in both the zonal and meridional directions, taking into account a $\cos\phi$ weighting of the zonal segments, and the gradient itself is computed using a centered finite differencing. Mathematically this is

$$|\nabla T_{2m}| = \sqrt{\nabla T_{2m,x}^2 + \nabla T_{2m,y}^2}, \tag{5}$$

where x and y are the zonal and meridional components of the field, respectively. It should be noted that the magnitude of both components is comparable around the regions of interest that we will study later.

This is followed by a 500 km radius smoothing of the field. This radius was chosen to find LSC anomalies on scales approaching the synoptic scales instead of grid-point-wise scales. Finally, a 3-day running mean is applied to the field, as the gradients can fluctuate regularly. With the field prepared, this is where a partially subjective interpretation of the field is required. When we seek land-sea contrast signals, we look only around coastal regions, and not too far inland or out into the ocean. Moreover, because it is smoothed in a 500 km radius, we still identify signals within a few 100 km of the coastlines. Thus we acknowledge that while LSC signals do not provide absolute precision in the location of temperature gradient anomalies along the coast. However, by eye, it was found that the smoothing procedure faithfully captures the key locations of strong anomalies along the coast.

SST gradients

Similar to land-sea contrasts, SST gradients (SSTGs) are essential in restoring baroclinicity in the West of North Atlantic, particularly around the Gulf Stream. This region is characterised by strong Western Boundary Currents (WBCs), which vigorously transport warmer waters from the South such that it tightens surface temperature gradients. Several studies have shown that SST gradients associated with the Gulf Stream assist in forcing the atmosphere. Minobe et al. (2008) found that these gradients induce convergence bands at the surface, extending all the way through the troposphere and producing diabatic heat release. Both Booth et al. (2012) and Vries et al. (2019) demonstrated that SST gradients around the Gulf Stream alter latent heat fluxes, which in turn modify the planetary boundary layer and associated lower-level surface winds in developing storms. Despite the fact SST gradients

are a secondary forcing (i.e. their structure imprints on the atmosphere first through surface heat fluxes, which then go on to force baroclinic waves), it is still of great interest to identify systematic relationships between them and North Atlantic storm activity to improve the accuracy of numerical weather prediction.

These gradients are additionally computed using centered finite differencing on daily SSTs, and again, both the zonal and meridional components are individually studied. The same 500 km radius weighted smoothing is applied, but no temporal smoothing is necessary, as SSTs have relatively low daily variability.

3.2 Methods

This section focuses on compositing to identify changes in the magnitudes of environmental variables with respect to the extremes of storm footprints. The type of compositing is either fixed-frame or Lagrangian, depending on the variable.

Fixed-frame compositing

This compositing is applied to LSCs and SSTGs. The former as it is constrained specifically to coastlines, the latter because oceanic fields cannot be used reliably for Lagrangian compositing (due to the inclusion of numerous missing values associated with land). For a given set of storms, assign a reference point $r(p_s, t_s)$ of each storm as either the cyclone generation or maximum intensification, where p_s is its geographical position with longitude and latitude (λ_s, ϕ_s) and t_s the point in time. If p_s existed in the region of interest, take a slice of that field at time $t = t_s$. This is repeated for all storms in the data set and averaged to give one composite for a storm set. For this section, two composites are created: one for high footprint and one for weak footprint storms. Finally, a difference between the composites is calculated. At each grid point, a significance test using a Welch two sample t-test is conducted. This is used to test the null hypothesis that the two populations have equal means, and is a more reliable version of Student's t-test for unequal variances or sample sizes, as is the case for here. In Section 3.7 we will demonstrate that both these quantities need only be studied in the Western Atlantic.

Lagrangian-frame compositing

For the atmospheric variables EGR, Jet, and PV850, we can identify their anomalous fields in the vicinity of the storm instead, increasing our ability to assess the local dynamics of the cyclone. Lagrangian compositing has previously been used to assess the occurrence of extreme CGF values in the vicinity of a cyclone (Pinto et al., 2009), the cyclone radius (Rudeva and Gulev, 2007), and the sensitivity of its growth to different variables (Dacre and Gray, 2013).

The procedure centers fields on the cyclone center, but because the size of the cyclone-centered frame has a latitude dependency, a rotation of the grid must be performed to capture an equivalent projection on any cyclone. Mathematically, we wish to rotate the point of $(\lambda = 0, \phi = 0)$ onto the cyclone center. This can be achieved by rotating the pole to a longitude $\lambda = 180 - \lambda_s$ and a latitude $\phi = 90 - \phi_s$. The new values of this rotated grid are estimated using bilinear interpolation. Then, a $20° \times 20°$ region is taken around the cyclone

	Model			Reanalysis		
Region	High SSIEU (172)	Low SSIEU (172)	All (3427)	High SSIEU (49)	Low SSIEU (49)	All (966)
RW - Gen	40	15	27	43	16	30
RW - MI	9	8	8	8	2	7
RE - Gen	31	60	47	27	39	40
RE - MI	66	61	60	63	47	56

Table 5: Proportion of storms (in %) generating or intensifying in RW or RE, relative to the storm set in the respective column (storm set size in brackets).

center, which equates to 2000 km ×2000 km. This rotation procedure is additionally applied to the 95th percentile field. Similar to fixed-frame compositing, we take the field at time $t = t_s$, but we further divide it by the 95th percentile field to obtain anomalies (the method is not sensitive to the choice of percentile). This is repeated for one set of strong footprint storms and weak footprint storms to produce two composites. Finally, their difference is computed, and a Welch two sample t-test is conducted for significance testing.

3.3   Storm behaviour

The statistics discussed in section 4 demonstrated that for both MPI-ESM-LR and ERA-20C, a large number of storms will generate or intensify around the Alps. Although the cyclone tracking scheme disallows the localisation of lows above an elevation of 1500 meters, it is still possible for orographically-developed lows to form here due to the interpolation of a coarse-gridded orography, which can underestimate the true elevation of the Alpine region. While orography likely plays an important role in the development of some severe European winter windstorms, this process is beyond the scope of this study. This necessitates the removal of storms localised in the Mediterranean region. The Mediterranean region is bound by regions east of 0° E and south of 48° N, i.e. near the Alps and further east. From the original storm set in Section 2.8, any storm which generates and/or intensifies in the Mediterranean is discarded. After filtering in this way, we retain 3427 and 966 storms for the MPI-ESM-LR and ERA-20C data sets, respectively. This is a 33% and 38% reduction in storms, respectively. With the removal of Mediterranean systems from the original storm data, we first calculate statistics of storm sets as shown in Table 5.

For high footprint storms, 40% / 43% of them generate in the Western Region (abbreviated as RW, regions defined by Figure 15), a large increase over the proportions of 15% / 16% and 27% / 30% for low footprint or all European storms, respectively. For any storm set in either data set, less than 10% intensify in RW. In both MPI-ESM-LR and ERA-20C, a similar number of high footprint storms generate ($\sim 30\%$) or intensify in the Eastern Region ($\sim 65\%$, abbreviated as RE with boundaries defined in Figure 16). However, the two data sets disagree on the genesis and intensification locations of low footprint storms. Collectively, around 70% of low footprint storms in the MPI-ESM-LR data generate or intensify in either of the two regions — in comparison, around 50% of them for ERA-20C. Thus, after removing Mediterranean systems, we observe similar relationships established in Section 2.8: compared to low footprint storms, high footprint storms prefer to generate in RW and intensify in RE, and all storms in general tend to intensify in RE (i.e. close to Europe). These results are consistent with what we found in Table 4 as well. In general,

removing Mediterranean systems shifts the quantiles of footprints positively, and strengthens the signals of storms forming and intensifying over the North Atlantic Ocean.

3.4   Baroclinic signals at cyclogenesis

We examine changes in CGFs at the temporal point of cyclogenesis for cyclones generating in both RW and RE here. Note that at the genesis phase of the cyclone, for any data set in either RW or RE, a very small difference for PV850 anomalies between high and low footprint storms was found and it is thus not shown.[2] To begin with, we look at the genesis point of cyclones which experience cyclogenesis in RW. Changes in EGR at 850-500 hPa and the jet at 250 hPa with respect to the footprint of a European windstorm can be seen in Figure 23. All signals are similar for EGRs in the 500-250 hPa layer but are not shown here. The EGR changes differ between MPI-ESM-LR and ERA-20C. In the former, significant increases in EGR anomalies of up to 40% are visible directly around the cyclone core. In the latter, however, there are significant increases in anomalies of up to 50% displaced further away from the cyclone center. Moreover, there are three maxima situated ∼1000 km East, 1000 km North, and ∼ 2000 km Southeast, of which the latter two are statistically significant. The anomalies in both data sets are approximately elliptical in their shape, with its major axis in the zonal direction. Thus, although there is uncertainty in the anomalies' exact location and hence direct influence on the cyclone, their magnitude and geometry are consistent between both data sets. Composite differences in the jet stream at 250 hPa are very similar to those of the EGRs, a somewhat expected result. Equation 2 shows that EGRs have a strong dependency on the vertical wind shear as well as static stability. Additionally, strong upper-level jet streams are associated with a higher vertical wind shear in the layer below. Thus, despite the dependency of EGRs on static stability, the two structures tend to reflect each other here.

If we instead look at the change in these anomalies at the genesis phase of cyclones in RE (Figure 24), a similar signal to genesis in RW is apparent. In MPI-ESM-LR, anomalies significantly increase by up to 30% with respect to the windstorm footprint in zonally-extended bands. For ERA-20C, the significant increases of up to 50% are once again displaced further away from the cyclone center, and the significance contour is small. Moreover, there is less agreement between EGRs and the jet: significant jet signals are positioned southeast of the cyclone center, whereas EGRs are directly west and east.

An advantage that comes with compositing spatial jet fields is that the position of the jet relative to the center of the cyclone can be identified. Figures 23 and 24 show that, for both data sets, the jet stream signals are positioned Northwest (all signals, RW) or Southeast (ERA-20C signals, RE) relative to the center of the cyclone. Ideal jet positions for cyclone intensification are either its right entrance or its left exit. These particular signals currently show no preference towards either positioning, but we will see later how this becomes relevant.

The interpretation of these signals at the genesis phase in RW is complex, primarily because we wish to link upstream dynamics to the strength of windstorms much further downstream. It is first important to note that in both data sets, the signals are non-significant

---

[2]This result is expected: a PV850 anomaly is generally a secondary feature (e.g. Wernli et al. (2002)). The cyclone needs to reach a mature enough phase such that a frontal system can develop. This, in turn, assists in the horizontal and vertical transport of moist air, which then releases latent heat by condensation.
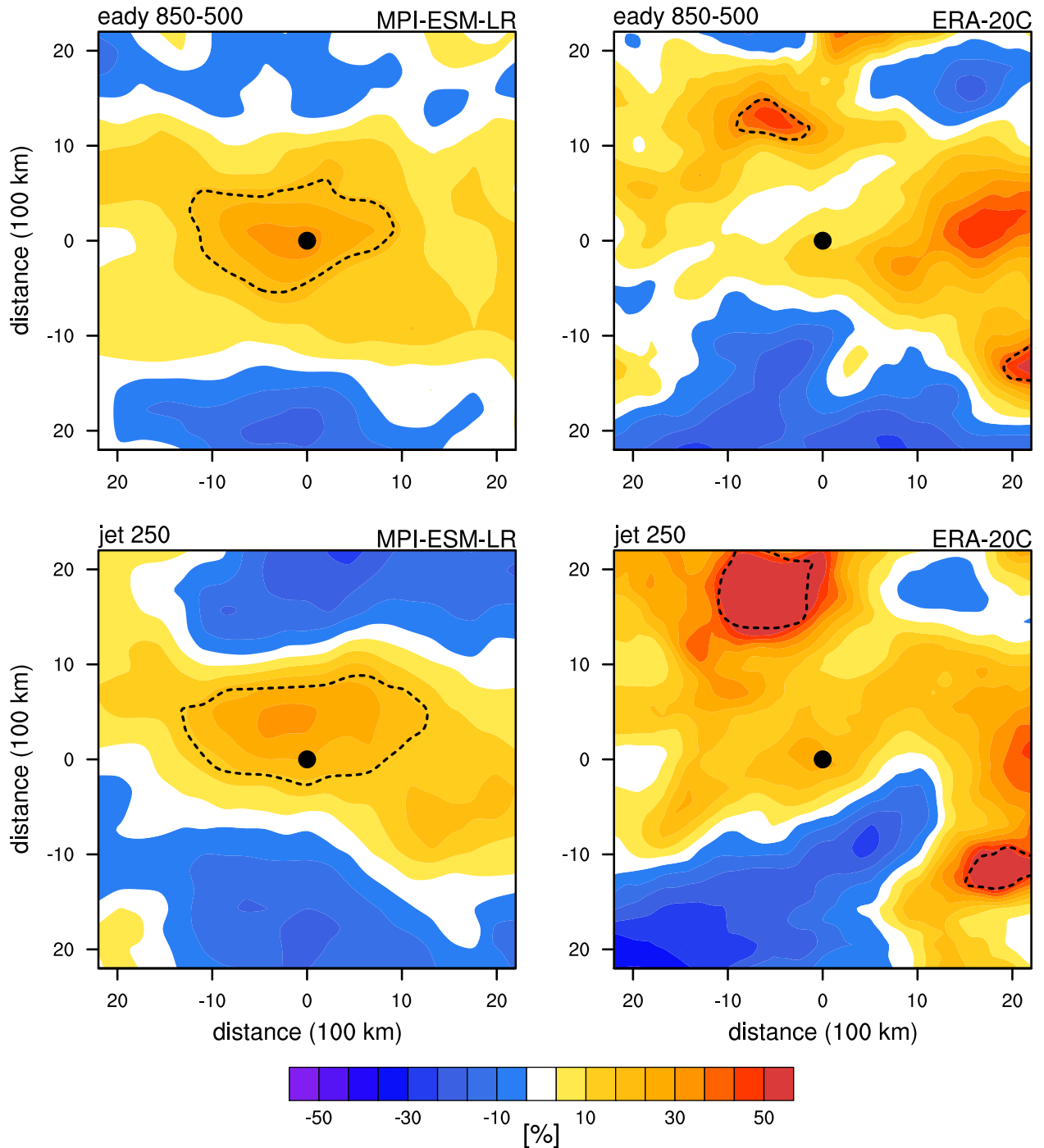
Figure 23: Percentage changes (%) in EGRs at 850-500 hPa (top, "eady 850-500") and the jet stream at 250 hPa (bottom, "jet 250") anomalies between high and low European footprint storm systems, for both MPI-ESM-LR (left) and ERA-20C (right) data. The abscissa and ordinate are the distances from the cyclone center (black dot), and changes significant to $p < 0.05$ (using a Welch two-sided t-test) are enclosed by the dashed contour. These cyclones necessarily generated in RW, and the composites are centered on the point in time and space of cyclogenesis.

and/or far displaced from the cyclone core, i.e. the relationship between storm footprints and these quantities at cyclogenesis is fairly weak. Nevertheless, a non-negligible increase is found, and we wish to understand how stronger EGRs and jet streams are conducive with higher intensity cyclones and European footprints.

To begin with, we should consider how cyclone intensities and their windstorm SSIs differ between high and low European footprint systems. For cyclones generating in RW, an analysis of the cyclone lifetime-averaged intensity showed that, compared to high footprints, cyclones with low footprints were not necessarily weaker cyclones overall (in terms of $\nabla^2 p$). However, the SSI of low footprint storms was on average around 100 times weaker compared
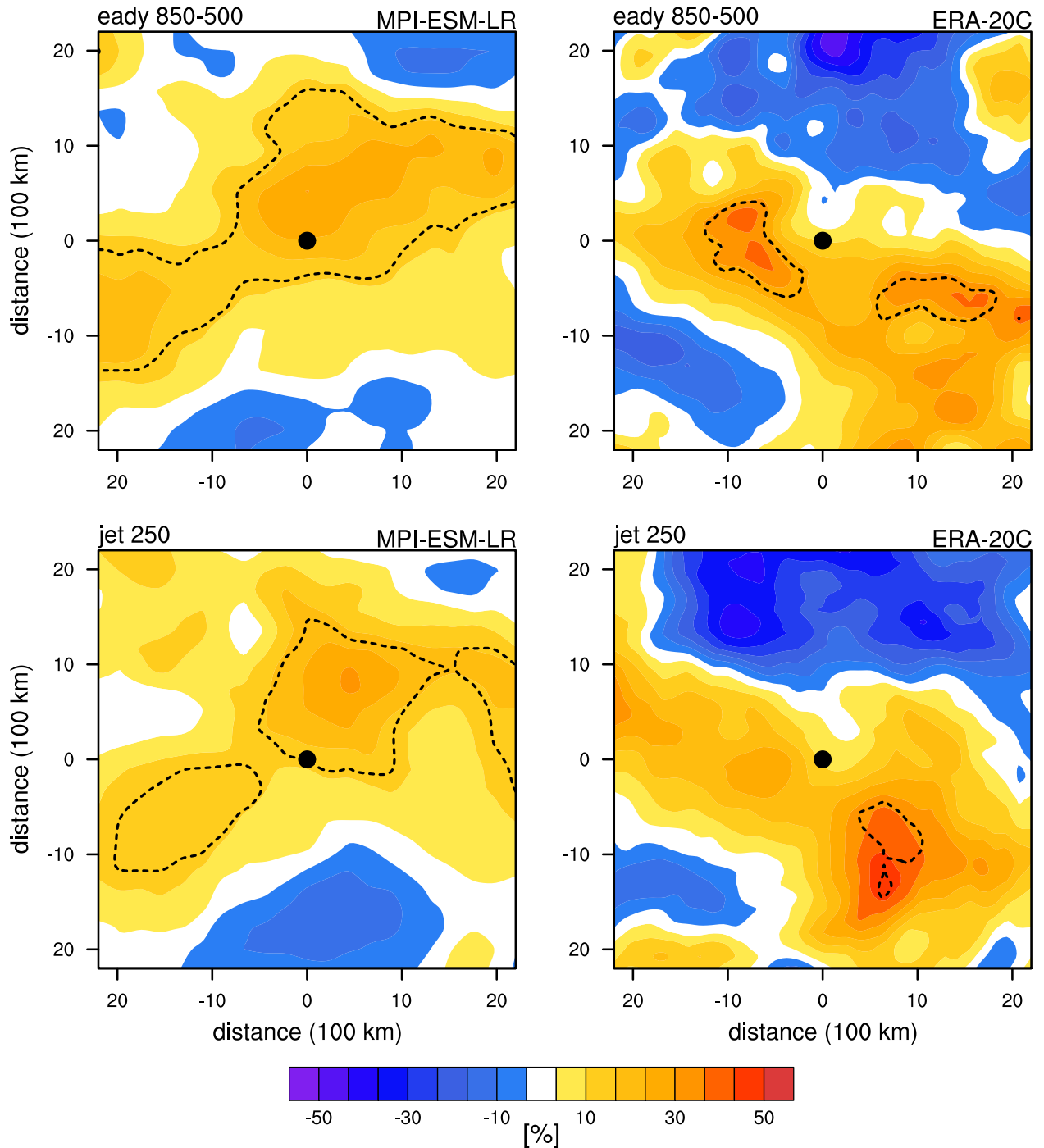
Figure 24: As Figure 23, but for cyclones which necessarily generated in RE.

to high footprint storms. This stark magnitude difference in SSIs between high and low footprint storms can be attributed to the mean windstorm area, where high footprint storms had significantly greater mean areas around six times larger compared to low footprint storms. Some studies found that cyclones which generate in RW have higher mean radii (Rudeva and Gulev, 2007), which themselves have longer lifetimes and deeper core pressures (Raible et al., 2018). It is thus hypothesized that the size of the cyclone may affect the total area of the windstorm (and hence its potential footprint in Europe) due to its longer development time, and that a strong initial baroclinic environment in the West is conducive with larger cyclones. This warrants further investigation of the relationship between the evolution of cyclone radii and its daughter windstorm's area. We will explore later how these quantities could be generated or coupled to surface thermal gradients, which are energetic around RW.

For systems generating in RE, we see signals that are not too far displaced from Europe. The same concept above further applies here: the higher baroclinicity can still produce higher radii systems, albeit systems with reduced development over the North Atlantic

Ocean. These signals are too far displaced from the US East Coast to be associated with any surface thermal gradients (as we will see later), and are simply generated by nearby jet streams or baroclinicity. There is the additional question of whether these systems are instead associated with secondary cyclogenesis, whereby East Atlantic cyclones form via frontal waves of primary cyclone systems which developed upstream (Rivals et al., 1998; Dacre and Gray, 2009); this was a prominent feature of Kyrill (Ludwig et al., 2015). This means East Atlantic systems may have generated from effects unrelated to mid-tropospheric baroclinicity accounting for the weaker signals in Figure 24 compared to Figure 23. However, this is beyond the scope of this study, as it necessitates the use of a regional-scale model to resolve frontal systems appropriately.

3.5 Baroclinic signals at cyclone maximum growth

Here, we turn our attention to the difference composites at the temporal point of the maximum intensification phase of cyclones. An extremely small number of storms intensify in RW, and are therefore excluded from this analysis (we saw in previous sections that storms which intensify in RW are highly unlikely to imprint a significant footprint downstream in Europe). Thus, we look at storms whose cyclones experience maximum intensification in RE in Figure 25. Beginning with EGRs, we see a large zonally-extended area of significant increases in MPI-ESM-LR, with the strongest increases of 50% within a ∼1000 km radius of the cyclone center. The ERA-20C increases, by comparison, are additionally significant and strong within a similar radius, but the significance contour is not as zonally extended and more confined. Nonetheless, compared to the cyclogenesis composite results in Figures 23 and 24, the two data sets agree more strongly. Similar signals can be found for the jet stream. Increases of up to 50% for MPI-ESM-LR, and well over 60% for ERA-20C, are located around the cyclone core within a longitudinal band. This band has longitudinal and latitudinal ranges of about 40° × 20°. Additionally, these increases are significantly higher compared to cyclogenesis composites. As before, these jet signals have a similar structure to the EGR signals. Moreover, the significance contours enclose similar regions in both variables, whereas the cyclogenesis composites instead found disagreements in ERA-20C data. The center of the cyclones is such that they are relatively close to the jet exit, but the contribution of this effect to the storm footprint will be explored in more detail in Section 4. Altogether, the results are consistent with the findings of Pinto et al. (2009), who located zonally-extended EGR and jet anomalies surrounding extreme cyclones during their intensification phases as well.

The EGR and jet composites at the intensification phases of cyclones in different regions elucidate the role of baroclinicity or upper-level forcings on the development of cyclones with high European footprints. Evidently, higher baroclinicity is associated with more intense storms, but the baroclinic environment is directly related to local upper-level jet anomalies via strong wind shear in the troposphere. More specifically, these anomalies should be situated towards the East Atlantic, and their positioning with respect to the position of the cyclone is crucial in their development. The passage of cyclones through their right entrance or left exit will help intensify them through upper-level divergence. In fact, specific jet positions are associated with the suppression of some cyclones, such as Lothar (Ulbrich et al.,

2001) — this is primarily related to coincidence of the upper- and lower-level trough axes (instead of the backwards tilt with height that is typically required for baroclinic instability). Thus, we require jets which are a) far enough downstream to extend into RE, and b) positioned such that passing-by storms can benefit from upper-level divergence in the jet entrance or jet exit.

Let us explore typical Atlantic jet regimes and their positions which may satisfy these two conditions. The mean behaviour of the strongest winter jets is such that we have an eddy-driven jet over the US East Coast and a thermally-driven jet over Northern Africa (Athanasiadis et al., 2010). It is primarily the eddy-driven jet which is expected to affect the storms studied here. However, climatologically-speaking, this eddy-driven jet is positioned upstream, and not always so far downstream into RE. Several studies have explored the structure and positioning of transient jet regimes (on daily scales) over the Atlantic. For instance, Madonna et al. (2017) identify three primary jet regimes based on a central, southern, and northern position, which all represent deviations of the eddy-driven jet from its mean position. The southern position is assumed to be associated with the merging of both the thermally- and eddy-driven jets. The central and southern jets are situated in such a way that cyclones generating in RW and intensifying in RE can benefit from upper-level divergence at the jet entrance and exit, respectively. They are shifted downstream enough so that cyclones can intensify in RE as they enter Europe, maximizing their footprint. Hence, it is likely that higher European footprints are associated with synoptic time periods where a strong jet anomaly is positioned downstream over the East Atlantic, potentially in a southern or central position, so that the storm can benefit from divergence at the its left exit. Woollings et al. (2010) further explain that the position and strength of these jets are partially dependent on the North Atlantic Oscillation (NAO) and Eastern Atlantic (EA) circulation patterns, the former of which is explored further in Chapter 4.
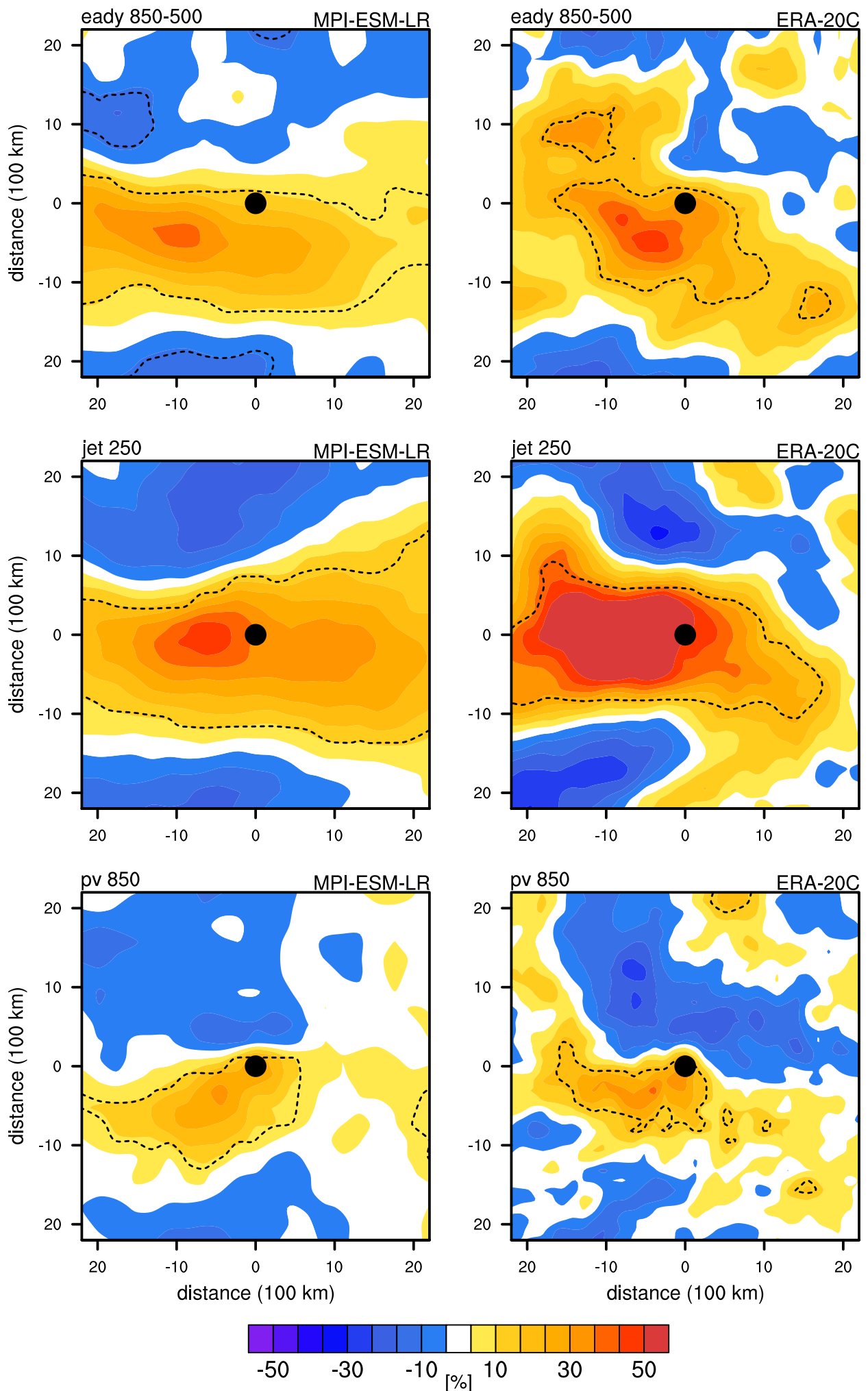
Figure 25: Percentage changes (%) in EGRs at 850-500 hPa (top), the jet stream at 250 hPa (middle), and PV850 anomalies (bottom, "pv 850") between high and low European footprint storm systems, for both MPI-ESM-LR (left) and ERA-20C (right) data. The geometrical conventions are the same as Figure 23. These cyclones necessarily experienced maximum intensification in RE, and the composites are centered on the point in time and space of cyclone maximum intensification.

3.6 Diabatic signals at cyclone maximum growth

As a proxy for diabatic development within the cyclone, PV850 is examined. The compositing and differencing procedure used here is identical to that used in Section 3.5. At the maximum intensification stage in RE, Figure 25 shows a marked increase in the magnitude of PV850 anomalies in the vicinity of the cyclone by up to 30 %. The anomalies are tightly wrapped around the cyclone core and are anchored on its southwestern flank, taking an elliptical shape, and diminish rapidly at a radius of around 500 km. These signals are consistent between both sets of data. A stronger PV850 anomaly in turns leads to anomalous cyclonic circulation at this level, aiding in the development of the cyclone. It acts to strengthen the coupled effect of lower- and upper-level circulations as is expected for baroclinic instability. These results indicate that higher footprint windstorms are associated with increases in the extremities of PV850 anomalies during the intensification of their parent cyclones in the Eastern Atlantic.

Let us discuss the implications of increased PV850 anomaly magnitudes. Although the quantitative attribution of PV anomalies to specific processes is beyond the scope of this study, we can still speculate as to the most likely processes responsible. While it may appear that the positive PV850 anomaly signals are simply indicative of higher vorticities associated with stronger cyclones, we are focusing on exclusively maritime systems. It is thus likely that diabatic processes associated with latent heat and moisture play an important role. There are several studies to support this notion (e.g. Davis, 1992; Davis et al., 1996; Rossa et al., 2000), studies which additionally focus on North Atlantic extra-tropical maritime systems. With regards to latent heat, Ahmadi-Givi et al. (2004) demonstrate, using observational data, that lower-level PV played a significant role in the development of an explosive cyclone, which intensified in the East Atlantic before continuing into Europe. This anomaly was centered around the 850 hPa level and was confirmed to be produced by latent heat; it was similarly elliptical in shape and wrapped around the cyclone core. Similarly, Büeler and Pfahl (2017) simulated the damaging cyclone Klaus and additionally found a similar low-level PV development associated with latent heat release. However, lower-level diabatic effects can include friction. For this, we look to Adamson et al. (2006), where they find that positive PV anomalies associated with friction impede the development of the idealized cyclone; however, this is actually confined the atmospheric boundary layer. Given that PV850 is computed just above the this layer, and that the majority of our systems intensify over the ocean (i.e. an increase in the availability of moisture), it is far more likely that latent heat is the predominant contribution to these anomalies.

3.7 Influence of thermal gradients at cyclogenesis

The relationship between European windstorm footprints and their occurrences with respect to LSCs and SST gradients is described here.

3.7.1 Land-sea contrasts

A cursory glance at the $|\nabla T_{2m}|$ ONDJFM climatologies for both data sets shows maxima positioned over the US East Coast and Greenland. With respect to the former, these gradi-

ents to some degree reflect the arc of tighter SST gradients positioned over the Gulf Stream. However, high gradients of around 2 K / 100 km can be seen further inland towards Connecticut and Massachusetts in both data sets. In ERA-20C in particular, strong LSCs with similar magnitudes are additionally located around Baffin Island. Lastly, the highest LSCs can be found on the Southeast coast of Greenland. From Section 2.8 it is clear that LSCs around the US East Coast have the greatest potential to affect our windstorms. However, we will discuss later if, and how, the strong LSCs near Greenland could affect the evolution of such windstorms.
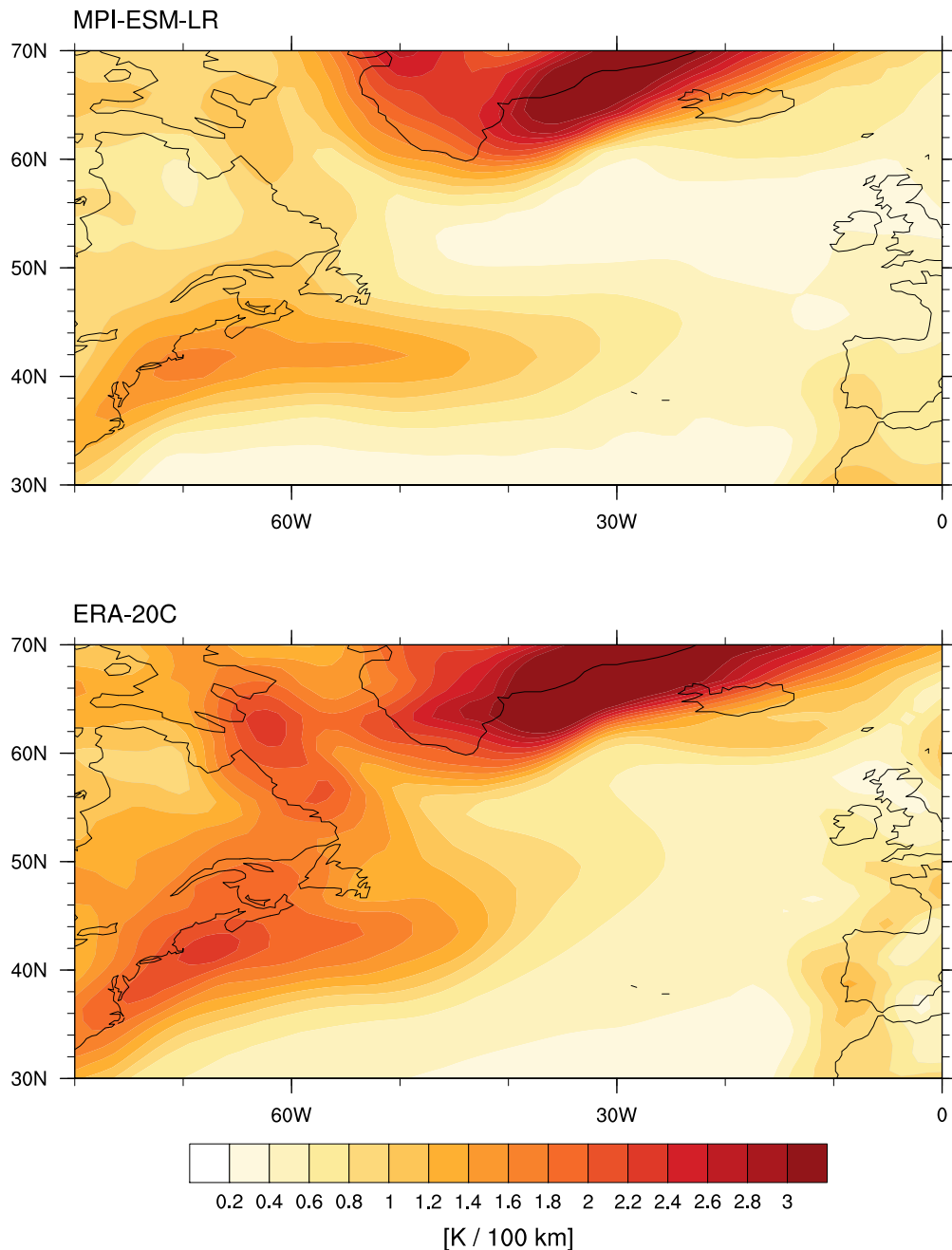
Figure 26: Climatology of $|\nabla T_{2m}|$ (ONDJFM) for MPI-ESM-LR (top) and ERA-20C (bottom).

To begin with, we focus on changes in LSCs with respect to European windstorm footprints, shown in Figure 27. In order to interpret an LSC, we focus on signals of $|\nabla T_{2m}|$ in the vicinity of the coastline, as the field is smoothed in a 500 km radius and so the signal encapsulates part of the un-filtered signal directly on the coastline. In MPI-ESM-LR, a small region near Newfoundland shows LSCs with statistically significant increases of up to 16% for high versus low European footprints. In ERA-20C, this signal is much stronger and more widespread: increases in LSCs of up to 25% are visible from Newfoundland to

northern regions of the US East Coast. The latitudes of these signals are collocated with the latitudes typically associated with the eddy-driven jet stream and high lower tropospheric baroclinicity. Altogether, we see that LSCs could relate to cyclone development by directly interacting with them (e.g. through convergence lines as described by Minobe et al., 2008), or by forcing baroclinicity and jet stream anomalies in the overlying atmosphere which in turn encourage cyclone growth. Naturally, a third option is that the LSC anomalies are actually dependent on tropospheric baroclinicity (e.g. other effects intensify the eddy-driven jet above, which in turn intensify LSCs by tightening surface temperature gradients).

We compare these results to Brayshaw et al. (2009), who explored the role of the land-sea contrast in modulating North Atlantic extra-tropical storm tracks in idealized models, and found that it contributes to locally enhanced EGRs and storm tracks. Nakamura and Yamane (2009) further found higher surface-level baroclinicity anomalies focused on Newfoundland with a zonal extension, a pattern similar to what we found in Figure 27. This supports the idea that LSCs likely force local anomalies in baroclinicity, which is in turn utilized to fuel intensive cyclone systems nearby.

MPI-ESM-LR

ERA-20C
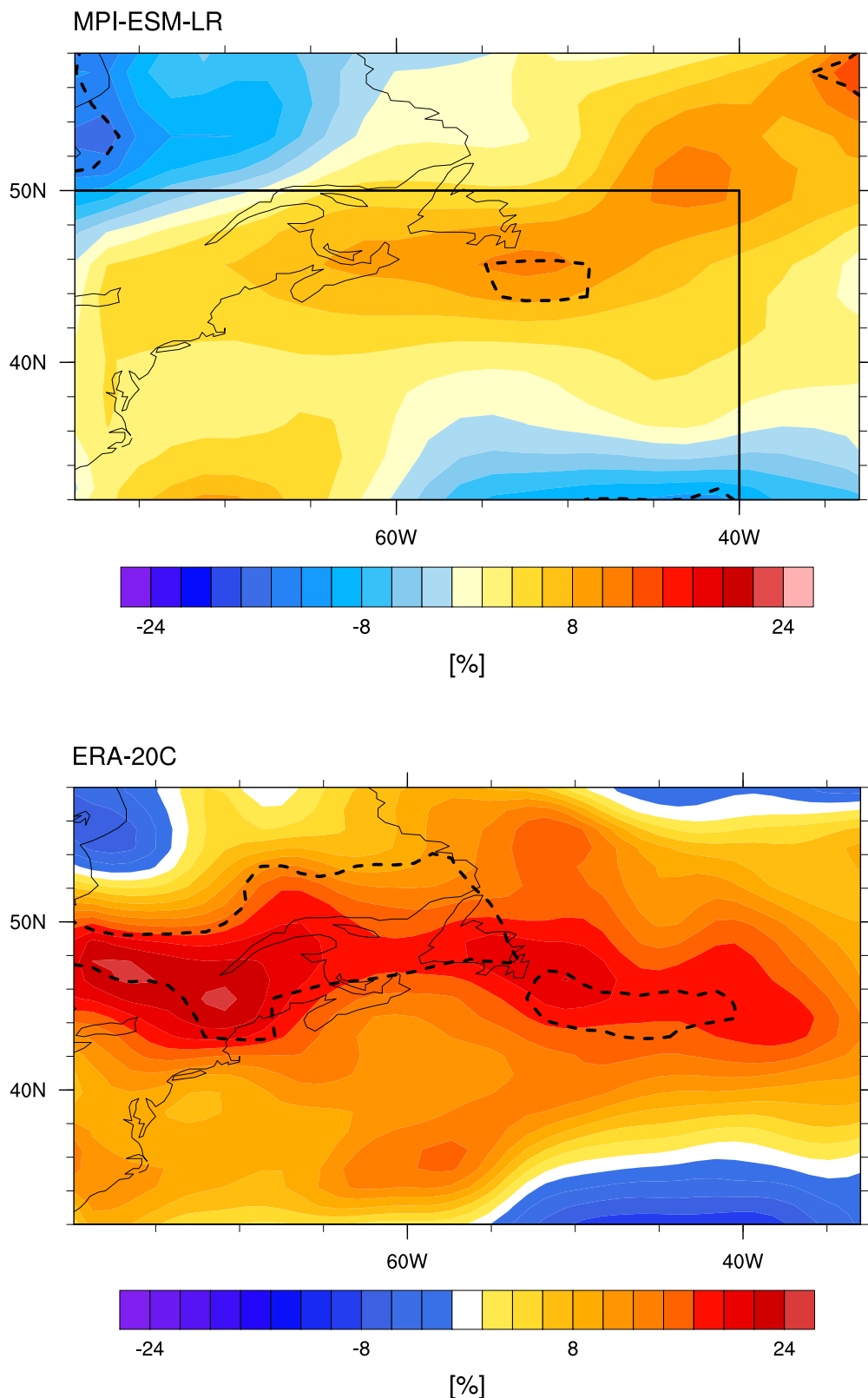
Figure 27: Percentage changes in $|\nabla T_{2m}|$ composites for high against low footprint cyclones at their genesis point in RW. Dashed contours represent changes significant to $p < 0.05$ using a Welch two-sided t-test. The box represents the region in which these cyclones generated.

3.7.2 SST gradients

From the climatology of SST gradients in Fig. 28, we see in the Eastern Atlantic that it is orders of magnitude lower compared to the Western Atlantic, thus we constrain the SST gradient analysis to the Gulf Stream region (there are aditionally tight gradients near Greenland, but we do not focus on systems which generate here). Also visible in this climatology is the difference in the tilt of SST gradients between each data set. In MPI-ESM-LR, the gradients are more zonal compared to ERA-20C. This has important implications for the tilt of the North Atlantic Current and the storm track as well (Jungclaus et al., 2013), a concept

61

we will revisit later. Around the Western Atlantic, SST gradients are only considered in terms of their meridional components, whose average magnitudes are ~ 6 and ~ 3.5 times higher than the zonal components over the considered time period for MPI-ESM-LR and ERA-20C, respectively. These climatologies show some similarities to those of LSCs (Fig. 26), so that the mean behaviour of both fields would appear to be similar around the Gulf Stream region (e.g. Jacobs et al. 2007). On a daily scale they are highly correlated in this region specifically (not shown). However, the two variables are not necessarily equivalent. Due to their atmospheric nature, LSCs operate on higher frequencies and are modified by feedbacks from overlying cyclones differently to SSTs. SSTs are naturally modified by marine boundary layer processes as well.
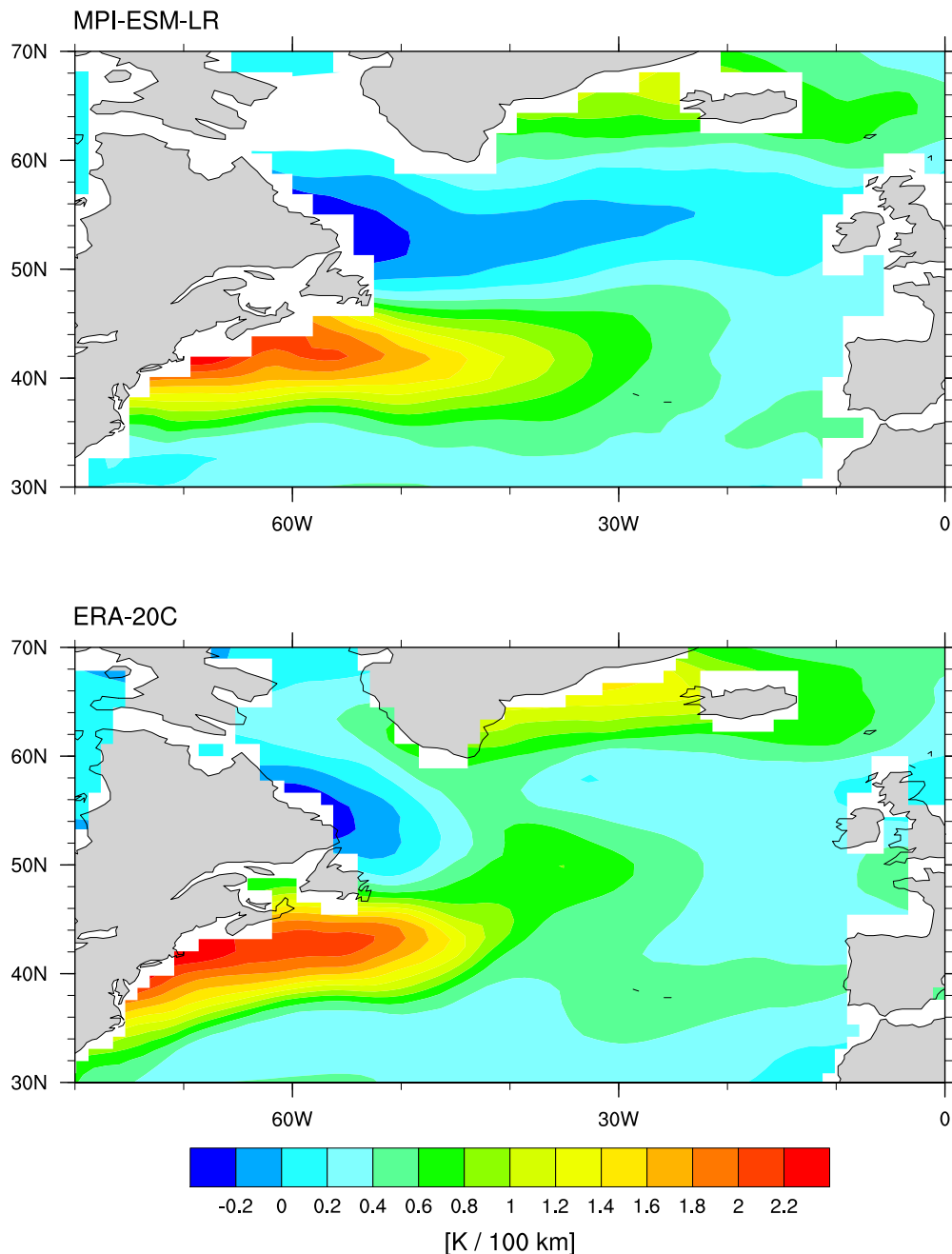
Figure 28: Climatology of meridional SST gradient (ONDJFM) for MPI-ESM-LR (top) and ERA-20C (bottom).

SST gradient composites did not show a statistically significant signal with respect to the European windstorm footprint. The challenge of finding relationships between SST gradient and cyclone intensities is consistent with the findings of Vries et al. (2019), who find relationships between SST gradients and surface heat fluxes, but not necessarily with cyclone vorticity or surface wind speeds.

To investigate this further, we instead consider how the SST gradients are related to the *occurrence* of a European windstorm. Although this cannot establish a direct relationship between SST gradients and windstorm footprint magnitudes, it does provide a sense of whether SST gradients are related to European storm systems at all. To achieve this, a composite of SST gradients for all time steps in which a cyclone generated in RW is created (given that the cyclone later produced a European windstorm which lasted for at least one day). By filtering in this way, we consider 912 and 287 storms for MPI-ESM-LR and ERA-20C data, respectively. These signals are compared against the ONDJFM climatology, so that increases in the signals shown in Figure 29 correspond to stronger gradients than the mean. In MPI-ESM-LR, statistically significant increases of up to 52% relative to the climatology can be seen, particularly directly near the coastline. Higher increases are close to South and North Carolina, and reduced increases closer to Maine and Nova Scotia. The ERA-20C results displayed weaker changes of up to 24%, with significant changes of around 9 — 15% around Nova Scotia, New York, and Pennsylvania. These results collectively illustrate that stronger SST gradients are conducive with increased European windstorm activity, but other factors will control their European footprint and the relationship is relatively data-dependent.

Comparing to previous works, the MPI-ESM-LR results are consistent with the findings of Sampe et al. (2010), who found in an idealized model that mid-latitude SST gradients are essential in restoring baroclinicity required to sustain the North Atlantic storm track and hence storm activity. They found that without these gradients, the position of the storm track shifts further Southwards, which could potentially affect the number of strong European systems (for example, systems could instead drift too far South). Relationships between tighter SST gradients and windstorm occurrence in MPI-ESM-LR have additionally been discovered by Nissen et al. (2014), where increased North Atlantic gradients were associated with higher decadal windstorm activity, although these gradients are not only concentrated over the Gulf Stream, but downstream as well. The ERA-20C results are comparable to that of Varino et al. (2019), who found that intensification of SST gradients lead to an increased frequency of above-average strength extra-tropical cyclones over the North Atlantic.
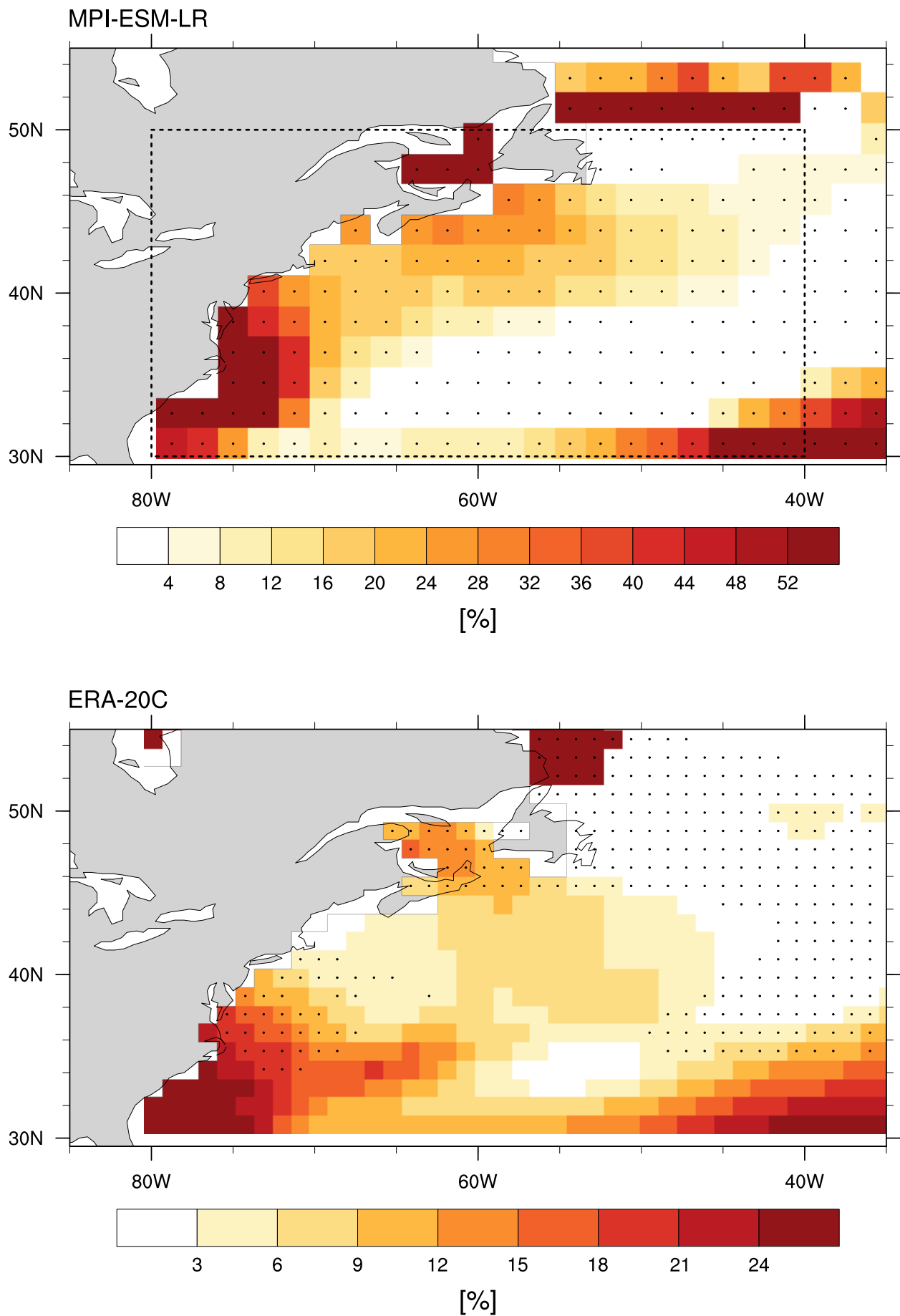
Figure 29: Percentage changes in meridional SST gradient for all time steps where any European windstorm's cyclone generated in RW (denoted by dashed box in top) versus the ONDJFM climatology, for MPI-ESM-LR (top) and ERA-20C (bottom). Note the different color bar scales for each plot. Stippled gridboxes are values significant to p < 0.05 using a Welch two-sided t-test.

There are a few possible reasons for the stark differences in SST gradient signals between the two data sets. For one, MPI-ESM-LR utilizes an explicitly coupled ocean and atmosphere, resulting in potentially different feedbacks between passing-by cyclones and SSTs,

64

and hence thermal gradients. It shows biases in the path of the North Atlantic Current (Jungclaus et al., 2013), such that waters are normally warmer around Gulf Stream and colder to the East of Newfoundland. Such a combination could lead to systematically higher gradients on average compared to observations. Another complication is that cyclones should theoretically smooth out both SST and T_{2m} gradients in its vicinity, a process which may be captured more accurately in ERA-20C for SST gradients in particular. One must further consider that the resolution of both data sets is significantly different, and that despite the fact we smoothed each data set in a fixed radius, there will still be discrepancies due to differently-resolved processes. For example, Parfitt et al. (2017) show that atmospheric front occurrence is strongly affected by the resolution of the underlying SST distribution. Furthermore, Scher et al. (2017) demonstrated that precipitation and convection associated with SST gradients is reduced in lower-resolution data sets as well.

3.7.3 Comparison of SST gradients and land-sea contrasts

Here, we directly compare the two types of thermal gradients. As SST gradient signals are geographically very close to where we find LSC signals, we will attempt to disentangle the two variables where possible. To begin with, composites related to European windstorm occurrence are aditionally constructed for $|\nabla T_{2m}|$ as shown in Figure 30, again compared its climatology displayed in Figure 26. Both MPI-ESM-LR and ERA-20C agree that there are significant increases in LSCs with respect to the occurrence of a European windstorm. In MPI-ESM-LR, these increases are located in the same regions as described previously (North and South Carolina, Nova Scotia, and Newfoundland). They are relatively strong increases ranging between $40 - 100\%$, and are partially congruent with the changes seen in Figure 29. In ERA-20C, these increases are more congruent with the coastline itself but with weaker increases ranging between $14 - 30\%$ (a zonal band of 20% increases can be identified further south, but over the ocean only). In fact, both of these results display their weakest signals around the Gulf Stream itself, consistent with the weaker SST gradient signals described above. Moreover, high cyclone activity over the Gulf Stream will tend to suppress any $|\nabla T_{2m}|$ signals. Thus, both fields show weaker signals over the Gulf Stream itself due to this suppression, but sustained gradients towards Newfoundland or South Carolina.

MPI-ESM-LR

ERA-20C

Figure 30: As Figure 29, but for changes in $|\nabla T_{2m}|$. All changes are significant to $p < 0.05$ using a Welch two-sided t-test.

To summarise the role of thermal gradients, we begin by discussing how their anomalies relate to the magnitude of the European footprints. First, we compare high against low

footprints. For LSCs, zonally-extended increases in their strength around Newfoundland and Nova Scotia can be seen in both MPI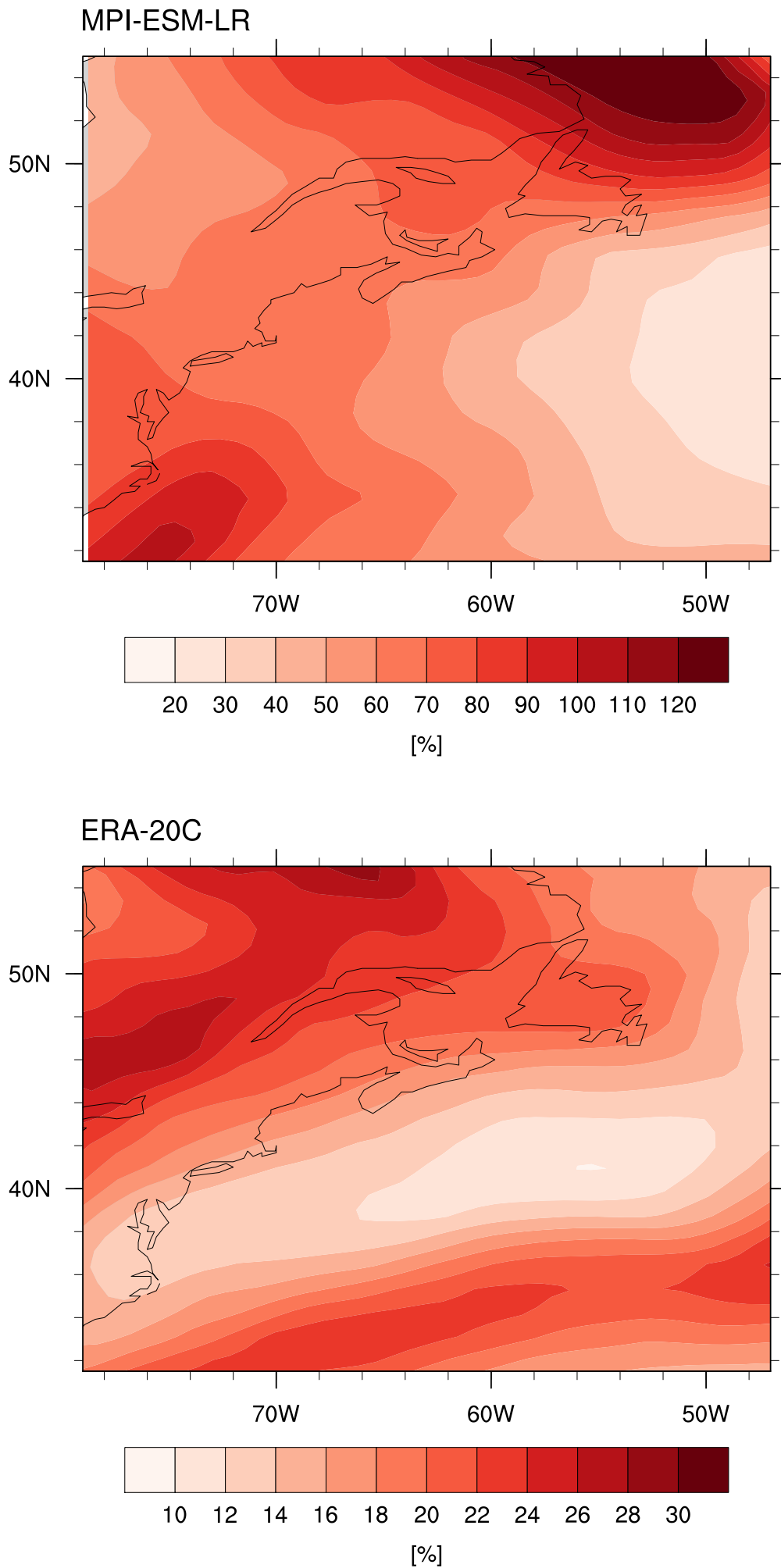-ESM-LR and ERA-20C. The proposed mechanism connecting the strength of the LSCs to the subsequent strength of the European windstorm is similar to that described in Section 3.4: stronger LSCs leads to higher baroclinicity and higher radii cyclones, which itself leads to larger systems with higher footprint windstorms. However, no discernible signal could be found for SST gradients.

This prompted us to identify how the occurrence of all European windstorms relate to the magnitude of thermal gradients. The two data sets agree that LSCs are stronger than the climatology when the system's cyclone generates in RW and produces a European windstorm. However, they marginally agree on the effect of SST gradients; MPI-ESM-LR illustrates a significantly increased signal compared to ERA-20C, albeit a similar structure. Altogether, we can see that LSCs appear to play a more crucial role in the occurrence and footprint magnitude of a European windstorm, and that the role of SST gradients is related to their occurrence, but still needs to be further investigated as it is more sensitive to the underlying data.

3.8 Summarizing the role of CGFs

In this chapter, we attempt to answer the question: "How do the strength, positioning, and timing of cyclone growth factors relate to the windstorm footprint?". We have explored five factors pertaining to cyclone genesis and intensification, and their relationship to the European windstorm footprint they produce. These were related to storms that are primarily maritime in nature, i.e. those which generate or intensify over the North Atlantic ocean. We calculated the percentage changes in anomalies of these factors between two sets of cyclones: those creating anomalously high, and those creating low European footprints.

To begin with, we identify changes associated with baroclinic factors such as the jet stream or EGRs. For systems which generate in the West Atlantic[3], they are associated with stronger EGRs and jet streams; the two variables had similar signals of significance, taking a pseudo-elliptical shape. However, the two data sets (three members of MPI-ESM-LR historicals and ERA-20C) disagreed in the exact position of these anomalies. At the genesis phase in the East Atlantic, we see a similar result for EGR and jet anomalies: similar orders of magnitudes and shapes, but the datasets disagree in their position relative to the cyclone core. At the intensification phase of systems in this region, we see a strong, zonally-extended jet and EGR signal consistent between both data sets. These increases were up to 50% stronger near the cyclone core for the high footprint storms. We looked at diabatic signals with PV850, which could only be found at the intensification phase of storms in the East Atlantic. In both data sets, tightly wrapped anomaly increases of up to 30% could be found near the cyclone core. As most of these systems intensified over the ocean, it is probable that these are associated with higher latent heat release in the cyclone core. Finally, we looked at the effects of thermal gradients. We found that significantly stronger and zonally-extended land-sea contrasts situated over Newfoundland are associated with higher footprint storms, especially in ERA-20C. These signals could be collocated with the storm-centered EGR and jet composites previously described, i.e. the two factors are coupled

---

[3]That is, European windstorms spawned by their parent cyclone generating in the West Atlantic.

to one another. However, SST gradients showed no signal with respect to the strength of the European windstorm footprint. This prompted an investigation into how SST gradients may instead affect the occurrence of a cyclone that goes on to form a European windstorm. This was done by computing SST gradient magnitudes at the genesis phase of European windstorm-forming cyclones that generated in the Western Atlantic. These magnitudes were found to be stronger than the winter climatology in MPI-ESM-LR, and less so in ERA-20C. Altogether, this suggests that strong thermal gradients are often a necessary but not sufficient condition for high footprint storms in Europe. However, the significantly different SST gradient signals in both data sets calls for further exploration of these relationships.

Let us integrate these results into a framework which describes the most likely evolution of a high footprint European windstorm. From Section 2.8, we found that high footprint storms most likely form in RW and intensify in RE. From the results of this chapter, we found that these cyclones are associated with higher baroclinicity at both its genesis and intensification phases, along with higher diabatic release during its intensification, and are likely associated with moisture. Moreover, the presence of strong surface thermal gradients — primarily associated with LSCs — at its genesis phase in RW could increase baroclinicity throughout the lower- to mid-troposphere. This increased baroclinicity increases the probability that cyclogenesis occurs in RW in the first place. In addition, we hypothesized that increased baroclinicity in this region leads to higher radii cyclones, which will produce more destructive windstorms. However, this alone is not sufficient to create the high European footprint. First, the storm must traverse the North Atlantic Ocean, ideally towards Europe. Having slowly grown for around two days (see Section 2.8), it encounters a strong jet and/or baroclinicity anomaly which will aid in the intensification of this system in RE, before it enters Europe with a newly-formed and intensified windstorm, imprinting a high footprint.

For alternative pathways that can produce high footprint European windstorms, we recall from both the previous and current chapters that a reduced proportion of high footprint storms generate in RE instead. These systems undergo slightly different evolutions. Many of these storms form in the central Atlantic or towards regions of high land-sea contrasts near Greenland and Iceland. They could additionally form from secondary cyclogenesis from the frontal systems of primary cyclones. However, the subsequent processes still apply: a maximum intensification on the Western flank of the European region due to a jet anomaly, followed by a maximized footprint within the region.

There are a number of ways to further explore how CGFs can influence the development of European storms. For instance, stationary-wave patterns contribute significantly to cyclogenesis in RW (e.g. Brayshaw et al. 2009, Jacobs et al. 2005) and could be incorporated as another forcing. Moreover, other diagnostics like the pressure tendency equation (e.g. Pirret et al., 2017) could be employed to quantify and compare dominant processes between high and low footprint systems which generate and intensify in different regions. Finally, the life-cycle of Eastern-generated storms should be explored by identifying secondary cyclogenesis as a key factor.

4 Generalized Linear Models for European windstorm footprints

> All models are wrong, but some are useful.
>
> _George E.P. Box_

The previous chapters characterised a number of competing factors which could be related to an anomalously low or high European storm footprint. With such a high number of factors (which can broadly be described as meteorological or geographical), we may wish to weight their contribution to the footprint. One way to approach this problem is to build a Generalized Linear Model (GLM). The GLM can be used in an explanatory manner, and opens the possibility to quantify a relative contribution of each factor to a given storm footprint. It allows for a direct comparison of dominant factors between MPI-ESM-LR and ERA-20C data. Further, it can bridge the gap between extreme classes of storm footprints by considering all footprints in between. In the following sections, the building blocks of a GLM are described, followed by the selection and construction of the predictors. Predictors are built based on the variables and concepts explored in the previous chapters. This provides a framework for the GLM which focuses primarily on all European storms.

4.1 General construction of the GLM

A GLM is comprised of three components: the random component Y (also described as the response variable, in this case the footprint), the systematic component (the k predictors $X_1, ..., X_k$), and the link function g (McCullagh and Nelder, 2019). It is broadly described by the equation

$$g\{\mathbb{E}[Y]\} = \beta_0 + \sum_{i=1}^{k} \beta_i X_i, \tag{6}$$

where β_0 represents the intercept term, β_i are the parameters (or regression coefficients) associated with each predictor X_i, and $\mathbb{E}[Y]$ is the expected value of Y with a link function g. It is assumed that Y is generated by a distribution including but not limited to the normal, binomial, Poisson, and Gamma distributions. The link function of a GLM models the relation of the expected value of the response variable to the set of linear predictors on the right hand side of the equation. In this instance, because our response variable (the storm footprint) is positive and continuous, we use a Gamma distribution coupled with a log-link function. More formally,

$$\log(\mathbb{E}[Y]) = \beta_0 + \sum_{i=1}^{k} \beta_i X_i, \tag{7}$$

with a response distribution $Y \sim \Gamma(\mu, \nu)$, where μ and ν are its parameters which are estimated using maximum likelihood estimation, and will shortly be described in more detail. In the model results we will briefly discuss the usage of the Gamma model formulation against a simpler linear model using a log-transformation of the response variable. We see

from Equation 7 that the overall structure is very similar to simple linear models: $\log(\mathbb{E}[Y])$ is related to the right hand side linearly in the β terms.

In the chapters to follow, we can represent equations with a similar notation of the form `y ~ a + b ...`, where `y` is the response variable regressed onto the predictors `a + b + ...` (McCullagh and Nelder, 2019). It is already assumed here that we are relating the expected value of the response to the right hand side with a log-link function, and that each predictor includes its associated β parameters.

The derivations to follow can all be found in Wood (2017). To derive the parameters μ and ν we first derive expressions from the probability mass function for any exponential distribution, written as

$$f_\theta(y) = \exp[y\theta - b(\theta)/a(\phi) + c(y, \phi)]. \tag{8}$$

Here, a, b, and c are arbitrary functions, ϕ the scale parameter, and θ the canonical parameter. These parameters can be estimated through the use of the log-likelihood function $l(\theta)$, defined as

$$l(\theta) = \log f_\theta(y) = [y\theta - b(\theta)]/a(\phi) + c(y, \phi). \tag{9}$$

From here, we can derive the expressions:

$$\frac{\partial l}{\partial \theta} = y - b'(\theta)/a(\phi), \tag{10}$$

and

$$\frac{\partial^2 l}{\partial \theta^2} = -b''(\theta)/a(\phi). \tag{11}$$

It can further be shown that

$$\mathbb{E}\left[\frac{\partial l}{\partial \theta}\right] = \{\mathbb{E}[Y] - b'(\theta)\}/a(\phi) = 0, \tag{12}$$

so that we arrive at the result

$$\mathbb{E}[Y] = b'(\theta). \tag{13}$$

Similarly, it can be shown that

$$\mathbb{E}\left[\frac{\partial^2 l}{\partial \theta^2}\right] + \mathbb{E}\left[\left(\frac{\partial l}{\partial \theta}\right)^2\right] = 0, \tag{14}$$

giving

$$b''(\theta)/a(\phi) = \mathbb{E}[(Y - b'(\theta)^2]/a(\phi)^2. \tag{15}$$

Defining $\mathbb{E}[(Y - b'(\theta)^2)] = \text{var}(Y)$ and rearranging gives

$$\text{var}(Y) = b''(\theta)a(\phi). \tag{16}$$

Thus we have general expressions for the expected value (Equation 13) and variance (Equation 16) of exponential family distributions. Let us return to the Gamma distribution, which has the probability density function of the form

$$f(y) = \frac{1}{\Gamma(\nu)}\left(\frac{\nu}{\mu}\right)^\nu y^{\nu-1}\exp\left(-\frac{\nu y}{\mu}\right). \tag{17}$$

By comparing this with the exponential probability density function in Equation 8, it can be shown that $\theta = -(1/\mu)$, $\phi = 1/\nu$, $a(\phi) = \phi$, and $b(\theta) = -\log(-\theta)$. This gives the mean and variance of μ and μ^2/ν, respectively. The key feature to note here is that the variance of the distribution scales with the square of the mean.

Lastly, we wish to fit the model itself by estimating the values of β_i which is achieved through maximum likelihood estimation (MLE). We define the log-likelihood of β as

$$l(\beta) = \sum_{i=1}^{n} \log[f_{\theta_i}(y_i)], \qquad (18)$$

where it is implied that l is dependent on β through θ_i (see Equation 13; the expected value itself is determined by β). The aim of MLE is to take the derivatives with respect to each β, $\partial l/\partial \beta$, and solving for β by equating these expressions with zero. This is done using the iteratively re-weighted least squares method, where its precise algorithm is discussed in more detail in Wood (2017). To summarize this method, the user starts from a modified form of Equation 18, and guesses initial β estimates to solve for different parameters. By doing so, one obtains estimates for β at the next step and this is repeated until convergence is achieved.

In Section 4.5, we will explore further the distribution of the footprints and how they relate to individual predictors, while describing the benefits of studying the footprints in log-transformed space. In Section 4.6 we will explore the results of these models.

4.2   Selection, construction, and screening of predictors

A frequent challenge in climate science is the representation of multi-dimensional spatiotemporal fields as univariate quantities. For example, teleconnection patterns like the NAO or PNA are represented as the projection of a geopotential height anomaly field onto a loading pattern produced by Principal Component Analysis (PCA) or Empirical Orthogonal Functions (EOFs). Another common example is the construction of the Atlantic Multidecadal Oscillation (AMO), which is a field mean of North Atlantic Ocean SST anomalies. For all intents and purposes, "factors" are effectively the predictors used in our GLM. Predictors can be defined as continuous, categorical or binary variables. Table 6 summarizes all the predictors used in the following sections, their type, and their specific definitions. Predictor definitions are consistent between both MPI-ESM-LR and ERA-20C data.

Atmospheric cyclone intensification factors

In Section 3 we found significant increases in the strength of EGR, jet, and PV anomalies in the vicinity of an intensifying cyclone with respect to the storm footprint. The EGR and jet signals are associated with increased baroclinicity during the cyclone maximum intensification timestep, while PV anomalies are associated with increased latent heat release at this same timestep. All variables here are taken at the time just preceding cyclone maximum intensification (recall that we select the maximum anomaly values in the last 5 time steps preceding this point). We do not include these variables at the genesis phase of cyclones, primarily because they were shown to be much stronger at the cyclone intensification phase in comparison (see Figure 25). Moreover, the signals between the two data sets agreed better

Predictor	Type	Description
eady	continuous	EGR field mean in $20° \times 10°$ storm-centered region at MI
jet	continuous	jet field mean in $20° \times 10°$ storm-centered region at MI
pv	continuous	PV field mean in $\sim 5°$ radius storm-centered region at MI
lsc	continuous	field mean of total land-sea contrast in 80°-60°W 30°-50°N
sstg	continuous	field mean of meridional SST gradient in 80°-60°W 30°-50°N
greg	categorical / binary	region of cyclone genesis
mireg	categorical / binary	region of cyclone intensification
nao	continuous*	daily NAO index at MI
b	continuous	storm bearing at MI

Table 6: List of predictors used for the statistical models. "MI" refers to the maximum intensification point of the cyclone. The * is to note that we will explore a binary alternative of nao in Section 4.5.2.

at the intensification timestep.

Since the EGR and jet signals in particular were very similar, we collectively describe them as "baroclinic signals" and apply the same field-mean averaging techniques to construct their predictors. The baroclinic signals typically appear as zonally elongated bands which are centered, upstream, or downstream of the cyclone (e.g. Figure 25). Systems may either emerge from a baroclinic zone upstream or travel into a zone downstream. Thus we express these predictors as the field mean of a $20° \times 10°$ longitude $\times$ latitude band centered on the storm; name this region B. The latitudinal range is of the order of a typical cyclone radius (~ 1000 km), while the longitudinal range (~ 2000 km) accounts for the zonal extension of these anomalies, as well as the fact most systems have a strong zonal velocity. Thus we arrive at their respective equations:

$$\texttt{eady} = [EGR(s, t = t_{MI})]_B \qquad (19)$$

and

$$\texttt{jet} = [jet(s, t = t_{MI})]_B, \qquad (20)$$

where EGR and jet are the Eady Growth Rate and jet fields, s a point in longitude and latitude space centered on the windstorm's parent cyclone at a time $t = t_{MI}$, MI the maximum intensification rate, and the square brackets represent the spatial average over the latitudinal band described above.

PV anomalies are typically smaller and more elliptical features which are tightly wrapped around the cyclone center during its intensification (e.g. Figure 25). This motivates a radial field mean with a radius that captures enough of the anomaly information. As an example, Čampa and Wernli (2012) characterise PV anomalies as field means within a cyclone radius of O(100 km). It was found by eye that a radius of 500 km most accurately captured the anomaly signal on average. A sensitivity test across radii of 300, 400, and 600 km was additionally conducted, and was found to produce relatively similar results in the statistical models. Similar to Equations 19 and 20, the equation for this predictor is

$$\texttt{pv} = [PV850(s, t = t_{MI})]_R \qquad (21)$$

where R represents the radial region for the spatial averaging described above.

Surface temperature gradients

Surface temperature gradient predictors are computed at the cyclone genesis timestep for all cyclones (as we did in Section 3), and are comprised of the land-sea contrast and SST gradient variables. As described before, both land-sea contrasts and SST gradients are known to play a crucial role in restoring baroclinicity in the Western Atlantic, or aiding in the generation and/or intensification of cyclones. Section 3.7 described a significant relationship between meridional land-sea contrasts and extremes of European storm footprints in both MPI-ESM-LR and ERA-20C.

We therefore characterise these gradients as univariate quantities by taking field mean averages over the US coastal region denoted by the boundaries in Table 6. Call this region USE. Land-sea contrasts were expressed in a similar way in Day and Hodges (2018). Regions far from the coast are excluded from the field mean (inland of the US, or further into the North Atlantic Ocean) by padding their grid boxes with missing values. The equation for LSC_x or LSC_y is

$$LSC_{x,y} = [LSC_{x,y}(s, t = t_{GEN})]_{USE}, \tag{22}$$

where the notation is the same as before, except t_{GEN} is at the time of cyclogenesis, and s is any spatial point in the fixed USE region. We write the land-sea contrast predictor as the total magnitude

$$\texttt{lsc} = \sqrt{LSC_x^2 + LSC_y^2}. \tag{23}$$

The individual components were previously included as standalone predictors, but it was found that the total gradient produced more descriptive statistical models overall. The sign of LSC_x and LSC_y is important in terms of their contribution to local baroclinicity, and should be positive and negative, respectively (Niehaus, 1980; Nakamura and Yamane, 2009). As we take the square of each of these quantities, this means LSC components of the baroclinicity-reducing sign will still contribute positively to $\texttt{lsc}$. Thus, we checked the nature of sign changes for these quantities in both data sets. LSC_x was almost always positive with the occasional sign reversal; however, negative magnitudes were extremely small compared to positive ones. LSC_y remained strongly negative as well. Thus, we are confident that the total gradient $\texttt{lsc}$ accurately reflects contributions of LSCs to local baroclinicity.

SST gradients exhibit a relationship with the occurrence of European windstorms, but not necessarily with the extremes of their footprints (e.g. Figure 29). A relationship with the storm footprint may emerge if we look at all systems between the extremes, thus motivating the use of them as a predictor. To create the predictor $\texttt{sstg}$, SST gradients are additionally expressed as field means of the field $SSTG$ over a small region south of Newfoundland (regions described in Table 6), i.e.

$$\texttt{sstg} = [SSTG(s, t = t_{GEN})]_{USE}. \tag{24}$$

This contains a region of high SST gradient variability, but excludes regions too far North with anomalously high and extraneous grid points in small regions.

The North Atlantic Oscillation

The NAO is known to affect both the strength and trajectory of North Atlantic storms. A positive NAO phase is associated with a higher frequency of stronger European cyclones, and cyclones can alternatively affect the current phase of the NAO (Pinto et al., 2009). Although the NAO is typically characterised on monthly timescales, a daily index can be constructed in the following way. First, define the NAO pattern by computing the first EOF of monthly DJF 500 hPa geopotential height anomalies; call this $E_1(s)$, where s is a spatial coordinate (spanning all p unique longitude and latitude points on the grid). Then, take daily geopotential height anomalies, $Z'(t, s)$, where t is the time, and project them onto this pattern. This gives an equation for the NAO as a function of time,

$$NAO(t) = \sum_{s=1}^{p} Z'(t, s) E_1(s). \tag{25}$$

Finally, a 5-day running mean is applied to smooth the data, and similar to other predictors, we take the NAO value at the cyclone maximum intensification timestep. This gives the equation

$$\texttt{nao} = \overline{NAO}(t = t_{MI}), \tag{26}$$

where the overbar represents the 5-day running mean. Dynamically speaking, a positive NAO will be associated with a stronger cyclone and one which is directed into Northeastern Europe. Figure 31 illustrates the eigenvector associated with the NAO constructed in the aforementioned method. It clearly shows the bipolar structure of the NAO, with a center of action over Iceland and the Azores region. The only noticeable difference in the definition of the NAO between the two data sets is that ERA-20C appears to contain more variability in the geographical position of the southern center of action, as can be seen by the greater zonal extension.

The storm bearing

In Section 2.8, it was discussed that the storm footprint could depend on its direction of travel during intensification. That is, storms traveling in an easterly direction are more likely to remain or persist in the European region for a longer time, and those which deviate strongly from this direction are more likely to exit the region and reduce the potential to maximize their footprint. This is especially important if one considers that the European region has a large longitudinal-to-latitudinal distance ratio. Consider the cyclone at its maximum intensification point at a time t and point p_t, with a longitude λ_t and latitude ϕ_t, i.e. $p_t = (\lambda_t, \phi_t)$. At the previous time step it was at the point $p_{t-1} = (\lambda_{t-1}, \phi_{t-1})$. It can be shown trigonometrically that the bearing $B_{t-1,t}$ of the storm as it travels from p_{t-1} to p_t is

$$B_{t-1,t} = \arctan 2(\sin(\lambda_t - \lambda_{t-1}) \cos \phi_t, \cos \phi_{t-1} \sin \phi_t - \sin(\phi_{t-1}) \cos \phi_t \cos(\lambda_t - \lambda_{t-1})). \tag{27}$$

In addition, we are interested in the direction the storm travels after its maximum intensification $B_{t,t+1}$, and so we take the mean bearing $\hat{B} = (B_{t-1,t} + B_{t,t+1})/2$. To construct the predictor, $\texttt{b}$, we wish to use a function that is maximized when $\hat{B} = \pi/2$ (easterly direction of travel), and is opposite in sign if the storm is traveling the opposite way at $\hat{B} = 3\pi/2$.
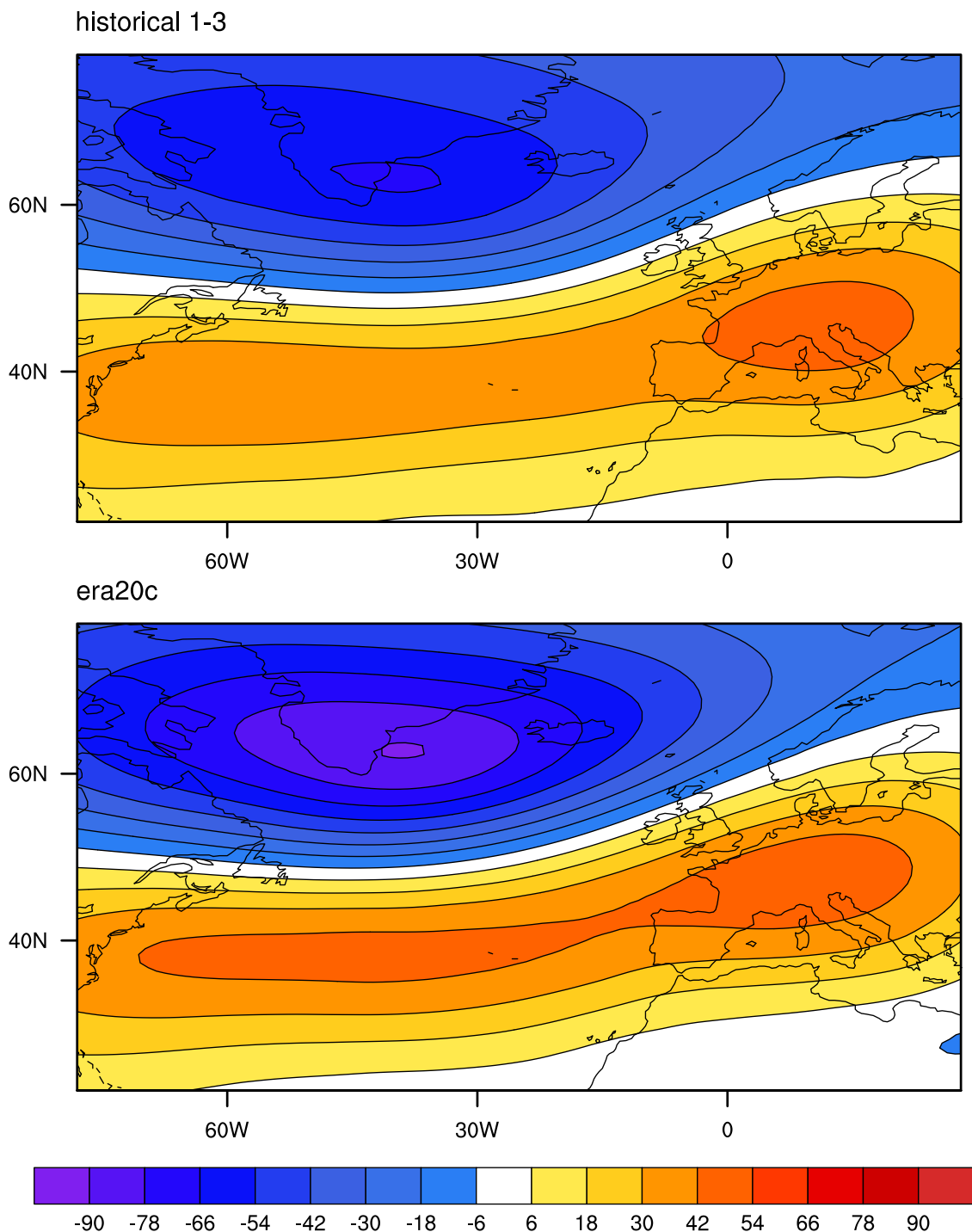
Figure 31: Monthly DJF 500 hPa geopotential height anomalies regressed onto the first principal component (in dm per PC standard deviation) for MPI-ESM-LR (top) and ERA-20C (bottom) data.

This is simply

$$\mathtt{b} = \sin(\hat{B}). \tag{28}$$

Regional predictors

A GLM can include a mixture of continuous and categorical predictors (Roths, 2018). Categorical predictors are useful in describing concepts or ideas which are otherwise impossible to express as a continuous physical variable. Two of such predictors are the regional predictors. These are the cyclone and genesis intensification regions, `greg` and `mireg`, respectively. For this particular study we represent each of these predictors with two levels, i.e. binary values of 0 and 1. From the results of Section 2.7, storms with anomalously high or low European footprints preferentially generate or intensify in West Atlantic (RW) or East Atlantic (RE), respectively. The boundaries defining RW and RE can be seen in Figures 15 and 16,

respectively. The predictors are defined as follows:

$$
\texttt{greg} =
\begin{cases}
1, & \text{if genesis in Western Region} \\
0, & \text{otherwise}
\end{cases}
$$

$$
\texttt{mireg} =
\begin{cases}
1, & \text{if max. intensification in Eastern Region} \\
0, & \text{otherwise.}
\end{cases}
$$

Thus we have converted two categorical variables to those with simple binary values. We should further consider how binary predictors can affect the left hand side of Equation 7. A number of continuous predictors were previously introduced and are relatively intuitive. For a continuous predictor X_P, they take on a range of values and contribute to $\log(\mathbb{E}[\texttt{ssi}])$ by an amount $\beta_P \cdot X_P$ within the range $(-\infty, \infty)$. However, for a binary predictor this contribution is either $\beta_B \cdot 1$ or 0. Thus binary predictors provide less information in explaining the relationship between a storm's footprint and regional development (and could be worked towards as a continuous predictor in future studies).

Interacting predictors

It is sometimes the case that the influence of multiple predictors combined differs substantially from the sum of their individual effects. In this case, the modeler can choose to include interaction terms, i.e. terms that couple multiple predictors together (Dobson and Barnett, 2008). As a simple example, say we construct a model $\texttt{y} \sim \texttt{a + b}$. In this simple case, the effects are additive. Our parameter estimations will show us the effect of any given predictor on the response variable, keeping all other predictors constant. Assume we have reason to believe that there is a strong interaction between $\texttt{a}$ and $\texttt{b}$ such that their influence on $\texttt{y}$ is greater than just the parameters associated with $\texttt{a}$ and $\texttt{b}$ individually. For example, assume a model

$$
y = \beta_0 + \beta_1 a + \beta_2(a)b, \tag{29}
$$

where we assume b interacts with a, as its coefficient β_2 is a function of a, i.e.

$$
\beta_2(a) = \gamma_0 + \gamma_1 a, \tag{30}
$$

where γ are the coefficients of this particular model. Inserting Equation 30 into 29 gives

$$
y = \beta_0 + \beta_1 a + \gamma_0 b + \gamma_1 ab, \tag{31}
$$

so that we now have the interaction term ab with associated coefficient γ_1.

Following the model equation notation we introduced in Section 4.1, we introduce a new interaction parameter $\texttt{a:b}$, to obtain $\texttt{y} \sim \texttt{a + b + a:b} \equiv \texttt{a * b}$. We have introduced two new model notations here: the : symbol represents an interaction, and * corresponds to two predictors added together with their interaction (McCullagh and Nelder, 2019).

In this study specifically, normally one would be interested in the individual effects of $\texttt{lsc}$ or $\texttt{greg}$ on the storm footprint. However, LSCs are specifically calculated in the West Atlantic. Thus, if LSCs are strong while the storm generates in the East Atlantic ($\texttt{greg} = 0$), we do not expect LSCs to have as much of an influence on the storm footprint compared

to the situation where storms instead generate in the West (`greg = 1`). As we will see in our final statistical model, we attempt to circumvent this problem by including an interaction between `lsc` and `greg` to account for this combined influence. The same logic can be applied to the predictor `mireg`. A strong jet should contribute substantially to the storm footprint, as does the fact it intensifies in the East. We recall from previous chapters that a strong jet during the cyclone's intensification in the East can lead to extremely high footprints. Thus, we represent this combined effect using interaction terms between `mireg` and `jet, pv, eady, nao` and `b`.

4.3   Statistical model structures

Building from the previous sections, we will now define the set of statistical models to explore in the following sections. We begin with simpler models and gradually build them in complexity. The simplest model structure will be one that does not include any explicit information about regional development, and uses the equation[4]

$$\texttt{ssi} \sim \texttt{lsc + sstg + jet + eady + pv + nao + b}. \tag{32}$$

Equation 32 is first applied to all storms in the MPI-ESM-LR and ERA-20C data sets, and assumes that the variance in the storm footprint can be adequately described without information of its regional development. Name this statistical model M1.

Let us now introduce the regional development of storms as an important factor. We subset data in three groups: those that generate in the West Atlantic ($\texttt{greg} = 1$, model M2), those that intensify in the East Atlantic ($\texttt{mireg} = 1$, model M3), and those that satisfy both of these conditions ($\texttt{greg} = 1$ and $\texttt{mireg} = 1$, model M4). Models M2 through M4 can further be expressed in terms of M1 as `greg`∗M1, `mireg`∗M1, and `greg`∗`mireg`∗M1, respectively. Model M5 includes information about the genesis and intensification regions of the storms in different manner, and utilizes the following equation

$$\texttt{ssi} \sim \texttt{greg + mireg + lsc + sstg + jet + eady + pv + nao + b}. \tag{33}$$

This equation is similar to the previous equation, except that `greg` and `mireg` are now additively included. It is now applied to *all* storms; there is no subsetting involved here. Lastly, model M6 additionally includes these two new predictors, but instead integrates them as interactive predictors with the following equation

$$\texttt{ssi} \sim \texttt{greg * (lsc + sstg) + mireg * (jet + eady + pv + nao + b)}, \tag{34}$$

and is applied to all storms as well.

Table 7 summarizes all six of the aforementioned models, including the various subsets of data, as well as the formulae that have been applied. Since we standardize the predictors, those with higher β estimates better describe the variance of the footprint compared to predictors with lower estimates. The goal is to find a model with specific predictors and storms such that its explained variance is maximized, and to identify which of these predictors

---

[4]We note that `nao` will be replaced by a binary predictor later on. Nonetheless, the structure of the models remain the same.

emerge with the highest estimates of the β parameters along with p-values which satisfy the threshold of $p < 0.05$. From this table, we can see that subsetting significantly reduces the number of storms considered, most notably M4. However, this trade-off allows us to better understand the regional development of storms while still retaining a parsimonious model.

model	formula	subset	N (MPI-ESM-LR)	N (ERA-20C)
M1	Eq. 32	none	3427	966
M2	Eq. 32	greg = 1	912	287
M3	Eq. 32	mireg = 1	2049	541
M4	Eq. 32	greg = 1 & mireg = 1	630	179
M5	Eq. 33	none	3427	966
M6	Eq. 34	none	3427	966

Table 7: Model setups. N is the number of storms included in the data set.

It is important to note that we assumed a Gamma GLM with a log-link would be the most appropriate for our data. However, other models such as a linear model (i.e. Gaussian family, identity link) could be used. When applied here, they generally produced models with a number of similarly significant predictors, but lower R^2 values. In addition, the interpretation of numerical changes in our response is different, as there are some nuances. In the Gamma model, we compute how the $\log(\mathbb{E}[\text{ssi}])$ relates to different predictors. For instance, we compute a change of $\Delta \log(\mathbb{E}[\text{ssi}]) = 1.0$. This represents an e-fold increase in the expected value of the footprint. In the case of a linear model, we instead compute $\Delta \mathbb{E}[\log(\text{ssi})] = 1.0$, which represents an increase in the expected value of the *log*-footprint of 1.0. Although a small distinction, the former construction is more intuitive as it works in terms of absolute footprints, not those which are log-transformed.

4.4 Model diagnostics

Multicollinearity

Multicollinearity refers to the case where multiple predictors of a GLM are highly linearly related, such that the values of individual regression coefficients can become more difficult to estimate accurately. In order to account for this, one can compute the Variance Inflation Factor (VIF) of each predictor in the model (Dobson and Barnett, 2008). The equation for the ith predictor's VIF is

$$\text{VIF}_i = (1 - R_i^2)^{-1} \tag{35}$$

where R_i^2 is the coefficient of determination of the regression equation for the ith predictor with all other predictors (using ordinary least squares regression). The coefficient of determination is essentially the total variance of the data explained by a model, and is defined by

$$R^2 = 1 - \frac{SS_{\text{res}}}{SS_{\text{tot}}}, \tag{36}$$

where $SS_{\text{res}} = \sum_j (y_j - f_j)^2 = \sum_j e_j^2$ is the sum of squares of residuals e_j, and $SS_{\text{tot}} = \sum_j (y_j - \bar{y})$ is the total sum of squares. Here, f_j refers to the fitted values compared to the observed values y_j with a mean $\bar{y}$. A high R_i^2 would indicate that the predictor is highly linearly dependent on all other predictors. A rule of thumb is to remove predictors with a

VIF higher than 10, and a more strict threshold of 5 is sometimes used as well (Montgomery et al., 2012). Here, we use the threshold of 5.

Akaike Information Criterion and Stepwise Model Selection

A useful model diagnostic developed by Akaike (1974) is the Akaike Information Criterion (AIC), defined as

$$AIC = 2k - 2\ln l(\hat{\theta}),\tag{37}$$

where k is the number of estimated parameters in the model, $l(\hat{\theta})$ is the maximum value of the log-likelihood function of the model, and $\hat{\theta}$ is the MLE estimate of θ (see Section 4.1). Models with minimized AIC values are preferred, thus the AIC penalizes models with higher k. The AIC conceptually represents the amount of information lost in a given model. However, it is not a useful quantity on its own, in the sense that it does not explain the absolute strength of the model. To understand the significance of the AIC value itself, we must compare it between nested models[5]. The probability that model A minimizes information loss compared to model B is proportional to $\exp(-\frac{1}{2}\Delta AIC)$ (Burnham and Anderson, 2002), where $\Delta AIC = AIC_A - AIC_B$. For example, if $AIC_A = 1000$ and $AIC_B = 1001$, then AIC_B is 0.61 as likely to minimize information loss as AIC_A.

In this study, the primary purpose of the AIC is to assist in backwards stepwise model selection. Backwards stepwise model selection refers the process by which we iteratively remove predictors from a model, comparing AICs along the way. The end result is a model with reduced complexity while still retaining the most important information. A detailed example of this process is shown in Section 4.6. In addition, forwards stepwise model selection is possible, and is particularly useful in models with a large number of predictors which would otherwise make it computationally challenging to begin with the full model. However, as noted in Field (2005, p. 161), forward stepwise is more likely to exclude predictors that help describe the response because of suppressor effects, i.e. predictors which are only significant when another is held constant. The AIC is sometimes known to choose too complex models, a problem which is sometimes circumvented by using the Bayesian Information Criterion (BIC) instead, which is just Equation 37 but the term $2k$ is replaced by $2\ln(n)k$, where n is the number of observations. However, we choose the AIC for this study as the BIC combined with backwards stepwise model selection was found to be too restrictive, in the sense that numerous important parameters were being discarded.

Assessing outliers

Outliers in the data can significantly influence the fit of a GLM, such that the removal of them can noticeably change the estimated parameters. One useful metric to define this effect of the ith datum is called Cook's Distance (or Cook's statistic), D_i, defined as

$$D_i = \frac{r_i^2 h_i}{p(1 - h_i)},\tag{38}$$

where h_i represents the leverage of the datum, $r_i = (\hat{e}_i/\hat{\sigma})(1 - h_i)^{-1/2}$ is the standardized

---

[5] "Nested" refers to models which are essentially subsets of a larger model. For example, `y ~ a + b` is nested in the larger model of `y ~ a + b + c`.

residual (for estimated residual $\hat{e}_i$ and variance $\hat{\sigma}$), and p is the number of parameters (Dobson and Barnett, 2008). The leverage can be thought of as the degree in which the ith measured value influences the ith fitted value and is explained with more mathematical detail in Cardinali (2013). We will show later in Section 4.6 how we can utilize this metric as a diagnostic for potentially problematic outliers.

Coefficient of variation

The performance of the model can be represented by another form of the coefficient of determination (Equation 36). This is calculated as

$$R^2 = 1 - \frac{\text{Residual Deviance}}{\text{Null Deviance}}, \tag{39}$$

where the deviance is the sum of squares of deviance residuals (Wood, 2017). More specifically, the null deviance relates to the fit for a model with only an intercept term, and the residual deviance for the model we construct. Like we saw with residuals in the ordinary least squares case (Equation 36), deviance residuals are a more general version that can be applied to any GLM. R^2 is not the be-all and end-all diagnostic as it is usually employed in some linear models; it is more useful in diagnosing predictive rather than explanatory models. Here, it is used as a sense check to ensure that a sizable and significant portion of the variance is being explained.

4.5   Relationships between the footprint and predictors

We first explore the general relationships that can be found between the response variable and its predictors. This provides a sense of which variables show potential in explaining the variance of the footprint. It is often the case that one cannot find simple relationships between the response variable and predicted variable until one or the other variables is transformed in some way, thus we first explore a log-transformation of the footprint. Then, we use correlation matrices to highlight key relationships between the footprint and the continuous predictors, as well as any potential relationships between the predictors. Lastly, categorical variables associated with the NAO and regions of cyclogenesis or intensification are explored.

4.5.1   Transformed data and correlation matrices

If we were to plot `ssi` against `jet` in a scatter plot (Figure 32a), we would not find a clear relationship between the two variables. However, if we instead plot the log-transformed footprint against the jet one sees a slightly clearer linear relationship emerge (Figure 32b).

Log-transformation of data is a common way to take data that is approximately exponentially distributed and transform it into a distribution that becomes more similar to the normal distribution in terms of its structure and symmetry (McCullagh and Nelder, 2019). This transformation of the distribution can be seen in Figure 33. Although the construction of a GLM need not require the response variable to be normal, our link function still log-transforms the expected value of the response.
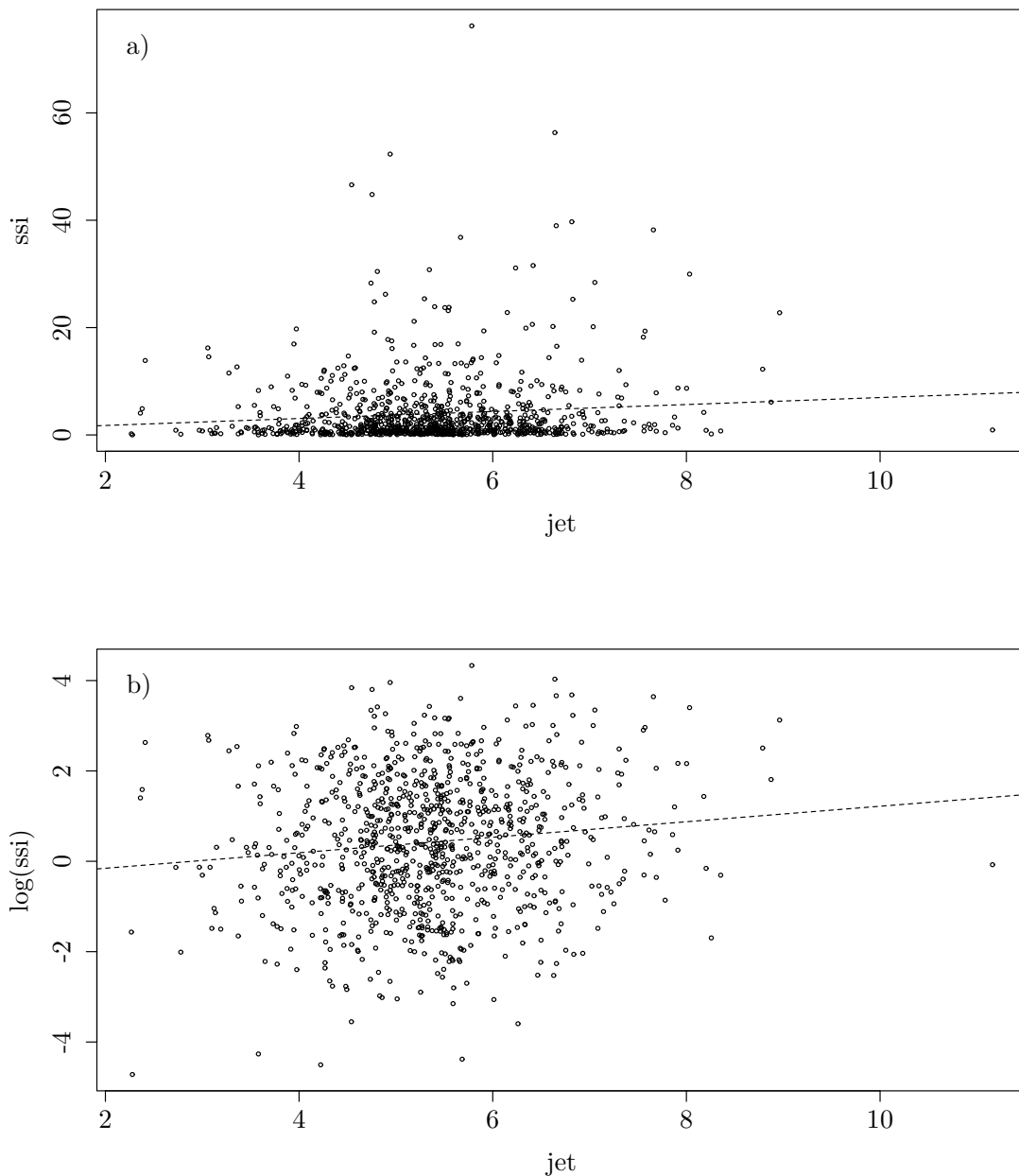
Figure 32: Scatterplot of a) `ssi` against `jet` and b) log-transformed data. The dashed lines represent the linear fit of the footprint against the jet. Data is ERA-20C.

Let us extend this to all the continuous variables, and construct a matrix of correlations between the log transformed footprint (lg.ssi) and each variable, displayed in Figure 34. The first column of each matrix displays the correlation of the log-footprint against all the other variables. In both MPI-ESM-LR and ERA-20C, it is most highly correlated with `jet` and `eady`, with lower correlations amongst the rest. It is clear that the log of the footprint cannot be explained by any one of these predictors alone in a purely linear fashion.

Between the individual predictors, the strongest correlations can be seen between `jet` and `eady`, reaching 0.62 and 0.61 in the MPI-ESM-LR and ERA-20C, respectively. The `jet` predictor shows much lower magnitude correlations with `pv` (0.26 / 0.26) and `b` (0.32 / 0.38). The high correlations between `jet` and `eady` or `pv` were to be expected: in Section 3.5 it was found that jet anomaly composites closely resembled composites of EGRs, and that PV anomalies were usually higher near the cyclone core as well. The higher correlation with `b` likely indicates that strong jets are primarily associated with strong zonal winds, which is often the case in the extra-tropical North Atlantic. However, it is surprising that the bearing is weakly correlated with `nao` (0.09 / 0.12), as it was assumed that a more positive NAO

81
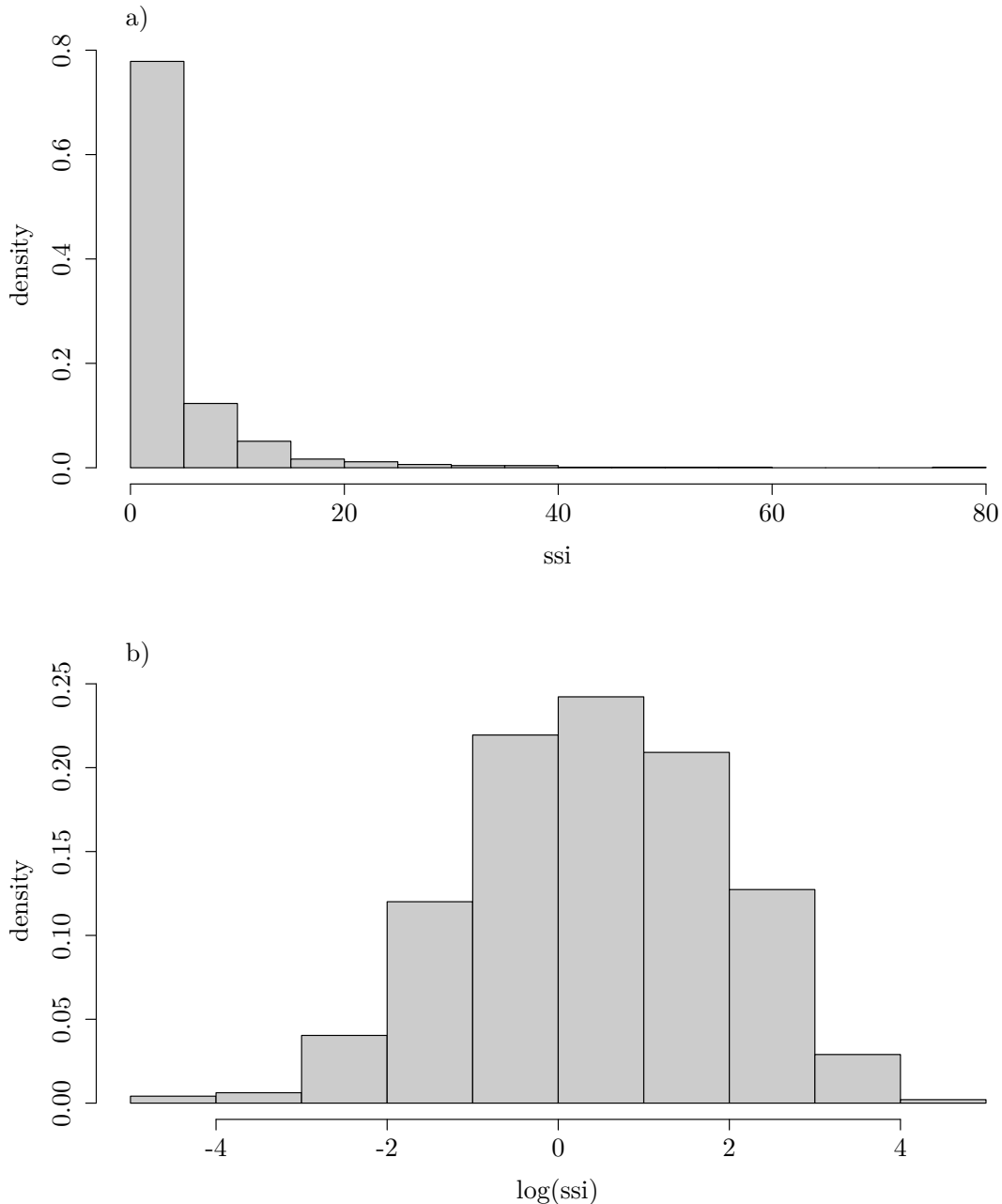
Figure 33: Comparison of histograms for a) untransformed and b) log-transformed `ssi`. Data is ERA-20C.

phase is associated with storms traveling in an easterly direction. Finally, both thermal gradients, `lsc` and `sstg`, show high correlations between each other (0.42 / 0.60). Stronger SST gradients near the coastline may increase the likelihood that surface air temperature contrasts across the US East Coast are further increased through surface heat fluxes. In all of the aforementioned cases of high correlations between predictors, this increases the likelihood that their VIFs will be higher such that they may need to be replaced.

The significantly low correlation of the log-footprint with the `nao` (0.11 / 0.08) is surprising, and the following section explores how it may be related to the NAO in a non-continuous manner. Similarly, the low correlations with `lsc` (0.11 / 0.09) and `sstg` (0.06 / 0.10) will be expanded upon in the section thereafter, with the use of the regional predictor `greg`.

4.5.2 Creating a categorical NAO predictor

The histograms in Figure 35 display the frequency of different NAO strengths. On average, storms intensify during a neutral phase of the NAO (centered near `nao = 0`). In MPI-

MPI-ESM-LR
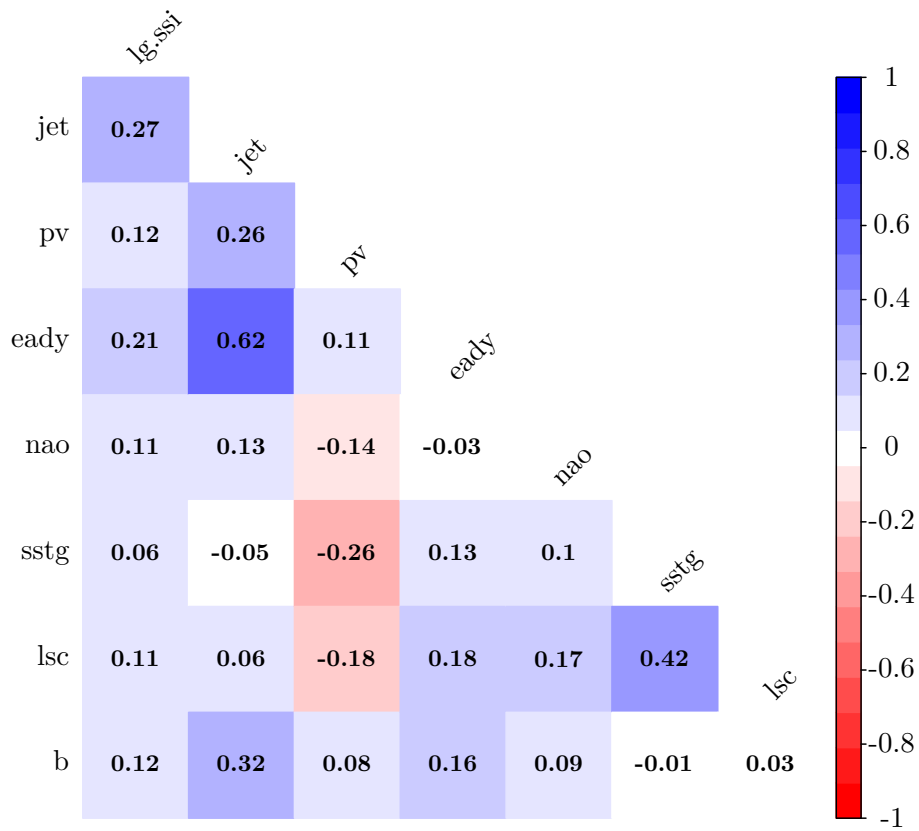
ERA-20C
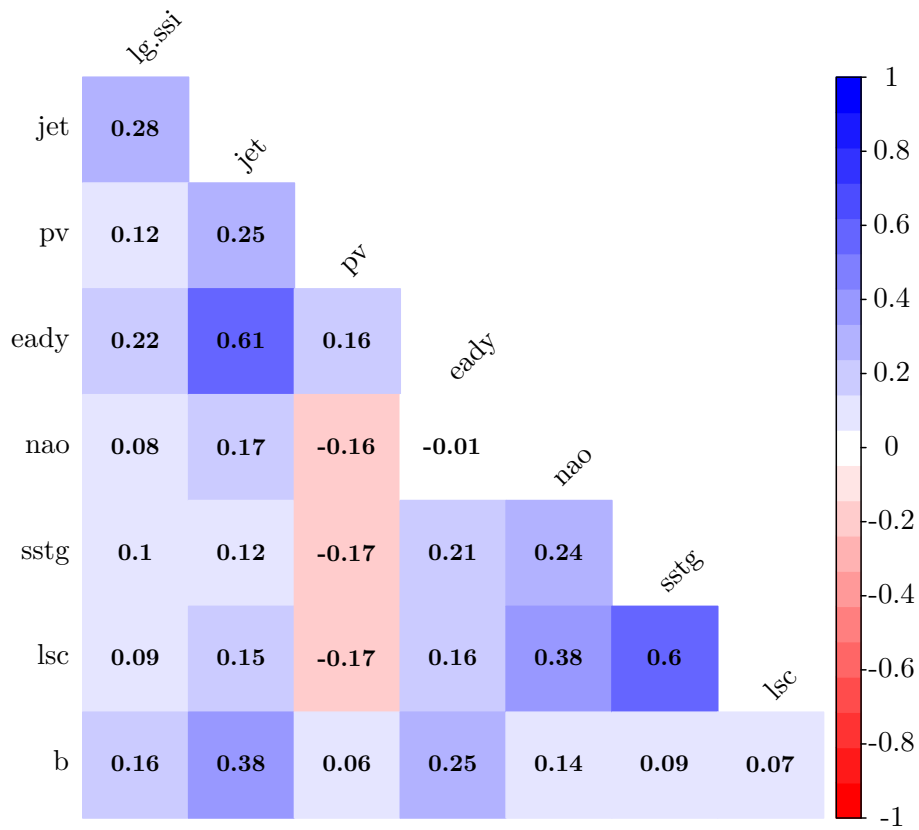
Figure 34: Correlation matrices of the response variable and predictors for (top) model MPI-ESM-LR data, and (bottom) ERA-20C data. All correlations are significant to the $p < 0.05$ level using a t-test.

ESM-LR and ERA-20C, there are 60% / 66% more storms that intensify during a positive compared to a negative NAO phase.
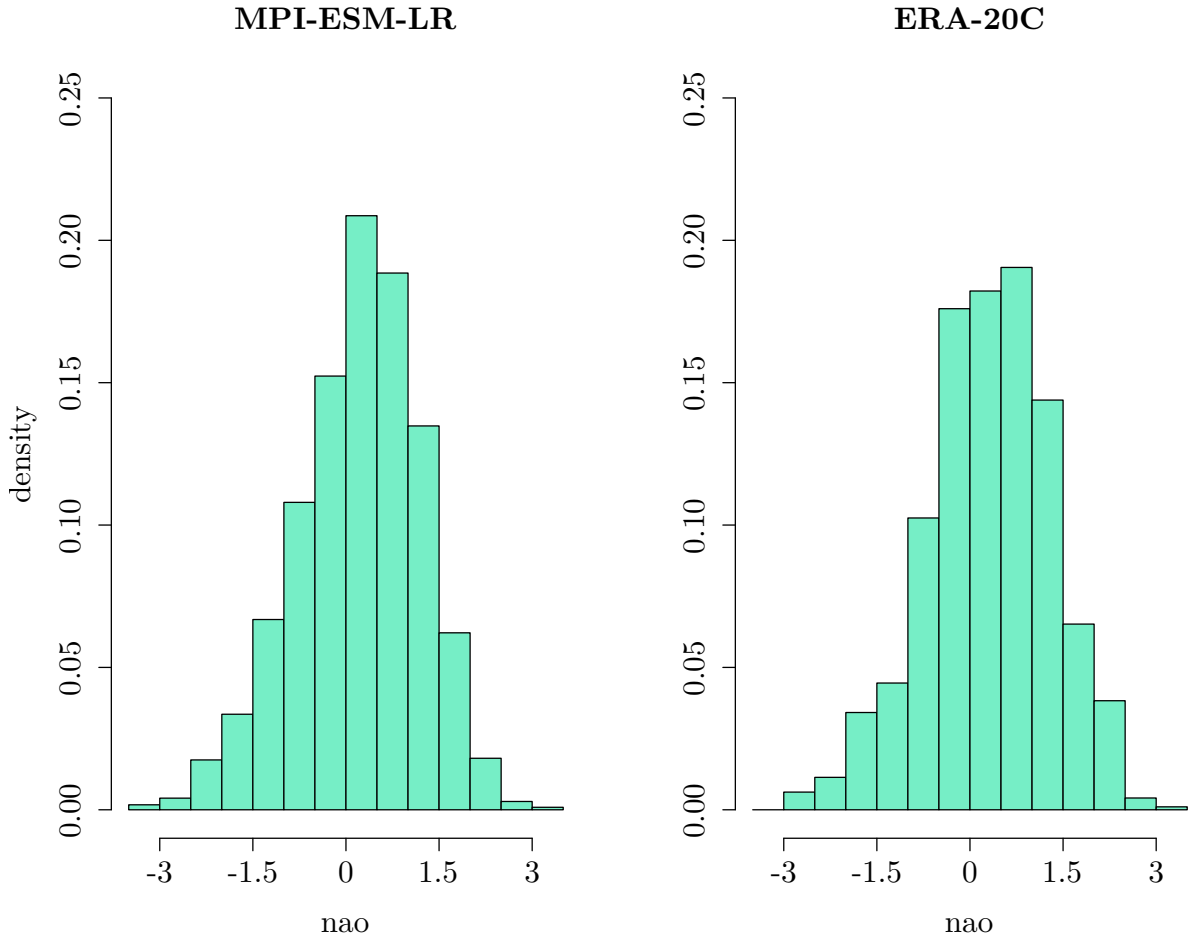
MPI-ESM-LR   **ERA-20C**

Figure 35: Histograms of NAO values for all storms at their cyclone maximum intensification phase for MPI-ESM-LR (left) and ERA-20C (right) data.

However, this continuous NAO predictor was found to provide inconclusive results in the statistical models to follow (not shown). We thus approach this problem from a different perspective. The NAO can alternatively be re-defined as a categorical index to represent "weak", "neutral", or "strong" phases (e.g. Serreze et al. (1997), Pinto et al. (2009), Nissen et al. (2014)). These phases are defined by $\mathtt{nao} \leq -1.5$, $-1.5 < \mathtt{nao} < 1.5$, and $\mathtt{nao} \geq 1.5$, respectively. Table 8 shows that there are substantial increases in the average value of storm footprints during strong NAO phases compared to weak and neutral phases. The results are consistent between both sets of data as well. Further, comparing strong versus not-strong (i.e. $\mathtt{nao} < 1.5$) shows a similar signal. Thus, this motivates the use of a binary predictor, which we call $\mathtt{naop}$, to indicate whether the NAO is in a strongly positive phase ($\mathtt{naop} = 1$) or otherwise ($\mathtt{naop} = 0$).

Data Set	Strong — Weak	Strong — Neutral	Strong — Not Strong
MPI-ESM-LR	0.61	0.50	0.51
ERA-20C	0.76	0.48	0.49

Table 8: Differences in average log($\mathtt{ssi}$) for storms intensifying during strong NAO phases versus weak phases (left column), neutral phases (middle column), and non-strong phases (right column). All differences are significant to the $p < 0.05$ level using a Welch two-sided t-test.

4.5.3 Regional predictors

We make the assumption that storms which generate in the west should produce higher footprints in Europe. In order to test whether or not `greg` can systematically increase the average value of the storm log-footprint and/or its slope, we can first regress log(`ssi`) onto another predictor individually, for example `lsc` or `sstg`. These two predictors are expected to play a more important role in a storm footprint given that it generates in the west. This regression is repeated for storms which generate in the west and otherwise. The results are shown in Figure 36.
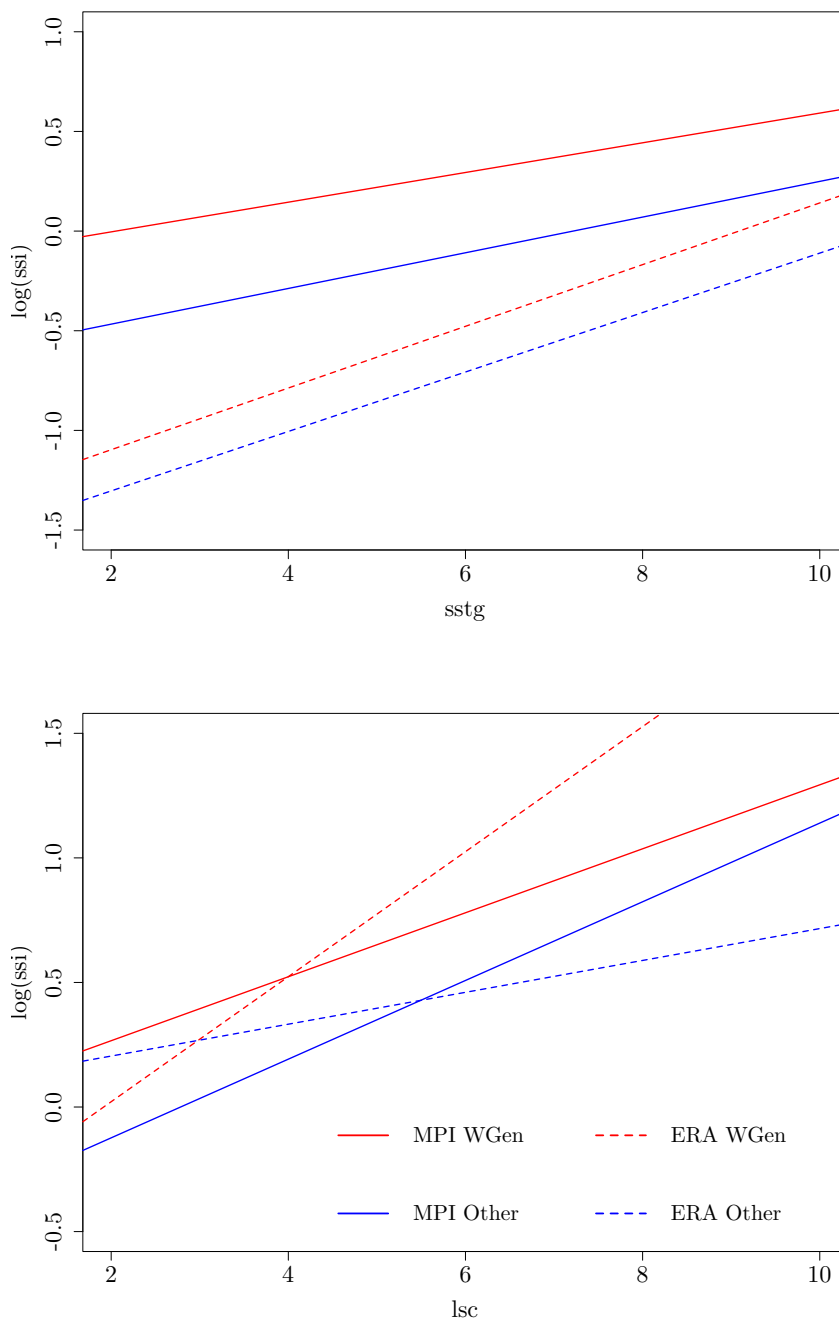
Figure 36: Regressions of log(`ssi`) against `sstg` (top) and `lsc` (bottom), for `greg` = 1 (red lines) and `greg` = 0 (blue lines). Both the MPI-ESM-LR (solid lines) and ERA-20C (dashed lines) are compared.

In both data sets, a systematic increase in the average value of the log-footprint's fit is seen for western-generated storm systems against increasing values of `sstg`, but no change in the slope of the log-footprint is clear. Against `lsc`, we see slightly different behaviour depending on the data set. The ERA-20C data sees a stark increase in its slope and no

significant change in the average footprint value. For the MPI-ESM-LR data, the average log-footprint is higher for western-generated storms, but there is a slight reduction in the slope. Regardless of the disagreements here, we still observe some evidence that `greg` can systematically affect the average footprint either in the slope or the average value.

4.6   Model results

In the sections to follow, tabulated results of the models' predictor estimates (β), standard errors, and p-values will be assessed and compared amongst one another. Each model will undergo stepwise AIC predictor selection, multi-collinearity testing, and residual verification. For brevity, these will only be explored in detail for M1. Lastly, the goodness of fit of each model is quantified using the R^2 from Equation 39. As a rule of thumb, useful predictors are those which contain high estimates and low p-values relative to other predictors in the table. We are additionally interested in consistency across the data sets, i.e. predictors which are significant to $p < 0.05$ in both MPI-ESM-LR and ERA-20C.

M1: All North Atlantic storms

Before we continue with the results of the model, one must first consider the degree of multi-collinearity that is apparent between the predictors, shown in Table 9. The highest collinearity occurs for `jet`, `eady`, `lsc` and `sstg`, which was to be expected as some of these were highly correlated (Figure 34). In general, if a predictor's VIF does not exceed a value of 5, the predictor is included in the model; thus we retain all of them here.

Predictor	`lsc`	`sstg`	`jet`	`eady`	`pv`	`naop`	`b`
VIF	1.64	1.62	1.87	1.66	1.14	1.13	1.18

Table 9: VIFs for the predictors considered in M1 (ERA-20C).

Then, we work through an example of backwards stepwise AIC to select a more parsimonious model where possible. Table 10 and Table 11 demonstrate how this is carried out for the ERA-20C data in a backwards fashion (this was applied to MPI-ESM-LR data, but is not shown here). Let Δ_0 be changes in the model AIC if we remove a predictor with respect to the base model. In the first step, Table 10, we find a base model AIC of 4358.0 including all predictors (this is "(None)"). With the removal of `lsc`, we see a change of $\Delta_0 = -1.9$. Thus we discard `lsc`, and repeat the process iteratively. We find the predictor with the lowest Δ_0, and if it is less than -1.0, we remove it. In the final step, Table 11, we have the option to remove `eady` for an AIC improvement of -1.0, and it is thus removed. This step is denoted as the final step, because to remove any more predictors from now would result either in weakly negative or positive Δ_0. It is crucial to note that the modeler need not use $\Delta_0 \geq -1.0$ as a strict threshold. In exploratory statistical modeling, one is free to include or exclude specific predictors as they see fit, and there is a degree of subjectivity in stepwise AIC model selection.

Predictor to remove	`lsc`	`b`	`naop`	`eady`	(None)	`pv`	`sstg`	`jet`
AIC	4355.8	4355.8	4356.4	4357.0	4357.7	4358.4	4359.8	4369.8
Δ_0	-1.9	-1.9	-1.3	-0.7	—	+0.7	+2.1	+12.1

Table 10: First Step of Stepwise AIC Selection for M1 (ERA-20C).

Predictor to remove	`eady`	(None)	`pv`	`sstg`	`jet`
AIC	4352.2	4353.2	4356.6	4357.9	4370.8
Δ_0	-1.0	—	+0.4	+4.3	+17.2

Table 11: Last Step of Stepwise AIC Selection for M1 (ERA-20C).

Backwards stepwise AIC model selection for ERA-20C, M1. Tables 10 and 11 are the first and last steps of the procedure, respectively. The procedure took 4 steps total. AIC values for corresponding models excluding certain variables are shown on the first row, where higher AIC values are placed to the right of "(None)", and lower ones to the left. "(None)" refers to the model without removing any predictors, and Δ_0 is the change in AIC of the model when removing that predictor compared to the current model with all predictors. Variables which do not show in the bottom table are those which were discarded in a previous step.

The validity of this model for these two data sets is elucidated by diagnosing their respective residual behaviours. The following diagnostics are all related to the ERA-20C data. Figure 37 illustrates how the residuals of M1 applied to ERA-20C behave. To begin with, we focus our attention on Figure 37a. The scatterplot residuals against the linear predictors show no clear relationship. The Q-Q plot in Figure 37b plots the quantiles of the standardized deviance residuals against theoretical Gaussian quantiles. It is reminiscent of a right-skewed distribution, showing a higher density of points at extremely small and large values compared to Gaussian distribution. This is expected, and the assumptions of a Gamma GLM do not demand for residuals to be normally distributed. Figure 37c plots the Cook's distance against the leverage (see Equation 38) with the exact cases shown in Figure 37d. Few points contain a high leverage, and those that do would not heavily influence the model were they to be removed and the regression repeated. The primary purpose of these diagnostics is to be cautious for any significant linear or non-linear trends present in the data that have not been accounted for, and for the influence of outliers. For future models we do not show diagnostic plots unless a problem was found.

Finally, we can move on to the tabulated results which are displayed in Table 12. For each predictor, we have a column "Estimate" which refers to the β estimate, along with its "Standard error" and associated "p-value". This is split into two major columns, one for MPI-ESM-LR and one for ERA-20C. In the description of results to follow, we will first look at MPI-ESM-LR results, followed by ERA-20C, and then a comparison between the two.

For MPI-ESM-LR, all of the predictors are significant to the $p < 0.05$ level. In terms of their predictor estimates, the strongest predictors are `naop` and `jet`. With $R^2 = 0.12$, the model only describes some of the variance in the storm footprint, although it is significant

a)

b)

c)

d)
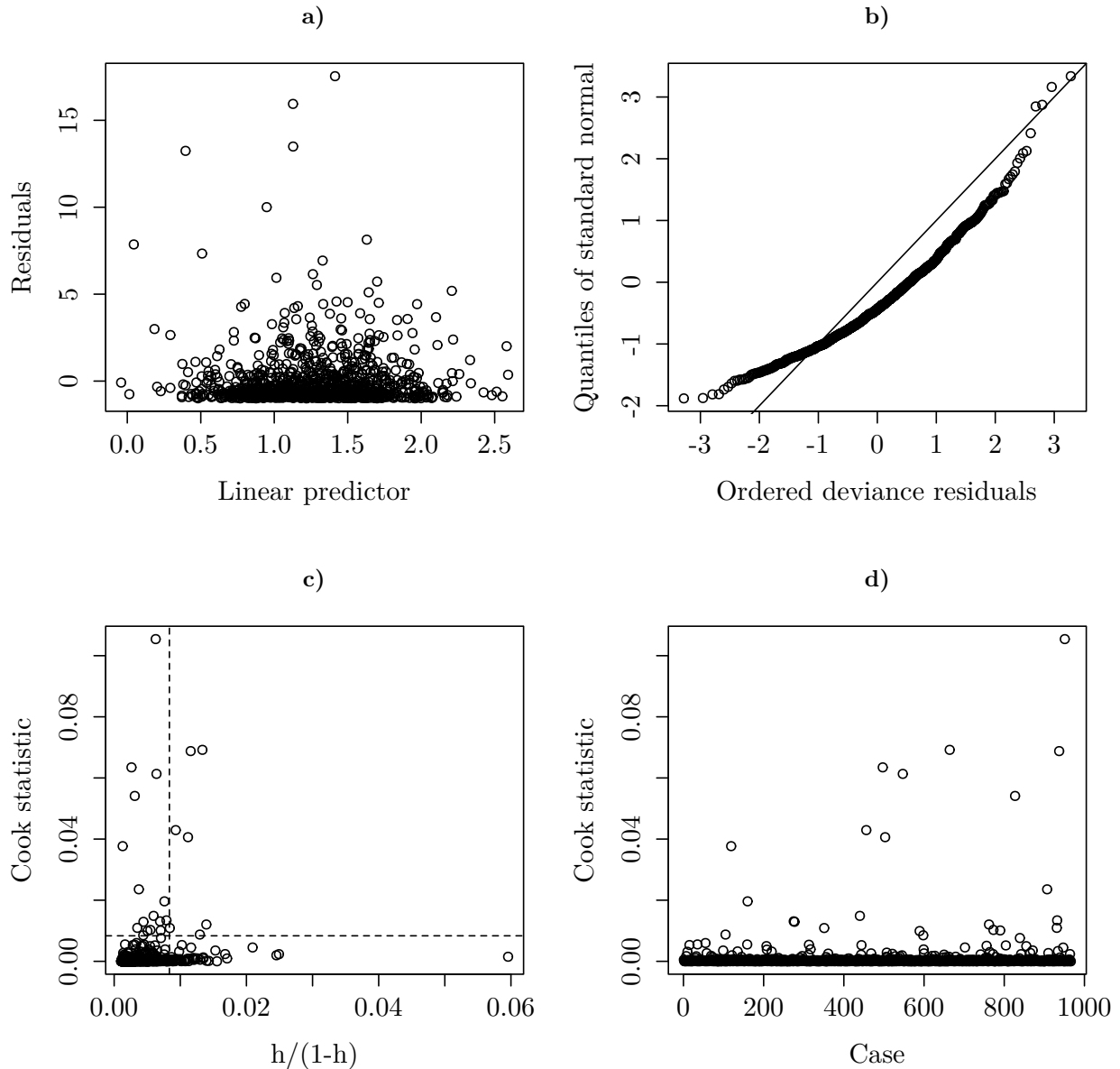
Figure 37: Diagnostic plots for M1, ERA-20C. a) Residuals plotted against the fitted values. b) A Q-Q plot of the deviance residuals versus theoretical normal quantiles. c) The Cook's distance D against the normalized leverage $h/(1-h)$. Here, the points above the horizontal dashed line highly influence the model. Those to the right of the vertical dashed line have high leverage compared to the residual's variance. d) Cook's distance for each case.

to $p < 0.05$ (tested against the null hypothesis that there is no slope). In ERA-20C, only `sstg`, `jet` and `pv` are included, of which the former two are significant to $p < 0.05$.

The results of M1 show that, without any explicit information about geographical locations, jet stream and potential vorticity anomalies at the maximum intensification phase explain the highest amount of a footprint's variance. Moreover, in MPI-ESM-LR a strongly positive NAO phase is beneficial, and there is a lesser (but still important) role of EGRs. The importance of thermal gradients is clear in both data sets, but with different predictors; MPI-ESM-LR is more influenced by land-sea contrasts and ERA-20C by SST gradients. We note that there are a number of European systems with trajectories far away from RW and RE, e.g. storms which generate and intensify in Arctic or sub-tropical regions, and thus systems where different processes could dominate their growth. This could explain why R^2 values are relatively low, as it is missing these key processes such as Arctic or sub-tropical temperature gradients, sea ice, or even orography. These processes were not included in the model as they concern only a small subset of the studied storm systems.

	MPI-ESM-LR			ERA-20C		
Predictor	*Estimate*	*Standard error*	*p-value*	*Estimate*	*Standard error*	*p-value*
Intercept	-2.55	0.237	$< 10^{-10}$	-3.23	0.803	$< 10^{-4}$
lsc	0.161	0.0281	$< 10^{-7}$	—	—	—
sstg	—	—	—	0.154	0.0537	0.00431
jet	0.292	0.0350	$< 10^{-10}$	0.341	0.0547	$< 10^{-9}$
eady	0.0730	0.0346	0.0348	—	—	—
pv	0.146	0.0282	$< 10^{-6}$	0.0835	0.0551	0.130
naop	0.336	0.0978	$< 10^{-4}$	—	—	—

Table 12: M1 summary. $R^2 = 0.12$ and 0.09 for MPI-ESM-LR and ERA-20C, respectively. Each predictor's estimate (i.e. β), its standard error, and its p-value are displayed.

M2: Storms that generate in the West

While our previous model was simple, unconstrained, and supplied with ample data, we now check to see how constraining our storm sets leads to more robust results (i.e. more significant predictors) or different statistical inference. As we know high footprint storms typically generate in the West Atlantic, we want to see if restricting our data to western-generated storms will build upon the previous model. This model addresses storms that explicitly generate in RW, with the subset `greg = 1`. We use the formula shown in Equation 32.

For MPI-ESM-LR, with all but one predictor included by stepwise AIC (Table 13). There is some similarity to the results of M1: `jet`, `naop`, `lsc`, and `pv` remain strong. However, `b` also appears as a strong, significant predictor. Overall, subsetting historical data in this way marginally changes the result of the model compared to M1 by including a new predictor at the expense of another (`eady`).

	MPI-ESM-LR			ERA-20C		
Predictor	*Estimate*	*Standard error*	*p-value*	*Estimate*	*Standard error*	*p-value*
Intercept	-2.70	0.382	$< 10^{-10}$	-1.32	0.692	0.0576
lsc	0.144	0.0462	0.00196	—	—	—
jet	0.394	0.0526	$< 10^{-10}$	0.252	0.121	0.0385
eady	—	—	—	0.187	0.106	0.0780
pv	0.142	0.0501	0.00469	—	—	—
naop	0.360	0.154	0.0196	0.326	0.270	0.228
b	0.158	0.0564	0.00513	-0.191	0.122	0.118

Table 13: M2 summary. $R^2 = 0.15$ and 0.09 for MPI-ESM-LR and ERA-20C, respectively.

For ERA-20C, in terms of predictors, only the four predictors `jet`, `eady`, `naop` and `b` are included. More importantly, compared to M1, the predictor `naop` plays a much larger role in explaining the variance of storm footprints. What was once an unimportant predictor in M1 is nearly as influential as `jet` in M2, but is not significant to p < 0.05. Surprisingly, `lsc` and `sstg` do not emerge as important predictors, despite storms necessarily generating in RW. The bearing predictor unexpectedly emerges with a negative parameter estimate; it

is unclear how this came to be, but it is not significant to p < 0.05 and contains a high standard error.

Altogether we see slight changes in the interpretation of predictors and their effect on storm footprints compared to M1, except for the potential role of a storm's direction of travel. In MPI-ESM-LR, the storm bearing emerges as a strong and significant predictor. In ERA-20C, the strongly positive NAO emerges as a powerful predictor instead (although it is not significant). One could collectively interpret this by considering that storms generating in RW need to be funneled into the European region later in their lifetime, regardless of their strength. As we saw in Section 2.7, strong North Atlantic systems which generate in RW are likely to remain along the US East Coast, and only a small subset of them will travel directly into Europe; a strongly positive NAO phase can assist with this. In M1 this was not as necessary, as the entire set of data included storms which generate in the East Atlantic and are already likely to enter Europe. However, despite subsetting storms which explicitly generate in RW, thermal gradient predictors did not emerge as more significant. In fact SST gradients were discarded entirely in ERA-20C. The most glaring drawback of this style of subsetting is the stark reduction in data, particularly for ERA-20C, which already has much less data to use compared to MPI-ESM-LR. In ERA-20C, only 29.7% of storms were included. This will significantly affect the robustness of any relationships between the storm footprint and the predictors.

M3: Storms that intensify in the East

This motivation for this model is similar to M2, except we subset storms into those that experience maximum intensification in RE with the condition `mireg = 1`. It uses the formula displayed in Equation 32. The aim is to see if constraining our data to storms intensifying specifically near Europe will provide more insight.

In MPI-ESM-LR, all predictors except `b` are chosen by stepwise selection and the majority of them are significant to p < 0.05 (Table 14). The predictors `jet`, `naop`, and `lsc`, and `pv` remain strong, like in M2. Moreover, `eady` and `sstg` have now emerged as relevant predictors.

	MPI-ESM-LR			ERA-20C		
Predictor	*Estimate*	*Standard error*	*p-value*	*Estimate*	*Standard error*	*p-value*
Intercept	-4.18	0.427	$< 10^{-10}$	-2.86	0.570	$< 10^{-6}$
lsc	0.188	0.0375	$< 10^{-6}$	—	—	—
sstg	0.0556	0.0372	0.135	—	—	—
jet	0.415	0.0462	$< 10^{-10}$	0.348	0.0806	$< 10^{-4}$
eady	0.107	0.0457	0.0189	0.197	0.0779	0.0117
pv	0.163	0.0374	$< 10^{-4}$	0.0909	0.0623	0.145
naop	0.302	0.132	0.0218	—	—	—

Table 14: M3 summary. $R^2 = 0.17$ and 0.13 for MPI-ESM-LR and ERA-20C, respectively.

The ERA-20C results are fairly different to previous models, where intensification quantities like `eady` and `pv` have a stronger influence with respect to `jet` (although `pv` is not significant to p < 0.05). The role of thermal gradients remains to be elusive as they are not included at all, along with the predictors `naop` and `b`. It is possible that storms which

intensify in RE are likely to drift into Europe with an idealised trajectory, so that there is less of a need for a strongly positive NAO.

In general, both of these data sets agree that jet streams, EGRs, and PV850 anomalies are the predominant factors affecting the storm footprint for those which necessarily intensify in RE. The clearest disagreement between the dataset lies in the role of thermal gradients, which seem to be more significant in the MPI-ESM-LR for land-sea contrasts specifically.

M4: Storms generating in the West *and* intensifying in the East

We now wish to see if heavily constraining the regional development of storms leads to a more robust and detailed model. This is done as we previously found in Section 2.8 that storms specifically generating and intensifying in RW and RE, respectively, were associated with high footprint storms. Thus this model construction is a combination of the previous two models with the subset `greg = 1` *and* `mireg = 1`, i.e. storms are subset by those which generate in RW and intensify in RE. It is the last model which uses the formula from Equation 32.

As with a number of previous models, this model continues the trend of `jet`, `naop`, and `lsc` with high estimates, this time along with `pv` and `b` (Table 15). Like M2, both `eady` and `sstg` were not included in the model. However, `naop` and `b` are not significant to p < 0.05.

	MPI-ESM-LR			ERA-20C		
Predictor	*Estimate*	*Standard error*	*p-value*	*Estimate*	*Standard error*	*p-value*
Intercept	-3.50	0.476	$< 10^{-10}$	-3.30	0.861	$< 10^{-4}$
lsc	0.188	0.0547	0.000624	—	—	—
sstg	—	—	—	—	—	—
jet	0.498	0.0663	$< 10^{-10}$	0.274	0.119	0.0229
eady	—	—	—	0.327	0.109	0.00301
pv	0.147	0.0612	0.0166	0.0915	0.0999	0.361
naop	0.330	0.194	0.0893	—	—	—
b	0.142	0.0778	0.0681	—	—	—

Table 15: M4 summary. $R^2 = 0.18$ and 0.15 for MPI-ESM-LR and ERA-20C, respectively.

For the ERA-20C results, both `jet` and `eady` are strong and significant. This is the first model where `eady` emerges as a stronger predictor compared to `jet`. Moreover, `pv` is included in the model, but is relatively weaker and not significant. As with M2, the stark reduction in data from N = 966 to N = 179 suppresses the potential to find any robust relationships with other variables, even if they may be weaker. Conceptually speaking, the results of this model are fairly sparse, and leave little room to interpret variables unrelated to baroclinicity at the intensification phase.

Nonetheless, although the only overlap between the two data sets is seen with the jet stream and EGRs, the MPI-ESM-LR data reveals a slightly different picture. For storms whose developments are constrained by genesis in RW and intensification in RE, it is a combination of strong thermal gradients (such as land-sea contrasts) at genesis, high magnitudes of intensification variables (e.g. the jet stream), and to a lesser extent the possible role of

a strongly positive NAO directing the storm in the right direction during its intensification phase.

M5: All North Atlantic storms with regional covariates

The purpose of this model is to see if describing the regional development of storms through the addition of predictors is more helpful than subsetting storm data. Models M2, M3 and M4 showed that if we subset storms which either generated in RW or intensified in RE, our chosen predictors better described the variance in the storm footprint. However, by subsetting storms with strict conditions (model M4), the significant reduction in data lead to models with little to explore in ERA-20C. This is where subsetting of the storms into specific pathways begins to break down. We now instead additively include the predictors `greg` and `mireg`. This model utilizes Equation 33.

	MPI-ESM-LR			ERA-20C		
Predictor	*Estimate*	*Standard error*	*p-value*	*Estimate*	*Standard error*	*p-value*
Intercept	-2.49	0.236	$< 10^{-10}$	-2.75	0.716	$< 10^{-4}$
`greg`	0.197	0.0609	0.00124	0.226	0.113	0.0459
`lsc`	0.159	0.0281	$< 10^{-7}$	—	—	—
`sstg`	—	—	—	0.136	0.0521	0.00928
`jet`	0.279	0.0353	$< 10^{-10}$	0.365	0.0521	$< 10^{-10}$
`eady`	0.0780	0.0346	0.0243	—	—	—
`pv`	0.137	0.0285	$< 10^{-5}$	—	—	—
`naop`	0.339	0.0982	$< 10^{-4}$	—	—	—

Table 16: M5 summary. $R^2 = 0.12$ and 0.10 for MPI-ESM-LR and ERA-20C, respectively.

In the MPI-ESM-LR results, the predictors `mireg` and `sstg` are not selected by stepwise AIC, but the remaining predictors are all significant to p < 0.05 (Table 16). Now, `greg` appears as a strong and significant predictor. This predictor is accompanied by a reduction in the relative strength of `jet` and `lsc` compared to the other predictors (compared to model M1).

For the ERA-20C results, this model is in fact most similar to M1. The predictors `sstg` and `jet` are the strongest here, and `pv` has now vanished as a relevant predictor. Instead, `greg` emerges here as a strong and significant predictor.

Thus, we see that `greg` has some utility in these models in the sense that it emerges as a "good" predictor (i.e. it is significant has a high parameter estimate). Moreover, the predictor `mireg` does not become relevant. Conceptually, this model highlights the importance of cyclogenesis in the RW as a crucial component of a European storm's footprint, but that explicit information about an intensification phase in RE is not as useful (given that most storms intensify in RE, this is to be expected). As we mentioned in the description for model M1's results, we may be missing important dynamical variables which are important in explaining the development of storms forming in e.g. Arctic or sub-tropical regions.

M6: All North Atlantic storms with regional covariates and interactions

The final model is nearly identical to M5 in its motivation and construction, except that predictors include interaction terms using the formula of Equation 34. The benefit of including interaction terms is that we can identify the contribution of combined effects. For example, we would expect that storms that explicitly generate in RW in the presence of strong LSCs would significantly increase the potential footprint of a storm substantially.

	MPI-ESM-LR			ERA-20C		
Predictor	*Estimate*	*Standard error*	*p-value*	*Estimate*	*Standard error*	*p-value*
Intercept	-2.48	0.236	$< 10^{-10}$	-3.90	0.938	$< 10^{-4}$
greg	0.197	0.0609	0.00124	2.49	1.60	0.120
lsc	0.159	0.0281	$< 10^{-7}$	-0.0653	0.0777	0.401
sstg	—	—	—	0.226	0.0757	0.00293
jet	0.279	0.0353	$< 10^{-10}$	0.343	0.0548	$< 10^{-9}$
pv	0.137	0.0285	$< 10^{-5}$	0.0702	0.0559	0.209
naop	0.339	0.0982	$< 10^{-4}$	—	—	—
greg:lsc	—	—	—	0.182	0.147	0.203
greg:sstg	—	—	—	-0.236	0.143	0.109

Table 17: M6 summary. $R^2 = 0.12$ and 0.10 for MPI-ESM-LR and ERA-20C, respectively.

Following stepwise AIC, the MPI-ESM-LR results in the same model as M5 (Table 17). The ERA-20C results, however, differ considerably, and the model offers us a new perspective. The two interaction terms, `greg:lsc` and `greg:sstg`, have been selected. They both contain relatively high estimates (in opposing directions), with albeit non-significant values. Lastly, the estimate of `greg` has increased significantly compared to M5. For example, if we assume a storm that has formed in RW (`greg` = 1), we can quantify the effect that a unit change in `lsc` for all other variables held constant would have on $\log \mathbb{E}[\text{ssi}]$. We know that the β estimates for the relevant predictors are $\beta_{\text{greg}} = 2.49$, $\beta_{\text{lsc}} = -0.0653$ and $\beta_{\text{greg:lsc}} = 0.182$. This gives a total change of

$$\Delta \log(\mathbb{E}[\text{ssi}]) = 2.49 \times 1 - 0.0653 \times 1 + 0.182 \times 1 = 2.61 \tag{40}$$

compared to a storm which does not generate in RW. This total increase is higher than the sum of the individual changes due to either `lsc` or `greg` (which would be $2.49 - 0.0653 = 2.42$). Alternatively, considering `sstg` instead, this change would equate to an increase of around 2.49, and thus interactions with SST gradients are less relevant here.

Altogether, interaction terms were potentially useful in describing the storm footprint for ERA-20C, but not for MPI-ESM-LR. Nonetheless, the terms were not significant in ERA-20C and a larger data set might be required to capture a robust relationship between the footprint and the coupling of these terms.

4.7   Summary of models

We investigated six models as applied to two sets of data. The role of each model was to approach the task of describing the storm footprint with multiple angles, whether by looking at all systems (M1) or regionally-constrained ones (M2 — M6). As each model is either a) applied to different subsets of data and b) utilizes different predictors, it is not a useful exercise to rank the models as "best" to "worst". Rather, we can use the diagnostics to see if models are better suited for describing a specific set of storms, such as M4. The drawback of this model was that aggressively subsetting data reduced our ability to find robust relationships in ERA-20C, especially with regards to thermal gradients. Despite the reduced R^2, M5 was a useful model as well. It showed that by loosening the constraints of subsetting data by including the regional development as predictors, we could find a robust relationship between the storm footprint and SST gradients in ERA-20C. Other models had more drawbacks. By including all storms with no regional constraints, M1 could only describe a portion of the storm footprint variance with no information about genesis or intensification regions. In M3, storms were subset by eastern-intensification; however, given that this included the majority of storms in each respective data set, it was not significantly different to M1. Finally, model M6 included explicit interaction terms between various quantities, which did not prove to add much value in interpreting MPI-ESM-LR data.

In addition, there was the matter of the choice of GLM and its diagnostics. For the aforementioned results, a Gamma model with a log-link function proved sufficient, although a Gaussian model with an identity link could also have been used. The Gamma model diagnostics were carried out by studying the residual behaviour, which were shown to be homoskedastic and resistant to any outliers in the data. In addition, no predictors were found to be strongly co-linear with one another. The backwards stepwise AIC model selection criterion typically discarded predictors in the ERA-20C data, but not the MPI-ESM-LR data. This may be explained by the substantially larger data size of MPI-ESM-LR.

In terms of summarizing the predictors themselves, generally speaking, western genesis, the jet stream, PV, and EGRs play the largest role in explaining the variance of windstorm footprints, regardless of the type of storms that are studied. There is an important role of LSCs and SST gradients, but these disagree between the data sets, where ERA-20C sees more value in using SST gradients and vice versa for MPI-ESM-LR. In addition, a strongly positive NAO is typically a strong predictor, but mainly in MPI-ESM-LR, rarely showing up in the model results for ERA-20C data except in M2, i.e. western-generated storms. This could be related to the mean tilt of the storm track and the direction of storm travel in the respective datasets. The storm track is more zonally-oriented in MPI-ESM-LR, while the southwest-northeast tilt is reproduced in ERA-20C (Varino et al., 2019). This implies that zonally-oriented MPI-ESM-LR storms are less likely to propagate into and stay in Central/Northern Europe (recall that we exclude storms intensifying in the Mediterranean, which is situated in Southern Europe). Thus, a strongly positive NAO is more likely to deflect such storms northwards. Altogether, this effect is not as crucial for ERA-20C storms.

Thus, to build upon our previous concept(s) of what makes a storm destructive, these results confirm, to some extent, what we expected: storms that generate in the west and intensify with the aid of baroclinicity, jet stream, or diabatic effects are more likely to create a

stronger windstorm in Europe. More specifically, it is most dependent on a strong jet stream in the vicinity of Europe with PV and thermal gradient anomalies as secondary effects. One could argue, from these results alone, that the role of the NAO is not exact and that it appears to be strongly dependent on the data and the tilt of the North Atlantic storm track; however, in general it can act to positively influence the footprint. However, the most interesting component of this study is the role of thermal gradients. Two general features across all models could be identified here. The first is that thermal gradients emerged as relevant predictors in all MPI-ESM-LR models, but for only three ERA-20C models. The second is that the two data sets disagree on the role of land-sea contrasts or SST gradients. This is in contrast with the findings of Section 2, which not only found no evidence for SST gradient magnitudes affecting windstorm footprints, but also a stronger influence of land-sea contrasts in ERA-20C compared to MPI-ESM-LR. Despite the plethora of possibilities presented by the results of here and Section 2, this certainly calls for a deeper investigation into systematic differences in the role of thermal gradients on European cyclone and windstorm intensities.

4.8   Model conclusions

The chapter concerns the stated question: "Can we rank, in order of importance, which factors play the most important role in a windstorm's footprint?". A GLM has been constructed by exploring an appropriate statistical family for the response variable (the storm footprint), a suitable link function, and the integration of predictors. To begin with, a set of predictors comprised of continuous and categorical predictors used to represent states of atmospheric and conceptual variables has been selected and screened. It was found that a log-transformation of the footprint revealed clearer linear relationships between itself and the other predictors, in particular the jet, EGR, and PV850 predictors. It was found that various predictors had strong correlations amongst themselves, in particular between the jet and EGR predictors. However, no one predictor could explain the log-footprint alone. We further found that a binary NAO predictor was more useful in terms of R^2 and significance compared to the originally-used continuous predictor.

In Section 3, we saw large increases (between footprint extremes) in the jet stream, PV850, and EGRs at the intensification phase of storms in RE. This study shows that all storm footprints "in between" can be explained, to some extent, by these factors. Moreover, while we previously found weak LSC and SST gradient signals, these results show that they do have some direct influence on the storm footprint. We were additionally able to elaborate on the role of the NAO. A positive NAO phase is associated with higher footprint storms, either through a trajectory that is guided towards Europe or by simply stronger storms. The NAO results were mostly consistent for MPI-ESM-LR data, where we surmised that the zonal bias in the tilt of the storm track in MPI-ESM-LR was a possible reason. As with any study pertaining to environmental factors and cyclones, cyclones can feed back onto all of these variables, an effect which we cannot completely untangle. The differences between the data sets are mainly constrained to a) the role of the thermal gradients, b) the utility between using `naop` and `b` as a predictors, and c) the relative importance of EGR and PV anomalies. Moreover, MPI-ESM-LR results generally "prefer" PV anomalies whilst ERA-20C "prefer" EGR — the reasons for this are unclear.

We have learned of the different contributions from these variables using many GLMs. The GLMs have provided us a set of statistically significant standardized regression parameters, allowing us to "rank" the different factors in order of importance. We were able to do this for storms following specific pathways and in two data sets. However, the GLMs describe between 9 - 18% of the total variance between the data sets. This shows that predicting storm footprints with this model would not be totally practical, and that a suite of other predictors would be necessary.

As already demonstrated, representing spatio-temporal variables as univariate quantities is challenging, and other methods could be explored. For instance, we could use the jet latitude index to represent the jet, LSCs could be represented in a more primitive way (e.g. Walz et al., 2018), and we could even use EOFs as a way to represent specific patterns. The model-building process further demonstrated that representing the regional development of these storms was challenging and requires a more precise representation. Although adding regions as covariates added some value to the models, it was only a minor improvement, and coupling these regions to predictors produced differing results between data sets. Utilizing different data analyses (such as classification schemes) to identify high- or low-footprint storms based on different states or thresholds is another way to explore the importance of different factors, for example.

5   Synthesis

5.1   Conclusions

This thesis explored the factors affecting the footprint of European windstorms. We began by justifying the need to go beyond studying windstorm frequencies, and to additionally consider their footprints. For instance, we typically consider a stormy season to be one in which a high number of windstorms occurred; on the contrary, we found that seasons with numerous storms do not necessarily align with a high total storm footprint. In order to relate windstorm footprints to states of North Atlantic variables, we first look to the cyclones which formed them. It was postulated that the formation and evolution of windstorms is highly dependent on the cyclones which form them, thus we followed with a comprehensive statistical analysis of how the two systems relate to one another. Following this, we introduce the role of cyclonic growth factors (CGFs), where we discussed how a specific set of variables with idealized positions and/or occurrences would likely impact the footprint of the windstorm. Finally, we attempted to quantify the relative role of each of these factors on the footprint of the windstorm using a GLM. Altogether, the primary findings of these studies are consolidated in the schematic in Figure 38.

Following this figure, let us begin by exploring the key cyclone pathways discussed in Chapter 2. There are a number of regions where high footprint cyclones likely generate, as indicated by G1 — G4 (Figure 15). G1 represents the majority of these cyclones which generate over the US East Coast before, before propagating East-Northeast towards Europe. G2 — G4 represent smaller subsets of pathways related to Greenland-generated storms (G2), secondary cyclogenesis due to frontal waves from previous cyclones (G3; the two green dashed arrows represent the primary and secondary cyclones), and weaker, more stationary Mediterranean systems (G4) which were excluded from Chapters 3 and 4. What G1 — G3 have in common, however, is that they are maritime by nature, and experience maximum intensification (MI) of the cyclone near the British Isles (Figure 16). We additionally learned that cyclone's daughter windstorm (W) likely forms in a ±24 hour of the MI point, before the windstorm intensifies in Europe and maximizes its footprint. In Chapter 3, we focused on windstorms related to G1-type cyclones. We found that zonally-extended baroclinicity anomalies (EGRs or jets; blue) situated at both its genesis over the US East Coast and near the British Isles are related to higher footprint systems, as well as PV850 anomalies during MI (Figures 23, 24, and 25). Moreover, thermal gradient anomalies, notably LSCs in the US East Coast, are conducive with higher footprint systems. SST gradient anomalies do not directly affect the footprint of the system, but instead increase the probability that cyclogenesis in the US East Coast leads to a European windstorm. These same thermal gradients were speculated to help create G2-type systems. Finally, the GLM constructed in Chapter 4 quantified the relative role of these factors, and emphasized the importance of a strongly positive NAO (NAO++) in guiding G1- and G3-type systems towards Europe (see Table 13). Naturally there are a multitude of cyclone pathways and CGFs not covered in this thesis that remain to be explored. However, from these results we can rank the factors affecting the severity of European winter windstorms: the presence of a jet anomaly during MI (blue region near British Isles) and G1-type cyclones are the most important, followed
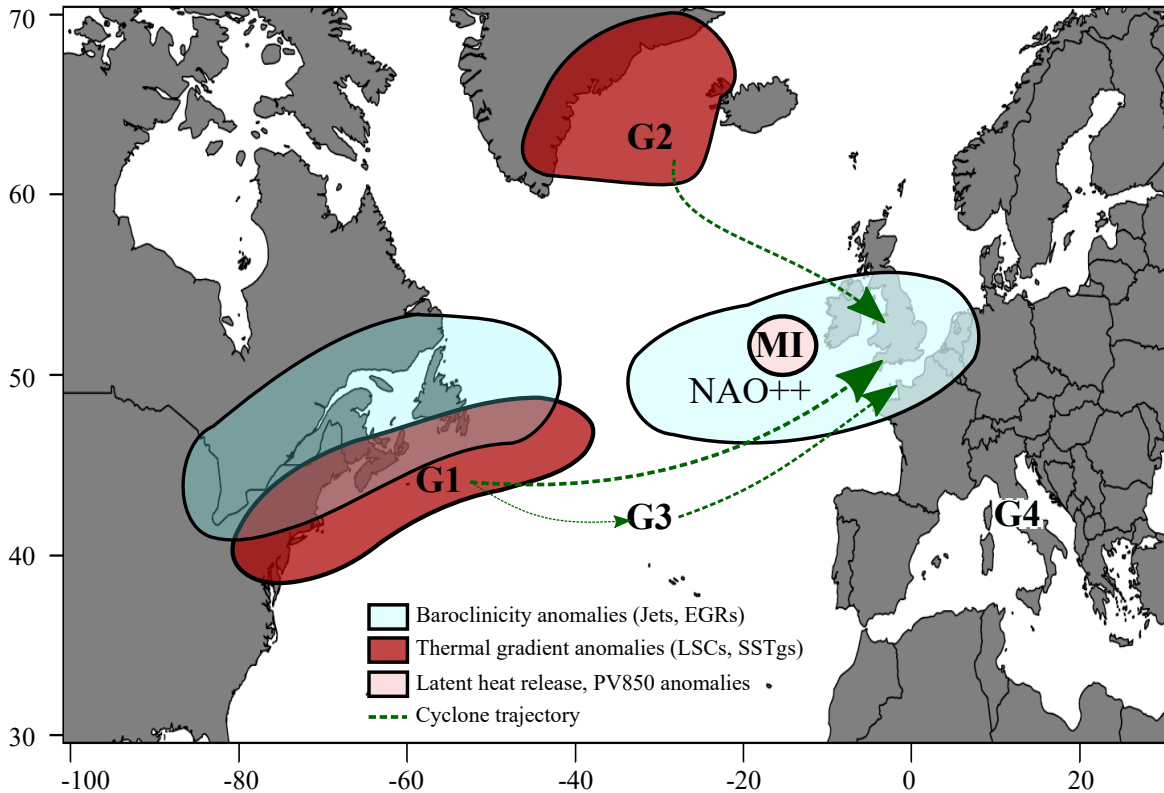
Figure 38: Schematic summarizing the idealized cyclone pathways which are likely to result in high European windstorm footprints, based on the results of the thesis. G1 through G4 represent the four possible points of cyclone genesis (see text for more detail), whose pathways are shown as dashed green lines. The various CGF anomalies are displayed as lightly shaded red, blue, and pink regions (for baroclinic effects, thermal gradients, and PV850 anomalies, respectively). Maximum intensification of the cyclone (MI, circled), occurs near the British Isles, ideally in a strongly positive NAO phase (NAO++). The daughter windstorms (W) form around the MI point as well, reaching maximum intensification shortly after and maximizing their footprint in Europe.

by EGR and PV850 anomalies at MI; thermal gradients — especially LSCs — are important for some systems, but see systematic differences depending on the dataset studied.

5.2 Developments and Outlook

This section describes the ways in which we can expand upon the work of this thesis. Beginning with Chapter 2, this part of the thesis work provides a framework for which future windstorm researchers can utilize the windstorm footprint metric and how it depends on cyclone properties. More specifically, it provides an intuitive picture of *when* and *where* the windstorm is expected to form with respect to the cyclone, so that the cyclone can be used to the windstorm researcher's advantage. To expand on the work, one could primarily focus on expanding the definition of the footprint metric in two ways. The first is to adapt it to only account for grid boxes that exist solely within the European region. As previously stated, the current footprint metric looks for the geographical *center* of clusters within Europe and aggregates all grid boxes around it, even if they are outside the defined region (conversely, if the center is outside the region but grid boxes overlap with the region, it is not considered). Second, the footprint could be adjusted to only include land-based grid boxes. This

could also be addressed using the distribution-independent SSI metric (Walz et al., 2015). This metric is well-designed for fairly comparing surface wind speed percentiles across ocean, land, and mountain grid boxes, which all contain different percentiles and slightly different distributions, and thus contribute differently to the SSI. Another limitation of the results from Chapter 2 relate to the storm pathways we considered. While we primarily identified two pathways with the use of density maps (Figures 15, 16, 17 and 18), groups of high or low footprint windstorms could instead be obtained with classification schemes, such as those related to machine learning. A number of windstorm properties remained to be investigated more thoroughly, namely their geometry, size, and possible relation to non-cyclonic systems. Moreover, expanding on the growth statistics, a more focused study detailing the lag or lead of cyclone growth with respect to their daughter windstorms would provide a more complete picture. Lastly, a deeper understanding of the potential impact of windstorms and their predictability can be achieved by classifying them into sub-types (for instance, one could identify elongated, localized windstorms associated with frontal activity). One could even identify windstorms at the mesoscale, such as those associated with squall lines.

In Chapter 3, this section of the thesis is the first to systematically relate windstorm strengths to environmental variables on an event-by-event basis. In particular, it used $|\nabla T_{2m}|$ as a diagnostic for land-sea contrasts, as well as the usage of PV850 as a proxy for diabatic development. These two quantities which are often overlooked in cyclone studies. Lastly, in combination with the Chapter 2, it has elucidated how the aforementioned variables affect the genesis and maximum growth of high-footprint cyclone systems. The most obvious expansion to this work is to consider more environmental variables. Notably, Rossby Waves could be considered as an upper-level forcing. Trains of Rossby Waves are known precursors of strong cyclones through downstream development, whereby upstream processes produce trains that develop further east and generate or intensify cyclones (e.g. Orlanski and Sheldon, 1995; Glatt et al., 2011; Wirth and Eichhorn, 2014). This could be accompanied with a diagnostic applicable to storm-centered compositing (e.g. Ghinassi et al., 2018). Moreover, the formation of extreme surface wind speeds is likely dependent on the existence of surface thermal fronts, so that diagnostics related to frontogenesis, frontolysis, and frontal characteristics could be used as a precursor for high footprint windstorms. An alternative route is to instead continue this study with the pressure tendency equation (PTE), as applied by Fink et al. (2012) and Pirret et al. (2017). Although the PTE works in a scalar framework, it attributes pressure changes in cyclones to specific upper- or lower-level forcings, and could no doubt be expanded to surface wind speed or footprint attribution. Other minor improvements can be made to the compositing method, for example rotating the frame in the direction of the storm. Another way to approach this study would be to study specific windstorm events identified by reanalyses, coupled with an ensemble (such as storms from the ECMWF Ensemble Prediction System). This would provide an even more robust framework to find systematic changes in storm footprints based on a range of environmental conditions. Lastly, on the topic of data resolution we recall that the role of land-sea contrast and SST gradients needs to be elucidated further as their relationships to storms may differ with higher resolution data.

Finally, the section of Chapter 4 demonstrates that the construction of the GLM is important to the study of windstorms for a number of reasons. For one, R^2 values of up to

0.18 were obtained. While small, they were statistically significant, and further development could improve R^2 values to the point where a GLM can be used to predict windstorm footprints. In a similar vein, this is the first study to assess windstorm properties using a GLM in an explanatory manner. It shows promise in employing field means of a number of environmental variables (such as LSCs, PV850, or baroclinicity anomalies), which may no doubt prove useful for future statistical analyses of windstorms. Following this line of thought, it could further benefit from the application of the PTE. Namely, the PTE seamlessly integrates many processes from multi-dimensional fields (such as air temperature on many levels) to univariate quantities. Such quantities could readily be applied to the GLMs. As far as statistical modeling goes, there are a number of other methods one could use to assess footprint-enhancing factors. For one, Bayesian networks can clearly visualize the specific chain of conditional events required for high or low European footprint storms to form; thus, while not quantitative, could make for a clearer conceptual interpretation of windstorm evolution. Finally, the same GLM experiments could be applied to a grid-point-wise map of SSIs (instead of individual windstorm events). This could be fruitful in explaining regional variations in surface wind impacts. More specifically, it could provide useful information for public and private stakeholders who may wish to develop statistical models to *predict* the intensity of future storm events in specific areas of interest.

Bibliography

Adamson, DS et al. (2006). "Boundary-layer friction in midlatitude cyclones". In: *Quarterly Journal of the Royal Meteorological Society: A journal of the atmospheric sciences, applied meteorology and physical oceanography* 132.614, pp. 101–124.

Ahmadi-Givi, Farhang, Graig, GC, and Plant, RS (2004). "The dynamics of a midlatitude cyclone with very strong latent-heat release". In: *Quarterly Journal of the Royal Meteorological Society* 130.596, pp. 295–323.

Akaike, Hirotugu (1974). "A new look at the statistical model identification". In: *Selected Papers of Hirotugu Akaike*. Springer, pp. 215–222.

Allen, John T, Pezza, Alexandre B, and Black, Mitchell T (2010). "Explosive cyclogenesis: A global climatology comparing multiple reanalyses". In: *Journal of Climate* 23.24, pp. 6468–6484.

Ambaum, Maarten HP and Novak, Lenka (2014). "A nonlinear oscillator describing storm track variability". In: *Quarterly Journal of the Royal Meteorological Society* 140.685, pp. 2680–2684.

Athanasiadis, Panos J, Wallace, John M, and Wettstein, Justin J (2010). "Patterns of wintertime jet stream variability and their relation to the storm tracks". In: *Journal of the Atmospheric Sciences* 67.5, pp. 1361–1381.

Befort, Daniel J et al. (2016). "Different long-term trends of extra-tropical cyclones and windstorms in ERA-20C and NOAA-20CR reanalyses". In: *Atmospheric Science Letters* 17.11, pp. 586–595.

Bengtsson, Lennart, Hodges, Kevin I, and Keenlyside, Noel (2009). "Will extratropical storms intensify in a warmer climate?" In: *Journal of Climate* 22.9, pp. 2276–2301.

Booth, James F et al. (2012). "Sensitivity of midlatitude storm intensification to perturbations in the sea surface temperature near the Gulf Stream". In: *Monthly Weather Review* 140.4, pp. 1241–1256.

Brayshaw, David James, Hoskins, Brian, and Blackburn, Michael (2009). "The basic ingredients of the North Atlantic storm track. Part I: Land–sea contrast and orography". In: *Journal of the Atmospheric Sciences* 66.9, pp. 2539–2558.

Büeler, Dominik and Pfahl, Stephan (2017). "Potential vorticity diagnostics to quantify effects of latent heating in extratropical cyclones. Part I: Methodology". In: *Journal of the Atmospheric Sciences* 74.11, pp. 3567–3590.

Burnham, Kenneth P and Anderson, David R (2002). "Model selection and Multimodel Inference: A Practical Information-Theoretic Approach". In:

Čampa, Jana and Wernli, Heini (2012). "A PV perspective on the vertical structure of mature midlatitude cyclones in the Northern Hemisphere". In: *Journal of the atmospheric sciences* 69.2, pp. 725–740.

Cardinali, Carla (2013). "Observation influence diagnostic of a data assimilation system". In: *Data Assimilation for Atmospheric, Oceanic and Hydrologic Applications (Vol. II)*. Springer, pp. 89–110.

Chandler, Richard E (2005). "On the use of generalized linear models for interpreting climate variability". In: *Environmetrics: The official journal of the International Environmetrics Society* 16.7, pp. 699–715.

Dacre, Helen F and Gray, Suzanne L (2013). "Quantifying the climatological relationship between extratropical cyclone intensity and atmospheric precursors". In: *Geophysical Research Letters* 40.10, pp. 2322–2327.

Dacre, Helen Francis and Gray, Suzanne Louise (2009). "The spatial distribution and evolution characteristics of North Atlantic cyclones". In: *Monthly Weather Review* 137.1, pp. 99–115.

Davis, Christopher A (1992). "A potential-vorticity diagnosis of the importance of initial structure and condensational heating in observed extratropical cyclogenesis". In: *Monthly weather review* 120.11, pp. 2409–2428.

Davis, Christopher A and Emanuel, Kerry A (1991). "Potential vorticity diagnostics of cyclogenesis". In: *Monthly weather review* 119.8, pp. 1929–1953.

Davis, Christopher A, Grell, Evelyn Donall, and Shapiro, MA (1996). "The balanced dynamical nature of a rapidly intensifying oceanic cyclone". In: *Monthly weather review* 124.1, pp. 3–26.

Day, Jonathan J and Hodges, Kevin I (2018). "Growing land-sea temperature contrast and the intensification of Arctic cyclones". In: *Geophysical Research Letters* 45.8, pp. 3673–3681.

Deveson, ACL, Browning, KA, and Hewson, TD (2002). "A classification of FASTEX cyclones using a height-attributable quasi-geostrophic vertical-motion diagnostic". In: *Quarterly Journal of the Royal Meteorological Society: A journal of the atmospheric sciences, applied meteorology and physical oceanography* 128.579, pp. 93–117.

Dobson, Annette J and Barnett, Adrian G (2008). *An introduction to generalized linear models*. Chapman and Hall/CRC.

Donat, Markus G et al. (2010). "Examination of wind storms over Central Europe with respect to circulation weather types and NAO phases". In: *International Journal of Climatology* 30.9, pp. 1289–1300.

Donat, MG et al. (2011). "Reanalysis suggests long-term upward trends in European storminess since 1871". In: *Geophysical Research Letters* 38.14.

Field, Andy (2005). *Discovering statistics using SPSS*. Thousand Oaks, CA, US.

Fink, Andreas H et al. (2009). "The European storm Kyrill in January 2007: synoptic evolution, meteorological impacts and some considerations with respect to climate change". In: *Natural Hazards and Earth System Sciences* 9.2, pp. 405–423.

Fink, Andreas H et al. (2012). "Diagnosing the influence of diabatic processes on the explosive deepening of extratropical cyclones". In: *Geophysical Research Letters* 39.7.

Gastineau, Guillaume, D'Andrea, Fabio, and Frankignoul, Claude (2013). "Atmospheric response to the North Atlantic Ocean variability on seasonal to decadal time scales". In: *Climate dynamics* 40.9-10, pp. 2311–2330.

Gastineau, Guillaume and Frankignoul, Claude (2015). "Influence of the North Atlantic SST variability on the atmospheric circulation during the twentieth century". In: *Journal of Climate* 28.4, pp. 1396–1416.

Ghinassi, Paolo, Fragkoulidis, Georgios, and Wirth, Volkmar (2018). "Local finite-amplitude wave activity as a diagnostic for Rossby wave packets". In: *Monthly Weather Review* 146.12, pp. 4099–4114.

Giorgetta, Marco A et al. (2013). "Climate and carbon cycle changes from 1850 to 2100 in MPI-ESM simulations for the Coupled Model Intercomparison Project phase 5". In: *Journal of Advances in Modeling Earth Systems* 5.3, pp. 572–597.

Glatt, Ilona et al. (2011). "Utility of Hovmöller diagrams to diagnose Rossby wave trains". In: *Tellus A: Dynamic Meteorology and Oceanography* 63.5, pp. 991–1006.

Graf, Michael A, Wernli, Heini, and Sprenger, Michael (2017). "Objective classification of extratropical cyclogenesis". In: *Quarterly Journal of the Royal Meteorological Society* 143.703, pp. 1047–1061.

Gray, Suzanne Louise and Dacre, Helen Francis (2006). "Classifying dynamical forcing mechanisms using a climatology of extratropical cyclones". In: *Quarterly Journal of the Royal Meteorological Society: A journal of the atmospheric sciences, applied meteorology and physical oceanography* 132.617, pp. 1119–1137.

Hartmann, Dennis L (2015). *Global physical climatology*. Vol. 103. Newnes.

Hoskins, Brian J and Valdes, Paul J (1990). "On the existence of storm-tracks". In: *Journal of the atmospheric sciences* 47.15, pp. 1854–1864.

Hurrell, J. W. et al. (2003). "The North Atlantic Oscillation: Climatic Significance and Environmental Impact". In: *Washington DC American Geophysical Union Geophysical Monograph Series* 134. DOI: 10.1029/GM134.

Jungclaus, JH et al. (2013). "Characteristics of the ocean simulations in the Max Planck Institute Ocean Model (MPIOM) the ocean component of the MPI-Earth system model". In: *Journal of Advances in Modeling Earth Systems* 5.2, pp. 422–446.

Keyser, Daniel and Shapiro, M. A. (1986). "A Review of the Structure and Dynamics of Upper-Level Frontal Zones". In: *Monthly Weather Review* 114.2, pp. 452–499. DOI: 10.1175/1520-0493(1986)114<0452:AROTSA>2.0.CO;2.

Klawa, M and Ulbrich, U (2003). "A model for the estimation of storm losses and the identification of severe winter storms in Germany". In: *Natural Hazards and Earth System Science* 3.6, pp. 725–732.

Knight, Jeff R et al. (2005). "A signature of persistent natural thermohaline circulation cycles in observed climate". In: *Geophysical Research Letters* 32.20.

Kruschke, Tim (2015). "Winter wind storms: identifcation, verification of decadal predictions, and regionalization". PhD thesis.

Kruschke, Tim et al. (2016). "Probabilistic evaluation of decadal prediction skill regarding Northern Hemisphere winter storms". In: *Meteorologische Zeitschrift* 25.6, pp. 721–738.

Leckebusch, Gregor C et al. (2008). "Extreme wind storms over Europe in present and future climate: a cluster analysis approach". In: *Meteorologische Zeitschrift* 17.1, pp. 67–82.

Liberato, Margarida LR (2014). "The 19 January 2013 windstorm over the North Atlantic: large-scale dynamics and impacts on Iberia". In: *Weather and Climate Extremes* 5, pp. 16–28.

Liberato, MLR et al. (2013). "Explosive development of winter storm Xynthia over the subtropical North Atlantic Ocean". In: *Natural Hazards and Earth System Sciences* 13.9, pp. 2239–2251.

Ludwig, Patrick et al. (2015). "Secondary Cyclogenesis along an Occluded Front Leading to Damaging Wind Gusts: Windstorm Kyrill, January 2007". In: *Monthly Weather Review* 143.4, pp. 1417–1437.

Madonna, Erica et al. (2017). "The link between eddy-driven jet variability and weather regimes in the North Atlantic-European sector". In: *Quarterly Journal of the Royal Meteorological Society* 143.708, pp. 2960–2972.

McCullagh, Peter and Nelder, John (2019). *Generalized linear models*. Routledge.

Minobe, Shoshiro et al. (2008). "Influence of the Gulf Stream on the troposphere". In: *Nature* 452.7184, p. 206.

Montgomery, Douglas C, Peck, Elizabeth A, and Vining, G Geoffrey (2012). *Introduction to linear regression analysis*. Vol. 821. John Wiley & Sons.

Murray, Ross J and Simmonds, Ian (1991). "A numerical scheme for tracking cyclone centres from digital data. Part I: Development and operation of the scheme". In: *Aust. Meteor. Mag* 39.3, pp. 155–166.

Nakamura, Hisashi et al. (2004). "Observed associations among storm tracks, jet streams and midlatitude oceanic fronts". In: *Earth's Climate: The Ocean–Atmosphere Interaction, Geophys. Monogr* 147, pp. 329–345.

Nakamura, Mototaka and Yamane, Shozo (2009). "Dominant anomaly patterns in the near-surface baroclinicity and accompanying anomalies in the atmosphere and oceans. Part I: North Atlantic basin". In: *Journal of Climate* 22.4, pp. 880–904.

Niehaus, Margaret CW (1980). "Instability of non-zonal baroclinic flows". In: *Journal of the Atmospheric Sciences* 37.7, pp. 1447–1463.

Nissen, KM et al. (2010). "Cyclones causing wind storms in the Mediterranean: characteristics, trends and links to large-scale patterns". In: *Natural Hazards and Earth System Sciences* 10.7, pp. 1379–1391.

Nissen, KM et al. (2014). "Decadal windstorm activity in the North Atlantic-European sector and its relationship to the meridional overturning circulation in an ensemble of simulations with a coupled climate model". In: *Climate dynamics* 43.5-6, pp. 1545–1555.

Novak, Lenka, Ambaum, Maarten HP, and Harvey, Ben J (2018). "Baroclinic Adjustment and Dissipative Control of Storm Tracks". In: *Journal of the Atmospheric Sciences* 75.9, pp. 2955–2970.

Orlanski, Isidoro and Sheldon, John P (1995). "Stages in the energetics of baroclinic systems". In: *Tellus A* 47.5, pp. 605–628.

Palutikof, JP and Skellern, AR (1991). "Storm Severity over Britain". In: *A Report to Commercial Union General Insurance, Climatic Research Unit, School of Environmental Sciences, University of East Anglia, Norwich (UK)*.

Parfitt, Rhys, Czaja, Arnaud, and Kwon, Young-Oh (2017). "The impact of SST resolution change in the ERA-Interim reanalysis on wintertime Gulf Stream frontal air-sea interaction". In: *Geophysical Research Letters* 44.7, pp. 3246–3254.

Pinto, Joaquim G et al. (2005). "Sensitivities of a cyclone detection and tracking algorithm: individual tracks and climatology". In: *Meteorologische Zeitschrift* 14.6, pp. 823–838.

Pinto, Joaquim G et al. (2009). "Factors contributing to the development of extreme North Atlantic cyclones and their relationship with the NAO". In: *Climate dynamics* 32.5, pp. 711–737.

Pirret, Jennifer SR, Knippertz, Peter, and Trzeciak, Tomasz M (2017). "Drivers for the deepening of severe European windstorms and their impacts on forecast quality". In: *Quarterly Journal of the Royal Meteorological Society* 143.702, pp. 309–320.

Poli, Paul et al. (2016). "ERA-20C: An atmospheric reanalysis of the twentieth century". In: *Journal of Climate* 29.11, pp. 4083–4097.

Pomroy, Hannah R and Thorpe, Alan J (2000). "The evolution and dynamical role of reduced upper-tropospheric potential vorticity in intensive observing period one of FASTEX". In: *Monthly Weather Review* 128.6, pp. 1817–1834.

Priestley, Matthew DK et al. (2017). "Rossby wave breaking, the upper level jet, and serial clustering of extratropical cyclones in western Europe". In: *Geophysical Research Letters* 44.1, pp. 514–521.

Raible, CC (2007). "On the relation between extremes of midlatitude cyclones and the atmospheric circulation using ERA40". In: *Geophysical research letters* 34.7.

Raible, Christoph C et al. (2018). "Extratropical cyclone statistics during the last millennium and the 21st century". In: *Climate of the Past* 14.10, pp. 1499–1514.

Reale, Marco et al. (2019). "A Global Climatology of Explosive Cyclones using a Multi-Tracking Approach". In: *Tellus A: Dynamic Meteorology and Oceanography* 71.1, pp. 1–19.

Renggli, Dominik (2011). "Seasonal predictability of wintertime windstorm climate over the North Atlantic and Europe". PhD thesis.

Rivals, Hélène, Cammas, Jean-Pierre, and Renfrew, Ian A. (1998). "Secondary cyclogenesis: The initiation phase of a frontal wave observed over the eastern Atlantic". In: *Quarterly Journal of the Royal Meteorological Society* 124.545, pp. 243–267.

Rossa, AM, Wernli, H, and Davies, HC (2000). "Growth and decay of an extra-tropical cyclone's PV-tower". In: *Meteorology and Atmospheric Physics* 73.3-4, pp. 139–156.

Roths, Scott (2018). *STAT 504 — Analysis of Discrete Data*. URL: https://newonlinecourses.science.psu.edu/stat504/ (visited on 01/02/2018).

Rudeva, Irina and Gulev, Sergey K (2007). "Climatology of cyclone size characteristics and their changes during the cyclone life cycle". In: *Monthly Weather Review* 135.7, pp. 2568–2587.

Sampe, Takeaki et al. (2010). "Significance of a midlatitude SST frontal zone in the formation of a storm track and an eddy-driven westerly jet". In: *Journal of Climate* 23.7, pp. 1793–1814.

Sanders, Frederick and Gyakum, John R (1980). "Synoptic-dynamic climatology of the "bomb"". In: *Monthly Weather Review* 108.10, pp. 1589–1606.

Scher, Sebastian et al. (2017). "Resolution dependence of extreme precipitation and deep convection over the G ulf S tream". In: *Journal of Advances in Modeling Earth Systems* 9.2, pp. 1186–1194.

Serreze, Mark C et al. (1997). "Icelandic low cyclone activity: Climatological features, linkages with the NAO, and relationships with recent changes in the Northern Hemisphere circulation". In: *Journal of Climate* 10.3, pp. 453–464.

Shaman, Jeffrey, Samelson, RM, and Skyllingstad, Eric (2010). "Air–sea fluxes over the Gulf Stream region: Atmospheric controls and trends". In: *Journal of Climate* 23.10, pp. 2651–2670.

Shaw, TA et al. (2016). "Storm track processes and the opposing influences of climate change". In: *Nature Geoscience* 9.9, p. 656.

Shmueli, Galit et al. (2010). "To explain or to predict?" In: *Statistical science* 25.3, pp. 289–310.

Stevenson, S, Rajagopalan, B, and Fox-Kemper, B (2013). "Generalized linear modeling of the El Nino/Southern Oscillation with application to seasonal forecasting and climate change projections". In: *Journal of Geophysical Research: Oceans* 117.8, pp. 3764–3781.

Titchner, Holly A and Rayner, Nick A (2014). "The Met Office Hadley Centre sea ice and sea surface temperature data set, version 2: 1. Sea ice concentrations". In: *Journal of Geophysical Research: Atmospheres* 119.6, pp. 2864–2889.

Trigo, Isabel Franco (2006). "Climatology and interannual variability of storm-tracks in the Euro-Atlantic sector: a comparison between ERA-40 and NCEP/NCAR reanalyses". In: *Climate Dynamics* 26.2-3, pp. 127–143.

Ulbrich, U, Leckebusch, GC, and Pinto, Joaquim G (2009). "Extra-tropical cyclones in the present and future climate: a review". In: *Theoretical and Applied Climatology* 96.1-2, pp. 117–131.

Ulbrich, U et al. (2001). "Three extreme storms over Europe in December 1999". In: *Weather* 56.3, pp. 70–80.

Varino, Filipa et al. (2019). "Northern Hemisphere extratropical winter cyclones variability over the 20th century derived from ERA-20C reanalysis". In: *Climate dynamics* 52.1-2, pp. 1027–1048.

Vries, Hylke de et al. (2019). "How Gulf-Stream SST-fronts influence Atlantic winter storms". In: *Climate Dynamics* 52.9-10, pp. 5899–5909.

Walz, Michael A, Donat, Markus G, and Leckebusch, Gregor C (2018). "Large-Scale Drivers and Seasonal Predictability of Extreme Wind Speeds Over the North Atlantic and Europe". In: *Journal of Geophysical Research: Atmospheres* 123.20, pp. 11–518.

Walz, Michael et al. (2015). "Development of a Distribution-Independent Storm Severity Index (DISSI)". In: *EGU General Assembly Conference Abstracts*. Vol. 17.

Wang, Xiaolan L, Swail, Val R, and Zwiers, Francis W (2006). "Climatology and changes of extratropical cyclone activity: Comparison of ERA-40 with NCEP–NCAR reanalysis for 1958–2001". In: *Journal of Climate* 19.13, pp. 3145–3166.

Wernli, Heini et al. (2002). "Dynamical aspects of the life cycle of the winter storm 'Lothar'(24–26 December 1999)". In: *Quarterly Journal of the Royal Meteorological Society: A journal of the atmospheric sciences, applied meteorology and physical oceanography* 128.580, pp. 405–429.

Willison, Jeff, Robinson, Walter A, and Lackmann, Gary M (2015). "North Atlantic storm-track sensitivity to warming increases with model resolution". In: *Journal of Climate* 28.11, pp. 4513–4524.

Wirth, V and Eichhorn, J (2014). "Long-lived Rossby wave trains as precursors to strong winter cyclones over Europe". In: *Quarterly Journal of the Royal Meteorological Society* 140.680, pp. 729–737.

Wood, Simon N (2017). *Generalized additive models: an introduction with R*. Chapman and Hall/CRC.

Woollings, Tim, Hannachi, Abdel, and Hoskins, Brian (2010). "Variability of the North Atlantic eddy-driven jet stream". In: *Quarterly Journal of the Royal Meteorological Society* 136.649, pp. 856–868.

Yamamoto, Ayako and Palter, Jaime B (2016). "The absence of an Atlantic imprint on the multidecadal variability of wintertime European temperature". In: *Nature communications* 7, p. 10930.